3.2 First-Principles Calculation of Material Properties

Development of database of anharmonic phonon properties using first-principles calculation

Masato OHNISHI

Department of Mechanical Engineering,

The University of Tokyo, Hongo, Bunkyo-ku, Tokyo 113-8656

Materials Informatics (MI) technology has rapidly developed in recent years. In materials science, limited data availability often hampers the development of materials using MI, making data expansion a critical challenge. Previous studies have led to the development of databases such as the Materials Project, AFLOW, and AtomWork, which focus on inorganic materials. However, these databases primarily feature data on electronic properties, such as band gaps and electronic band structures, and lack data on anharmonic phonon properties like thermal conductivity, crucial for developing thermo-functional materials. Therefore, since 2022, we have been developing a database dedicated to anharmonic phonon properties, utilizing first-principles calculations. In the fiscal year of 2023, our focus has primarily been on calculations that consider three-phonon scattering, excluding other factors such as four-phonon scattering, phonon renormalization, and electron-phonon interactions.

In this project, we developed computational software that automates the analysis of anharmonic phonon properties in inorganic materials using first-principles calculations. We employed VASP [1] for first-principles calculations and ALAMODE [2] for phonon calculations. Additionally, we utilized various Python libraries to enhance our processes: ASE [3] and Pymatgen [4] for handling crystal structures, Spglib [5] for crystal symmetry, and Custodian [4] for managing VASP job submissions and fine-tuning parameters. Currently, our software targets approximately 20,000 materials listed in the Phonondb (A. Togo) database of harmonic phonon properties, as well as non-metallic and non-magnetic materials from the Materials Project. Our process primarily considers three-phonon scattering, focusing mainly on stable structures. Automatic calculations for these materials are currently underway.

The calculations conducted in fiscal years 2022 and 2023 led to the determination of thermal conductivity (anharmonic phonon properties) for approximately 4,500 materials and harmonic phonon properties for over 10,000 materials, as illustrated in Fig. 3. This database now represents an unprecedentedly large collection of anharmonic phonon properties for inorganic materials based on first-principles

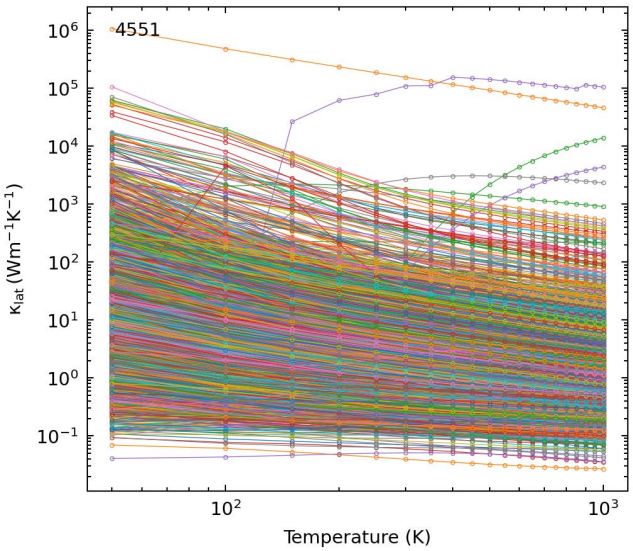

Fig. 3 Temperature-dependent thermal conductivity for approximately 4,500 analyzed materials.

calculations. Previously, publications related to MI typically discussed datasets encompassing no more than 100 materials. For the next step, our plans include expanding our calculations to metallic materials and approximately 48,000 stable materials that were recently announced by DeepMind at the end of 2023 [6].

As mentioned above, we have calculated the thermal conductivities for a large number of materials. However, as shown in Figure 3, some results indicate thermal conductivities exceeding 10,000 Wm-1K-1 at room temperature, and some exhibit a rapid increase in thermal conductivity with rising temperature. These unrealistic results can be attributed to the omission of four-phonon scattering and an insufficient density of the k-mesh in reciprocal lattice space, which lowers the accuracy of calculations, especially for materials with high thermal conductivity. Conversely, the data on materials with low thermal conductivity appears more reliable and is expected to be valuable for future predictions of thermal conductivity using machine learning.

References

[1] G. Kresse and J. Furthmüller, Phys. Rev. B 54, 11169 (1996).

[2] T. Tadano, Y. Gohda, and S. Tsuneyuki, J. Phys.: Condens. Matter 26, 225402 (2014).

[3] H. Larsen et al., J. Phys.: Condens. Matter 29, 273002 (2017).

[4] S. P. Ong, W. D. Richards, A. Jain, G. Hautier, M. Kocher, S. Cholia, D. Gunter, V. L. Chevrier, K. A. Persson, and G. Ceder, Comput. Mater. Sci. 68, 314 (2013).

[5] A. Togo and I. Tanaka, ArXiv. 1808.01590 (2018).

[6] N. J. Szymanski et al., Nature 624, 86 (2023).

Theoretical Study on Dynamical Processes in Heterogeneous Catalysis using Density Functional Theory and Machine Learning Methods

Thanh Ngoc PHAM, Harry Handoko HALIM, John Isaac G. ENRIQUEZ, Yuelin WANG, Muhammad Rifqi AL FAUZAN and Yoshitada MORIKAWA
Department of Precision Engineering, Graduate School of Engineering, Osaka University
2-1 Yamadaoka, Suita, Osaka 565-0871

Although first-principles electronic structure calculation methods have high prediction accuracy and have been used to elucidate various reaction processes, the spatial scale is limited to about nm and the time scale is limited to about several tens of ps because of the high computational cost. Recently, it has become possible to overcome this limit by combining DFT with machine learning methods. Using multi-scale simulations, we have been able to achieve large spacial scale and long time scale simulations on surfaces and interfaces that were previously impossible. We aim to elucidate the heterogeneous catalytic reaction process through multi-scale simulations and to identify factors that govern catalyst reactivity and provide guidelines for designing more efficient catalysts.

In this fiscal year, we investigated several systems which are important in both fundamental science and applications. Self-regenerative materials are keys to the development of stable catalysts used under high temperature condition, e.g., three-way catalyst converters in automobiles. Among others, metal nanoparticles supported on perovskite oxides are promising ones. However, little is known about their atomistic details, which are crucial for understanding and development of thermally stable catalysts. Therefore, we investigated a machine-learning enhanced density functional theory study of Pd_xO_y nanoparticles supported on a $Sr_3Ti_2O_7$ (001) surface and demonstrate that supported oxidized Pd particles fulfill the conditions for the self-regenerative catalysts [1].

We investigated the influence of CO to the formation of Cu clusters on Cu(111) surface by doing a set of MD simulations driven by machine-learning force-field [2]. By using the Cu island deposited on the Cu surface as the model, the simulations show that the CO-decorated Cu clusters are formed within a hundred of ns at 450 K and 550 K given the exposure to CO molecules. On the other hand, no cluster is formed on clean Cu surface even at 550 K. CO-decorated Cu clusters ranging from dimer to hexamer are detected within a hundred of ns at 450 K. Lowering the temperature to 350 K doesn't result in the formation of clusters due to the scarce detachments of adatom. Raising the temperature to 550 K results in the formation of bigger clusters, ranging from dimer to heptamer, but with shorter lifetime. The clusters can be formed directly through simultaneous detachment of a group of stepatoms or indirectly by agglomeration of wandering $Cu1(CO)_1$ and smaller clusters on the surface terrace. The statistical analysis on the evolution of the clusters shows the $Cu(CO)_1$ significantly involved in the formation and decomposition of the clusters due to their high mobility.

We also elucidated the surface facet depen-

dence on the oxygen adsorption and oxidized surface morphology of the diamond (111) and (100) surfaces to give insights that will improve the polishing, etching, and fabrication of diamond devices [3]. We used spin-polarized density functional theory to systematically simulate the O adsorption and CO and CO2 desorption reactions from pristine and etched diamond (111) and (100) surfaces. The results show that the surface facet dependence is caused by two factors: (1) the difference in the reactivity of the O_2 and (2) the difference in the carbonyl orientation of the O-terminated surfaces. The O_2 adsorption and activation energies on the C(111)-(2 × 1) surface are weaker and higher, respectively, compared to those on the C(100)-(2 × 1) surface. Moreover, the O_2 adsorption energy on the C(111)-(2 × 1) weakens with O_2 coverage. At monolayer O coverage, the carbonyl groups on the C(111)-(1 × 1):O surface have an inclined orientation which causes high steric repulsion between adjacent O atoms. The repulsion decreases with less neighboring molecules, leading to staggered etching, formation of islands, and loss of well-defined crystallographic orientation of the surface atoms. For the C(100)-(1 × 1):O surface, the carbonyl groups have an upright orientation and have low steric repulsion. The CO desorption activation energy is lower near an existing vacancy, leading to row-wise etching, which preserves the crystallographic orientation of the surface atoms.

We further performed DFT calculations and AIMD simulations to investigate the ORR mechanism on the sp-N1GDY/G and Pyri-NGDY/G with and without the solvation effect [4]. We found that under both vacuum and water conditions, ORR firstly proceeds on sp-N1GDY/G via dissociative mechanism because O_2 can be chemisorbed on a clean surface and easily dissociated rather than protonated to OOH*. However, OH* is strongly adsorbed on the sp-N1GDY/G surface, resulting in the weakening of the second O_2 adsorption, and ORR takes place via the ET-OHP associative mechanism. Pyri-NGDY/G also prefers ET-OHP associative mechanism.

We theoretically investigated the NO reduction reaction on Cu(100), Cu(111), Cu(110), Cu(211), and Cu(221) surfaces using a microkinetic analysis based on DFT energetics. [5]. We show that monomer dissociation requires high activation energies of more than 1 eV on almost all of the Cu surfaces we have considered. On the other hand, the existence of the flat-ONNO intermediate significantly lowered the activation energies, suggesting that the dimer-mediated pathway is preferred for NO dissociation, particularly at lower temperatures. Through this study, we provide an in-depth understanding of the NO reduction reaction on Cu surfaces over a wide temperature range.

References

[1] T.N. Pham, B.A.C. Tan, Y. Hamamoto, K. Inagaki, I. Hamada, and Y. Morikawa: ACS Catal. **14**, 1443 (2024).

[2] H.H. Halim, R. Ueda, and Y. Morikawa: J. Phys. Condens. Matter, **35**, 495001 (2023).

[3] J. I. G. Enriquez, T. Yamasaki, M. Michiuchi, K. Inagaki, M. Geshi, I. Hamada, and Y. Morikawa: J. Phys. Chem. C, **128**, 6294-6308 (2024).

[4] Y. Wang, T. N. Pham, H. H. Halim, L. Yan, Y. Morikawa: Materials Advances, **4**, 6542-6552 (2023).

[5] M. R. Al Fauzan, T. N. Pham, H. H. Halim, Y. Hamamoto, K. Inagaki, I. Hamada, and Y. Morikawa: J. Phys. Chem. C, **127**, 19451-19467 (2023).

Clarification of Microscopic Mechanisms of Semiconductor Epitaxial Growth and Device-Interface Formation by Large-Scale Quantum-Theory-Based Computations

Atsushi Oshiyama

Institute of Materials and Systems for Sustainability, Nagoya University

Furo-cho, Chikusa-ku, Nagoya 464-8601

In the fiscal year of 2023, on the basis of the total-energy electronic-structure calculations and molecular dynamics simulations within the density-functional theory (DFT), we have studied the epitaxial growth of wide-gap semiconductors, atomic and electronic structures of semiconductor-insulator interfaces, and mechanisms of atomic diffusion in semiconductors. The main computational tools are our RSDFT (Real Space DFT) code and RS-CPMD (Car-Parrinello Molecular Dynamics) code as well as VASP code. Specifically, we have studied 1) microscopic origin of hole traps at GaN/SiO_2 MOS device interfaces [1], 2) microscopic mechanism of the acceptor doping during epitaxial growth of GaN [2], and 3) possibility of recombination-enhanced migration of Mg acceptor in GaN [3]. The below is the explanation of the issue 1) above.

Identification of Hole Traps at GaN/SiO_2 MOS Device Interfaces

Power devices necessary to convert energies on the earth to electric power are crucial to sustain our energy-saving society in future. Currently, power devices based on silicon, are widely used, and overwhelming in the market. However, achieving higher efficiency and miniaturization of Si power devices is limited. In contrast, wide band gap semiconductors are obviously beneficial to energy conversion processes in power devices, and silicon carbide (SiC) and gallium nitride (GaN) indeed emerge in the market typically as MOSFET in power electronics.

In GaN-MOSFET devices, SiO_2 is usually used as a gate oxide. However unidentified hole traps emerge in such devices, and deteriorate the device performance. Recently, spontaneous formation of a Ga-oxide (GaO_x) intermediate layer with 1-2 nm thickness at the GaN/SiO_2 interface has been reported. We envisage that this nanometer-scale Ga oxide plays a role and have performed melt-quench calculations and explored the origin of the hole traps.

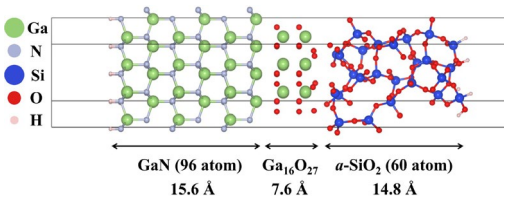

Fig. 1: Initial structure of GaN/GaO_x/SiO_2 interface in our slab model before the melt-quench calculations in the first-principles MD scheme. The thickness of the vacuum layer at the right and left sides is 12 Å

The GaO_x amorphous layer sandwiched by amorphous SiO_2 and GaN is simulated by atomic slabs separated from its images by vacuum regions as in Fig. 1.

Starting from the initial structure (Fig. 1), we perform melt-quench calculation and obtain stable GaN/a-GaO_x/a-SiO_2 structures. By adopting distinct heating and annealing procedures, we have prepared 4 distinct amorphous samples as shown in Fig. 2. Details of the heating and annealing procedures are found in our JAP paper [1].

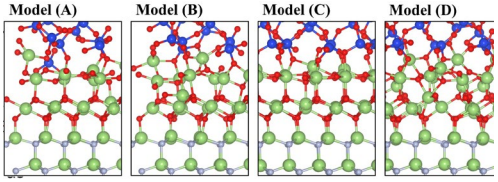

Fig. 2: Four distinct structures near the GaN/a-GaO_x/a-SiO_2 interfaces obtained by the first-principles MD calculations with the melt-quench technique. The color code is the same as in Fig. 1.

The local structures in the a-GaO_x layers obtained by our melt-quench calculations exhibit certain diversity. The Ga atoms are 4-, 5- or 6-fold coordinated with O atoms, whereas the O atoms are 2-, 3-, or 4-fold coordinated with either Ga or Si atoms. One of the important features in the local structures is the presence of the 2-fold coordinated O such as the -GaOSi- and the absence of the -GaOGa-. The presence of the 2-fold coordinated O is common in many oxides. However, what we have found for the nanometer-scale GaO_x sandwiched by GaN and SiO_2 is the sole presence of the -GaOSi- structure.

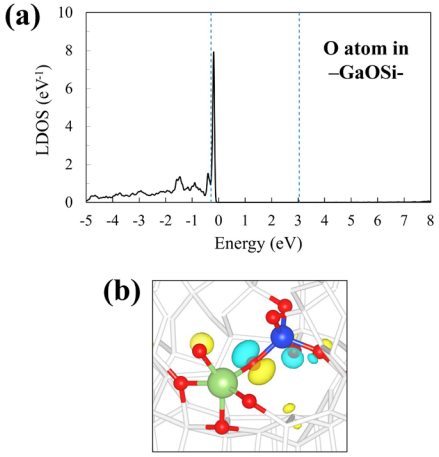

Fig. 3: Local density of states (LDOS) of the O atom in the -GaOSi- structure (a) and Kohn-Sham orbital at the LDOS peak (b). The blue dashed lines in the figure show the VBM and CBM of the GaN layer.

Figure 3 shows the local density of states contributed from this -GaO-Si local structure. We have found that this local structure induces a localized electron state just above the valence-band maximum, thus becoming a hole trap. The calculated Kohn-Sham orbital [Fig. 3(b)] unequivocally shows that this hole trap is the O lone pair state between Ga and Si atoms.

(The group id for this work is k0042)

Related publications

[1] S. Hattori, A. Oshiyama, and K. Shiraishi, J. Appl. Phys. to be published (2024).
[2] S. Yamauchi, I. Mizushima, T. Yoda, A. Oshiyama, and K. Shiraishi, Appl. Phys. Exp. to be published (2024).
[3] Y. Zhao, K. Shiraishi, T. Narita, and A. Oshiyama, App. Phys. Lett. to be published (2024).

Development of first-principles calculation code RSPACE and design of highly functional interface

Tomoya ONO
Graduate School of Engineering, Kobe University
Rokkodai-cho, Nada, Kobe 657-8501

SiC attracts much attention because it is one of the most promising wide-bandgap semiconductors for developing next-generation switching devices operating in high-power and high-frequency applications. However, the high channel resistance of SiC-MOSFETs hampers their performance. This high resistance is expected to be attributed to the low field-effect mobility in SiC-MOSFETs, which is much lower than the ideal electron mobility (~ 1000 $cm^2V^{-1}s^{-1}$). n-type MOSs, in which the inversion layers are composed by the conduction band edge (CBE) states, are more commonly used than p-type MOSs in the SiC-MOSFETs. The behavior of the CBE states of a SiC bulk is similar to that of free electrons and sensitive to the local atomic structure at the interface. In addition, in practical devices, off-oriented 4H-SiC(0001) surfaces by 4 degree are widely used. Thus, the SiC-MOS intrinsically possesses atomic-scale step and terrace structures even for the atomically flat surfaces. It is reported that the maximum field-effect mobility can be increased from 1-7 $cm^2V^{-1}s^{-1}$ to 25-40 $cm^2V^{-1}s^{-1}$ for 4H-SiC(0001) MOSFETs by interface nitridation by post-oxidation annealing with nitric oxide (NO). The microscopic information of the effect of NO annealing on a decrease of channel resistance of the SiC-MOSFET with atomic-scale steps is not fully clear although a lot of efforts have been made thus far.

In this study, the DFT calculation for the electronic structures of 4H-SiC(0001)/SiO_2 interfaces with atomic-scale steps is performed and the interface electronic structures before and after NO annealing are compared.[1]The computational models where the trench structure models are employed to imitate the step model are shown in Fig. 1 as an example. Owing to the excellent computation ability of supercomputer, such large models can be treated. In a 4H-SiC(0001) substrate, h and k site SiC bilayers are alternately stacked. The structure in which the Si atoms at the topmost h-site bilayer of the SiC substrate is bonded to the O atoms in the SiO_2 one-bond coordination is called the h1 model. The h3, k1, and k3 models were named similarly. The interface model with steps, in which the k1 and h3 interfaces are the upper and lower terraces, respectively, is named the k1/h3 model. The RSPACE code,[2] which uses the real-space finite-difference approach for the DFT, is employed.

Table 1: Partial charge density calculated in units of electron per supercell for flat interface before annealing. Data taken from Ref. 1.

Layer	k1	k3	h1	h3
1st-2nd	—	—	0.26	0.41
2nd-3rd	0.43	0.46	—	—
3rd-4th	—	—	0.44	0.43
4th-5th	0.43	0.44	—	—
5th-6th	—	—	—	—

The partial charge densities, which are projected on the wavefunction of the CBE states

Table 2: Partial charge density calculated in units of electron per supercell for step interface before annealing. Data taken from Ref. 1.

Layer	k1/h3	k3/h1	h1/k3	h3/k1
1st-2nd	—	—	0.14	0.02
2nd-3rd	0.39	0.23	—	—
3rd-4th	—	—	0.42	0.42
4th-5th	0.42	0.42	—	—
5th-6th	—	—	0.43	0.42

Table 3: Partial charge density calculated in units of electron per supercell for step interface after annealing. Data taken from Ref. 1.

Layer	k1/h3	k3/h1	h1/k3	h3/k1
1st-2nd	—	—	0.03	0.06
2nd-3rd	0.01	0.01	—	—
3rd-4th	—	—	0.14	0.12
4th-5th	0.39	0.40	—	—
5th-6th	—	—	0.43	0.43

of thin SiC bilayers, are defined as

$$\rho_{PC} = \Sigma_{i,k} \left| \int \Psi^*_{i,k}(\boldsymbol{r})\phi_k(\boldsymbol{r})d\boldsymbol{r} \right|^2 \times\theta(\epsilon_{i,k}-\epsilon_F)\theta(\epsilon_{max}-\epsilon_{i,k})\Delta_k, \quad (1)$$

where ϵ_F is the Fermi level, θ is the Heaviside function, and $\phi_k(x,y,z)$ is the wavefunction of the CBE states obtained by the thin film models. ϵ_{max}(=ϵ_F+1.65 eV), which is the maximum energy of the energy window, is chosen so that the energy window contains the CBE states inside the SiC substrate.

Table 1 lists the partial charge densities of the flat interface. We find that the partial charge density at the first bilayer in the h1 model is smaller than those at the other bilayers, which is consistent with the conclusion derived in the previous studies. The partial charge densities of the interfaces with steps before (after) NO annealing are also shown in Table 2 (Table 3). Our results indicate that the CBE states are absent below the upper terrace in some models before NO annealing owing to the finite-size effect and the Coulomb interaction of the O atom in the SiO_2 region. On the other hand, the effect of atomic configuration of the SiO_2 region is screened by the nitrided layer after NO annealing.

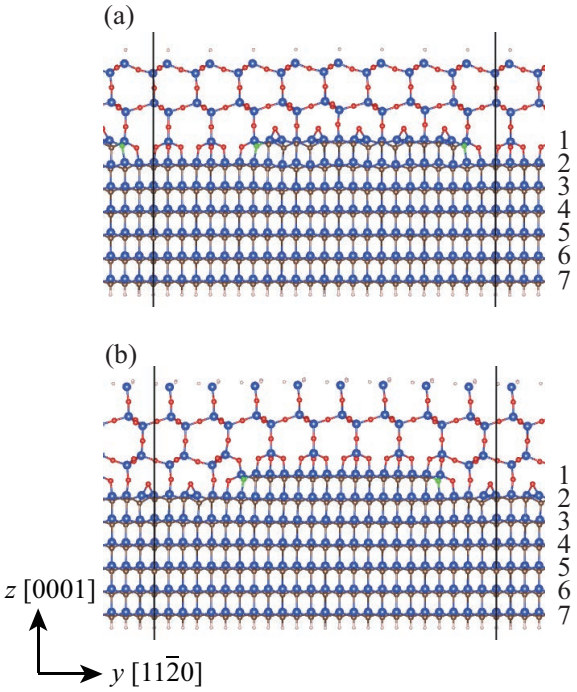

Figure 1: Interface atomic structure with steps for (a) k1/h3 (h1/k3) and (b) k3/h1 (h3/k1) models. Green, blue, red, and white balls represent N, Si, C, and O atoms, respectively. Black lines are the boundaries of supercells. The numbers written on the right-hand-side of the atomic structures are the indices of the atomic layers counted from the upper terrace.

References

[1] M. Uemoto, N. Funaki, K. Yokota, T. Hosoi, and T. Ono, Appl. Phys. Express **17**, 011009 (2024).

[2] K. Hirose, T. Ono, Y. Fujimoto, and S. Tsukamoto, *First-Principles Calculations in Real-Space Formalism, Electronic Configurations and Transport Properties of Nanostructures* (Imperial College, London, 2005).

First-principles study of functional materials

Fumiyuki ISHII, Naoya YAMAGUCHI, Rifky SYARIATI,
Hana Pratiwi KADARISMAN, Kaiki SHIBATA, Shohei MIURA,
Yaotang ZHANG, Yedija Yusua Sibuea TEWENG, Jin INOUE, Sota, YAMATE
Yume MORISHIMA, Khusnul YAKIN, Wardah AMALIA, Shigetomo YANASE,
Syifa Fauzia Hariyanti PUTURI, Ahmad GHIFFARI, Salsabila Amanda PUTRI
Nanomaterials Research Institute, Kanazawa University
Kanazawa, 920-1192, Japan

1. *Thermoelectric effect enhanced at van Hove singularity*[1]
The thermoelectric effect is a phenomenon where a temperature gradient generates an electric field, allowing for the effective harnessing of waste heat. There are two primary types of thermoelectric effects: the longitudinal Seebeck effect and the transverse Nernst effect. While the Seebeck effect generally results in higher thermoelectric conductivity, the Nernst effect is advantageous due to its simplicity and durability in thermoelectric devices.

In our research, we performed model calculations on a kagome lattice with a chiral spin state, focusing on the density of states (DOS) and its impact on thermoelectric conductivity. The DOS in this context shows singularities known as van Hove singularities (VHS). Our results indicate that these VHS enhance thermoelectric conductivity, leading to the prediction of a significant anomalous Nernst coefficient, approximately 10 μV/K at 50 K.

2. *Anomalous Nernst effect in Cr-doped Bi_2Se_3 singularity*[2]
We have investigated the electronic and thermoelectric properties of Cr-doped Bi_2Se_3 with six quintuple layers, modeling it as a quantized anomalous Hall insulator. Cr doping induces long-range ferromagnetism in Bi2Se3, a phenomenon confirmed both theoretically and experimentally. This magnetization leads to the experimental observation of the anomalous Hall effect in Bi_2Se_3, indicating that Cr-doped Bi2Se3 may exhibit Chern insulator characteristics. As a Chern insulator, it could serve as an outstanding transverse thermoelectric material, demonstrating a significant anomalous Nernst effect through the intrinsic contribution of the anomalous Hall effect and a pronounced Seebeck effect.

Using the rigid band approximation, we conducted first-principles density functional calculations to analyze the carrier-dependent anomalous Nernst coefficients. To enhance thermoelectric performance, we examined the origins of the anomalous Nernst effect, separating the contributions of the pure Nernst and Seebeck terms. Our study revealed a substantial contribution from the Seebeck term in Cr-doped Bi_2Se_3, attributed to the finite Chern number (C=-1). This finite Chern number is generated by the band splitting caused by out-of-plane magnetization from Cr doping. Consequently, we predict that Chern insulator materials, due to their Seebeck-induced effects, show great potential as transverse thermoelectric materials.

3. *Dirac electrons in graphene flake*[3]
Using the band unfolding method, we calculated the Dirac states of a finite graphene piece, referred to as a graphene flake. In a 15×15 rhombohedral graphene flake with an

approximate size of 3.7 nm, we clearly observed the Dirac states characteristic of pristine graphene, indicating the emergence of bulk-like electronic properties in this relatively small structure. To quantify these electronic properties, we determined the Fermi velocity by fitting the spectral weights using a weighted least-squares method. The approximated $E(k)$ and Fermi velocity for the 3×3 central region within the 15×15 graphene flake closely match those of pristine graphene. Our results highlight that the atomic arrangement and local periodicity in a small portion of the sample provide valuable insights into the system's electronic properties. The computational techniques used in this study may also be valuable for examining other finite or aperiodic systems, such as incommensurate twisted bilayer graphene.

4. *Proton Transfer in Triazole Molecules*[4] Triazole is an effective proton carrier because it features one proton donor and two proton acceptors. To investigate the proton transfer mechanism in triazole molecules, we performed density functional theory calculations in both gas and solvent phases. Our results indicate that 1,2,4-triazole molecules are more stable than 1,2,3-triazole molecules in both their neutral and protonated states. In the gas phase, proton transfer occurs only between symmetric molecular pairs. However, in solvent phases, proton transfer can also occur between some asymmetric molecular pairs as the proton donor-acceptor distance increases. The presence of solvents influences proton transfer by modifying the distance between proton donors and acceptors in triazole molecules.

References

[1] K. Shibata, N. Yamaguchi, H. Sawahata, and F. Ishii, J. Phys. Soc. Jpn. **92**, 124704(2023).

[2] R. Syariati, V. Saraswati, H. Sawahata, N. Yamaguchi, and F. Ishii, Jpn. J. Appl. Phys. **63** 01SP26 (2024).

[3] W. Amalia, N. Yamaguchi, S. Yunitasari, and F. Ishi, *submitted.*

[4] K. Yakin, N. Yamaguchi, T. Nakajima, M. Mizuno, F. Ishii, *submitted.*

Phonon effects in phase equilibria

Yoshihiro GOHDA
Department of Materials Science and Engineering, Tokyo Institute of Technology
J1-3, Nagatsuta-cho 4259, Midori-ku, Yokohama 226-8502, Japan

One of the most significant characteristic of metallic materials is the microstructure consisting of a few phases. Hence, many properties of metals cannot be understood from single crystals. The microstructure can be designed from the phase diagram that is determined from free energies of multiple phases. The free energy is decomposed into a few contributions, where the most important ones include the phonon effects and the configrational entropy. One of the problem in calculating the phonon free energy is the existence of the martensitic phase transition, where a high temperature phase is not stable at zero temperature exhibiting imaginary phonons. The self-consistent phonon (SCPh) method [1] can cure this problem.

In this project, we performed first-principles phonon calculations to evaluate free energies of metallic materials. Figure 1 shows calculated free-energy differences between the bcc and hcp phases for pure Ti and a Ti-Nb alloy. Since the bcc phase of Ti-based alloys exhibits martensitic phase transition, we performed SCPh calculations with the ALAMODE code [2]. In addition, we included effects of the electronic free energy, because we found it non-negligible. Even though binary Ti-Nb alloys has two-phase equilibrium regions in the phase diagram due to the digree of freedom in the composition variation, we fixed the composition so that the phase equilibrium occurs at a single temperature. The phase transition of the Ti-Nb alloy occurs at a lower temperature compared with pure Ti, consistent with an experimental fact that Nb is known as a bcc stabilizer in Ti-based alloys [3]. In addition, phase equilibria in permanent magnets were discussed through the CALPHAD approach with the first-principles cluster-expansion method [4].

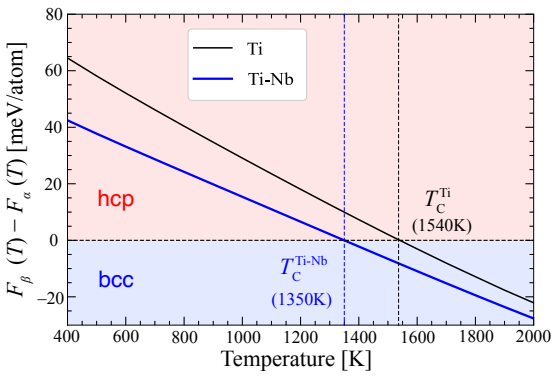

Figure 1: Calculated free-energy differences between the bcc and hcp phases for pure Ti and a Ti-Nb alloy as functions of the temperature T. $F_\alpha(T)$ indicates the free energy of the α phase, i.e., the hcp phase, whereas $F_\beta(T)$ is for the β phase, i.e., the bcc phase.

[1] T. Tadano and S. Tsuneyuki, Phys. Rev. B **92**, 054301 (2015).
[2] T. Tadano, Y. Gohda, and S. Tsuneyuki, J. Phys.: Condens. Matter **26**, 225402 (2014).
[3] K. Hashimoto, T. Tanaka, and Y. Gohda, in preparation.
[4] S. Enomoto, S. Kou, T. Abe, and Y. Gohda, J. Alloys Compd. **950**, 169849 (2023).

Analyses on local properties at complex structures via ab-initio-based methods

Satoshi WATANABE
Department of Materials Engineering, the University of Tokyo
7-3-1 Hongo, Bunkyo-ku, Tokyo, 113-8656

1 Introduction

The understanding of local properties in complex structures such as amorphous, surfaces, interfaces, and defects is becoming increasingly important as research and development of new information devices and energy-related systems progress. Nanoscale simulations with high prediction accuracy are a powerful means to gain this understanding, but those for local properties in complex structures are often still challenging due to the high computational cost. We have been addressing this issue not only using first-principles calculations but also employing machine learning potentials constructed based on data from first-principles calculations. In the following, two of our results from fiscal year 2023 are described.

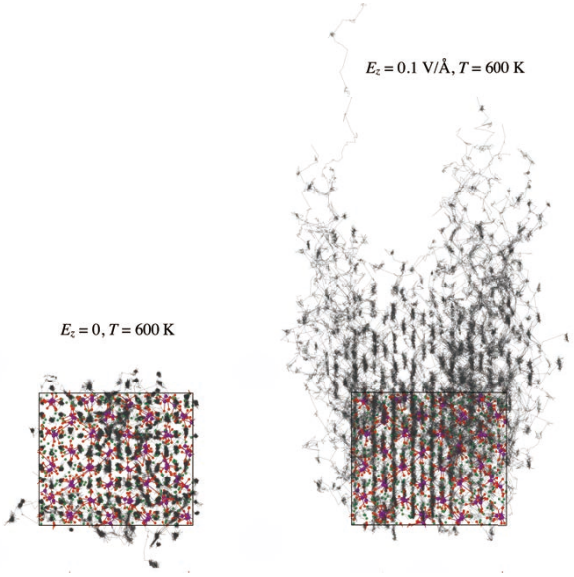

Figure 1: Calculated MD trajectories of Li in the amorphous Li_3PO_4 model for 300 ps at 600 K (left) without and (right) with the electric field. The z direction is upward one in the figure. Reprinted from Ref. [1].

2 Ion migration under electric fields

Understanding the ionic behavior under external electric fields is significant for the development of electronic and energy-related devices that utilize ion transport. To investigate such behavior, we developed a neural network (NN) model to predict the Born effective charges of ions [1]. By conducting molecular dynamics (MD) simulations that combine this NN model with a high-dimensional NN potential [2], we examined the migration of Li ions in Li_3PO_4 under a uniform electric field.

The prediction error of the constructed NN model, compared with the data from density functional perturbation theory, is 0.0376 e/atom. In MD simulations of a crystalline structure with a Li vacancy under a uniform electric field of 0.1 V/Å, we observed an enhanced mean square displacement of Li ions along the electric field, which appears to be physically reasonable. Furthermore, we obtained two interesting results. First, we found that the off-diagonal terms of the Born effective charges have a nonnegligible effect on Li migration under the electric field. Second,

in MD simulations of an amorphous structure without a Li vacancy, Li migration occurs in various areas despite the absence of explicitly introduced defects as can be seen in Fig. 1. We anticipate that the proposed NN method can be applied to any ionic material, facilitating the atomic-scale elucidation of ion behavior under electric fields.

3 Ion conduction in partially crystallized glass

Glass-ceramics, which crystallize from a glass state, often exhibit unique properties, including enhanced ionic conductivities compared to both the original crystalline and glass forms. However, details regarding the behavior of ion conduction in glass-ceramics, particularly the conduction pathways, remain elusive. We constructed a high-dimensional NN potential for Li_3PS_4 and examined the crystallization process of glass as well as ionic conduction through MD simulations.

First, we successfully reproduced experimentally observed crystallization from Li_3PS_4 glass. Next, we revealed that the diffusion barriers of Li decrease as the crystallinity in Li_3PS_4 glass-ceramics increases. Furthermore, we found that Li displacements predominantly occur in the precipitated crystalline portion, suggesting that percolation conduction plays a significant role in enhancing Li conduction. These findings provide valuable insights for the future utilization of glass-ceramic materials.

References

[1] K. Shimizu, R. Otsuka, M. Hara, E. Minamitani and S. Watanabe: Sci. Technol. Adv. Mater. Methods **3** (2023) 2253135.

[2] J. Behler and M. Parrinello: Phys. Rev. Lett. **98** (2007) 146401.

[3] K. Shimizu, P. Bahuguna, S. Mori, A. Hayashi, and S. Watanabe: J. Phys. Chem. C, submitted.

First Principles Design of GaN/Insulator Interface for GaN MOSFET

Kenji SHIRAISHI

Institute of Materials and Systems for Sustainability,

Nagoya University, Furo-cho, Chikusa-ku, Nagoya, Aichi 464-8601

Power devices necessary to convert energies on the earth to electric power are crucial to sustain our energy-saving society in future. The efficiency and also the compactness of such devices are essential to promote power electronics. GaN-based MOSFETs are promising power devices with high-speed operations owing to high mobility of carriers of GaN in addition to the high breakdown voltage. Many experiments have been conducted to investigate the GaN/SiO_2 interface properties. However, a high density of hole traps at the GaN/SiO_2 interface has been reported in experiments in the past [1]. This result obviously indicates that there are unidentified hole traps which make the carriers immobile at the GaN/SiO interface. Physical origins of those hole traps are totally unresolved.

We unveil atomic and electronic structures of the interface and identify the microscopic origin of the hole trap which has been a puzzle in GaN technology. The electron density of states (DOS) of the obtained GaN/a-GaOx/a-SiO_2 interface are shown in Fig. 1. A characteristic feature is the absence of electron states in midgap region of GaN. However, near to the valence-band maximum (VBM), within the energy region of about 1 eV. Those states appear in the energy gap at the edge of the valence bands [2].

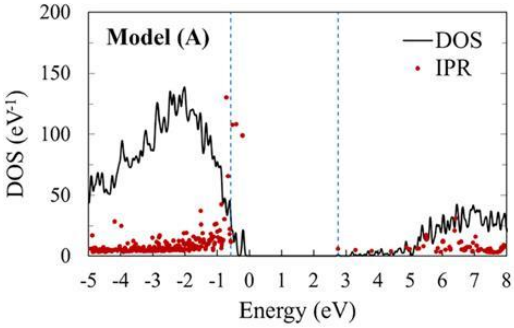

Fig.1: Calculated Density of State of GaN/a-GaOx/a-SiO_2 interface

These results indicate that O lone pairs in Ga-O-Si bonds are the atomistic origin of hole traps. Thus, to avoid these hole traps, the elimination of interfacial GaOx layers are inevitable.

References

1. Y. Wada, H. Mizobata, M. Nozaki, T. Kobayashi, T. Hosoi, T. Kachi, T. Shimura, and H. Watanabe, Appl. Phys. Lett. 120, 082103 (2022). (2020
2. S. Hattori, A. Oshiyama, and K. Shiraishi, J. Appl. Phys. 135, 175303 (2024).

Theoretical Studies on New Types of Point Defects Originated from Floating States in a-SiN towards Flash Memories Applications

Kenji SHIRAISHI

Institute of Materials and Systems for Sustainability,

Nagoya University, Furo-cho, Chikusa-ku, Nagoya, Aichi 464-8601

The a-SiN known as a useful hard material is now indispensable in current semiconductor technology: It is placed near the interface of Si-based metal-oxide-semiconductor structures and utilized as a nonvolatile flash memory which sustains our current data-driven society [1].

We performed first principles calculations to clarify the atomistic origin of charge traps in a-SiN which play crucial role in memory functions of recent flash memories.

In the actual a-SiN, H atoms are incorporated with its concentration of 10^{20}-10^{21}cm^{-3}. To clarify the role of the H atom, we have prepared H-incorporated a-SiN by our melt-quench scheme using $Si_{48}N_{63}H_3$ supercells. We have forged 4 distinct samples by varying heat treatments. By examining all the 4 samples, we have found, iour H-related local structures, NSi_2H, SiN_3H, NSi_3H and NSi_2H_2. We have found that these four H-related structures account for 92 % of all the H-related structures. This indicates that the under-coordinated or the wrong bond structures which induce mid-gap states are mostly passivated by H atoms. On the other hand, the SiN_4 configurations are not attached with H atoms. Hence the localized floating states (LFS) remain even in the H-incorporated amorphous samples (Fig. 1) [2]. As shown in Fig.1, LFS is hindered in the conduction band in case of neutral state, however it emerges as a charge trap state when electrons are captured. From these observation, LFS is the atomistic origin of a-SiN based flash memories.

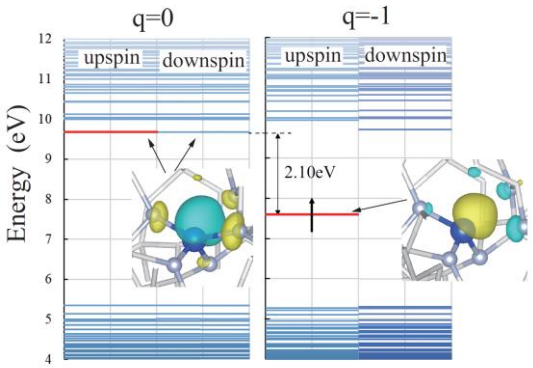

Fig.1: Energy levels and wave function of H incorporated a-SiN. (a) Neutral state. (b) Electron captured states.

References

1. K. Yamaguchi, A. Otake, K. Kobayashi, and K. Shiraishi, IEDM Tech. Dig. , pp. 275 (2009)..
2. Y. Nagaya, Master thesis, 2024, Nagoya University.

Identifying the Charge-Transition State in SiC/SiO_2 interfaces through a Combination of Ab-Initio Calculations and EDMR Experiments

Yu-ichiro MATSUSHITA

Laboratory for Materials and Structures,

Tokyo Institute of Technology, Yokohama 226-8503

In semiconductor physics, a quantitative understanding of interface properties is an extremely important research activity in device design. In particular, detailed analysis of defect levels is essential to understand interface defects and their effects on devices. In this article, we focus on the SiC-MOS (metal-oxide-semiconductor) interface, which is attracting attention as a next-generation power device, and present the results of our collaborative work with experiments to accurately understand the defect structure and its electronic levels.

In particular, it is known that the surface polarity of the SiC surface degrades the computational accuracy due to the ionic nature of the parent material. In this study, we first selected an electronic structure calculation method for SiC surface defects and confirmed the accuracy of the method. The electronic structure calculations for PbC centers were carried out using the high precision electronic structure approximation (HSE approximation) in combination with the finite size correction, as shown in Figure 1. The calculations show the existence of a (0/-) level 1.2 eV above the upper valence band (VBM). On the other hand, the latest experimental results from EDMR (electronically detected-magnetic-resonance spectroscopy) also confirm the location of the (0/-) level 1.2 eV above the VBM, and the combination of the HSE approximation and the finite-size correction allows us to calculate the electronic structure of interface defects with high quantitative accuracy. Considering the energy level, the P_{bC} center must impact both p- and n-channel devices, which is closely related to previously reported channel features. [1]

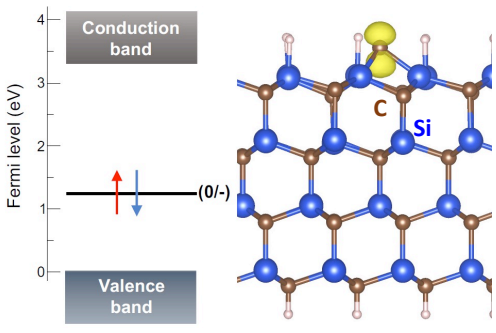

Figure 1. Results of elecgtronic structure calculations for Pbc centers. The calculated electronic levels (left) and their defect wavefunctions (isosurfaces at 15% of the maximum applitude of the wavefunction) (right).

In this study, we have used the RSDFT(Real-Space DFT) code on an ISSP Ohtaka Supercomputer.

References

[1] M. Sometani, APL Mater. **11**, 111119 (2023).

First-principles calculation of adsorption on electrode surfaces

Osamu SUGINO

Institute for Solid State Physics,

The University of Tokyo, Kashiwa-no-ha, Kashiwa, Chiba 277-8581

We have performed first-principles calculations of adsorbates on metal surfaces together with magnetic structure of a cuprate material. These calculations were based on the Generalized Gradient Approximation (GGA) or meta-GGA augmented with van der Waals functions scheme. This is because previous studies using GGA were often inconsistent with experiments and, on that basis, necessity of much more expensive functionals was argued. The simulated temperature programed desorption (TPD) spectra of an oxygen molecule and the distribution of the desorbed CO_2 were both consistent with experiment indicating accuracy of the functionals in describing the dynamics on Pt(111). These stringent benchmark calculations would prompt further simulation of the oxygen reduction reaction (ORR), CO oxidation, and other electrocatalytic reactions. The calculation scheme was also applied to water overlayers on Pt(111); although some inconsistencies in adsorption structure and energy remain, a serious comparison with experimental sum frequency generation (SFG) spectra has confirmed that the water molecules are arranged in such a way as to orient the hydrogen atoms towards the platinum surface. The computational scheme was moreover combined with the ring-polymer molecular dynamics simulation to study the quantum diffusion of H on Pd(111). By accelerating the simulation using the machine learning potential technique, the diffusing property of H atom was captured even at low temperatures where tunneling dominates. Simulation could explain how tunneling behavior differs between surface and bulk. We have further studied oxide materials, a pristine anatase TiO_2 surface, defective ZrO_2 surfaces and bulk $Sr_{1-x}La_xCuO_2$. The TPD spectra of O_2 were found to be consistent with the experiment for TiO_2; based on this result, we discussed the possible ORR efficiency on oxide-based electrocatalysts. The meta-GGA (SCAN) functional, which is able to describe the Mott transition of the cuprate, we discussed magnetic structure of this material.

Not only were these simulations time consuming, but the results needed to be provided in a timely manner to allow for collaboration with experiments. The ISSP supercomputer were found extremely useful for this purpose.

Analysis of thermal transport in disordered systems

Junichiro SHIOMI

Department of Mechanical Engineering,

The University of Tokyo, Hongo 7-3-1, Bunkyo-ku, Tokyo 113-8656, Japan

We have studied about thermal transport in complex systems. This year, we focused on the heat transport property of $FeCl_3$-graphite intercalation compounds and surface-disordered Si thin-film.

1. $FeCl_3$-graphite intercalation compounds

This research explores graphite and its intercalation with $FeCl_3$, aiming to uncover the mechanisms underlying the extremely low cross-plane thermal conductivity observed in GICs' experiments. In this study, we employed non-equilibrium molecular dynamics simulations to investigate the thermal conductivity of $FeCl_3$-graphite intercalation compounds (GIC) with various nanostructures, including different stages, thickness, and filling factor. Stage-'n' refers to the number of graphene layers sandwiched between neighboring intercalate layers, as shown in Fig. 1(a). Fixed boundary conditions were applied for cross-plane calculations (as shown in Fig 1(b)), and periodic boundary conditions were implemented for in-plane thermal conductivity analyses. By emulating superlattice, we observed decreasing-increasing trend in thermal conductivity, as shown in Fig. 2. We found that the cross-plane thermal conductivity increased with an increase in stage in a manner consistent with incoherent phonon interface scattering from $FeCl_3$ layers. However, at low stage (characterized by shorter periodic thickness), the decrease of cross-plane thermal conductivity as long-wavelength coherent phonon modes were expected to play a dominant role in the thermal transport, and the thermal conductivity values reached a saturated value of 0.3 W/m·K at stage5. The present work provides valuable insights into modulating the thermal properties of graphite by tuning phonon wave nature at room temperature with intercalated layered material. The observed decreasing-increasing thermal conductivity trend affirm the existence of coherent phonon transport at low stages.

2. surface-disordered Si thin-film

In this study, we investigated atomic-scale mechanisms underlying the reduction in thermal conductivity due to surface disorder by applying anharmonic lattice dynamics analysis to silicon thin-film structures with surface roughness. In this study, we fabricated ultra-thin silicon film structures with thicknesses ranging from 1 to 10 nm and introduced

disorder to the crystal structure of the surfaces to replicate surface roughness. The effect of surface roughness on suppressing thermal conductivity was usually estimated using the formula derived by Ziman[1]. However, the thermal conductivities of the thin films calculated in this study were lower than those estimated based on Ziman's formula (Fig. 3). Further analysis, separating the results into harmonic effects (phonon group velocity) and anharmonic effects (phonon relaxation time), revealed that while the harmonic effects suppressed thermal conductivity regardless of film thickness, the anharmonic effects were significant in suppressing thermal conductivity in extremely thin films of less than 5 nm. The insights from this study are useful for understanding the role of surfaces in materials with reduced thermal conductivity due to nanostructuring.

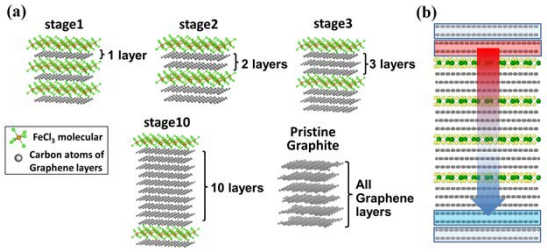

Fig. 1 Schematic illustration of the (a) main subject of this research, depicting various stages Graphite Intercalation Compounds (GICs) (b) setup for GIC's cross-plane thermal conductivity calculation, where the heat source and sink are positioned on the upper and lower sides.

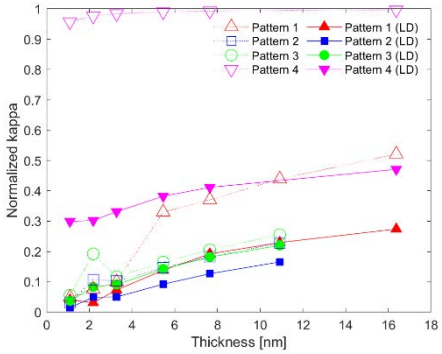

Fig. 3 Thermal conductivity of films with surface roughness. Normalized using the bulk thermal conductivity at T = 300 K. The empty markers represent the estimated thermal conductivity based on Ziman's formula[1], while the solid markers show the actual calculated results. Patterns 1-4 correspond to films with varying degrees of roughness.

References

[1] J. M. Ziman, Electrons and Phonons(Clarendon Press, Oxford,1960).

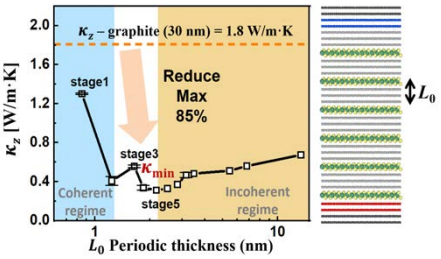

Fig. 2 Stage dependence of cross-plane thermal conductivity in GIC, with a constant total number of layers. Higher stages correspond to shorter periodic distances L_0 (the height of the smallest repeating unit) and more interfaces.

First-principles analysis of hydrogen-evolution semiconductor photocatalysts

Seiichiro L. TEN-NO
Graduate School of System Informatics, Kobe University
Rokkodai-Cho, Nada-Ku, Kobe 657-8501

Efficient dopants for high-performance photocatalytic $SrTiO_3$

Perovskite $SrTiO_3$ (STO) is a typical semiconductor photocatalyst for overall water splitting under ultraviolet. Similar to other photocatalysts, structural defects during synthesis should be controlled to promote photocatalytic activities. According to the recent experiment [1], it is observed that Al-doped STO can enable a quantum efficiency of almost unity at wavelengths between 350 and 360 nm.

To explore more efficient dopants for higher-performance photocatalysts, we have studied the dopant effects on the electronic structures of STO using the first-principles analysis based on the density functional theory (DFT). We use the supercell method to describe point defects including anion defects and substitutional doping, where several supercell models, namely, $2 \times 2 \times 3$, $2 \times 2 \times 4$, $3 \times 3 \times 3$, and $3 \times 3 \times 4$ supercell of the primitive cell of STO, are considered to take into account the finite size effects. The DFT calculations were performed within the PBE+U functional using PAW method as implemented in VASP [2]. The Hubbard U parameter was set to be $U =$ 4.36 eV for the 3d orbitals at the Ti sites, which reproduces the relative position of defect levels to the valence and conduction band.

Here we focus on the oxygen-site vacancy (V_O) and substitutional doping for the nearest Ti site. Since the O-defect works as the n-type doping and introduces 2 electron carriers, we also choose divalent and trivalent cations (namely, D^{2+} and T^{3+}) with a similar ionic radius to Ti^{4+} to introduce hole carriers. Then, we consider $D =$ Mg, Ni, Zn, and $D =$ B, Al, Ga, In, Tl, Sc.

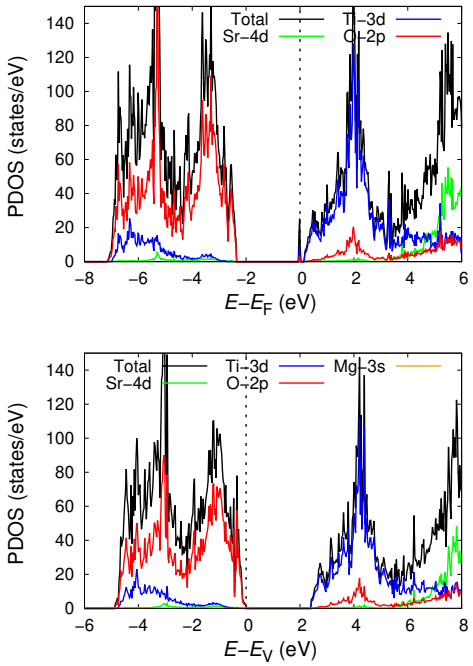

Figure 1: PDOS for (top) V_O and (bottom) Mg_{Ti}.

Figure 1 shows the projected density of states (PDOS) for V_O and Mg substitutional doping for the Ti, namely, Mg_{Ti}. Here the results of the $3 \times 3 \times 4$ supercell calculations are shown. In the presence of V_O, the defect level appears just below the conduction band minimum as a donor level. This defect level can

degrade the photocatalytic activities since it works as a recombination center. On the other hand, the Mg_{Ti} doping remove the defect level owing to the p-type doping, so that the photocatalytic degradation is expected to be prevented. We have also investigated whether the defect level can disappear in the other doping cases, namely, D_{Ti} and $2T_{Ti}$ doping.

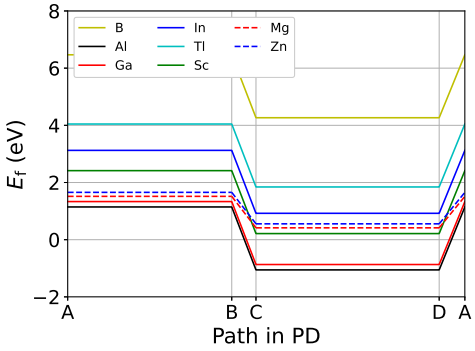

Figure 2: Dopant formation energy for each D_{Ti} and $2T_{Ti}$ doping.

Furthermore, we calculate the dopant formation energy for the D_{Ti} and $2T_{Ti}$ doping, which shown in Figure 3. Here each chemical potential is evaluated from the phase equilibrium of STO, and dopant chemical potentials are evaluated from the phase equilibrium of their oxides. Mg/Zn_{Ti} and $2Ga/Sc_{Ti}$ doping are easy to form according to the formation energy. Therefore, Mg/Zn_{Ti} and $2Ga/Sc_{Ti}$ doping can be expected to be efficient dopants for high-performance photocatalytic STO.

Hydrogen peroxide evolution on SnOx cocatalyst at hematite surface

Recent experiments have reported that when hematite (Fe_2O_3) is doped with Sn and Ti, the dopants diffuse to the particle surface to form a composite oxide ($SnTiO_x$) cocatalyst with hydrogen peroxide (H_2O_2) selectivity [3].

To investigate the water oxidation reaction on the SnO_x surface, we perform energy calculations of the adsorbates in each step of the

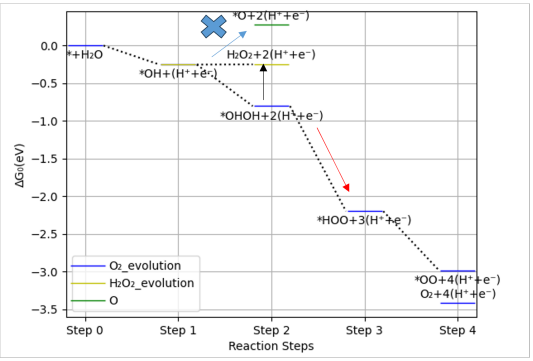

Figure 3: Energy diagram of water oxidation reaction added solvent effect.

predicted O_2 and H_2O_2 evolution reaction and perform a thermodynamic discussion. We find that both H_2O_2 and O_2 evolution reactions occur in structures without oxygen defects and with oxygen defects inside the bulk, while O_2 evolution reaction occurs in structures with oxygen defects near the surface. This result also suggests that there is a pathway for oxygen evolution other than the four-electron oxidation reaction. Furthermore, the numerical calculations including the solvent effect revealed that the 4-electron oxidation reaction and the O_2 evolution via 2-electron oxidation do not compete in real solvents.

Calculation conditions

We have performed hybrid (MPI+OpenMP) parallel computing using, where the parallelization over bands and k-points is used by VASP version 6.4.2.

References

[1] T. Takata *et. al.*: Nature **581**, 413 (2020).

[2] G. Kresse *et. al.*: Phys. Rev. B **47**, 558 (1993); Phys. Rev. B **49**, 14251 (1994); Computational Materials Science **6** (1996) 15–50; Phys. Rev. B **54**, 11169 (1996).

[3] Z. Zhang *et. al.*: Nat. Commun. **13**, 1499 (2022).

Improvement of accuracy and software development for the first-principles wave function theory

Masayuki OCHI
Forefront Research Center, Osaka University
1-1 Machikaneyama-cho, Toyonaka, Osaka 560-0043

April 1, 2024

We have developed a first-principles electronic structure calculation software using the transcorrelated (TC) method [1, 2]. The TC method is a many-body wave function theory, where Hamiltonian is similarity-transformed with the Jastrow correlation factor. By this transformation, electron correlation effects are efficiently considered. In particular, one-electron orbitals in the Jastrow-Slater-type wave function can be optimized in the same manner as the Hartree–Fock (HF) method, to say, by solving a one-body self-consistent-field (SCF) equation. It is advantageous that the computational cost for this process is the same order as that for the HF method [3].

In this year, we have published our study on isolated atoms [4]. In this study, we have tried several kinds of the Jastrow factor and checked the accuracy of fully-self-consistent TC+variational Monte Carlo (VMC) calculations. We found that the variance minimization in VMC is better compatible with TC than the energy minimization. In addition, an inclusion of the one-body Jastrow factor in VMC calculation gives better convergence of the self-consistency loop between TC and VMC calculations.

We have also studied condensed matter systems using our computational code TC++, which was published on github [5, 6] in the last year. One can perform TC calculations using TC++ by reading some output files dumped by DFT calculation using the Quantum-Espresso package [7]. TC++ supports the following functionalities: HF, TC, and biorthogonal TC (BITC) calculations, SCF and band calculations, solids and homogeneous electron gas, a plane-wave-basis set, and norm-conserving pseudopotentials. Calculation is MPI-parallelized for the k-point and band indices.

In this year, we have implemented the crystal-structure optimization using the Hellmann-Feynman force in the HF and BITC calculations. We note that the Hellmann-Feynman theorem holds for BITC but not for TC. We found that the lattice constants of bulk silicon is well reproduced by our (BI)TC calculations. We have also (internally) implemented the polynomial Jastrow factorsin (BI)TC calculations. The accuracy check is ongoing using supercomputers of ISSP.

References

[1] S. F. Boys and N. C. Handy, Proc. R. Soc. London Ser. A **309**, 209 (1969); *ibid.* **310**, 43 (1969); *ibid.* **310**, 63 (1969); *ibid.* **311**, 309 (1969).

[2] N. C. Handy, Mol. Phys. **21**, 817 (1971).

[3] M. Ochi, K. Sodeyama, R. Sakuma, and S. Tsuneyuki, J. Chem. Phys. **136**, 094108 (2012).

[4] M. Ochi, Phys. Rev. A **108**, 032806 (2023).

[5] https://github.com/masaochi/TC

[6] M. Ochi, Comput. Phys. Commun. **287**, 108687 (2023).

[7] https://www.quantum-espresso.org/

Density functional theory study of adsorption and reaction of molecules on metal surfaces

Ikutaro Hamada

Department of Precision Engineering, Graduate School of Engineering,

Osaka University, 2-1 Yamadaoka, Suita, Osaka 565-0871

To mitigate global warming and climate change, there is an urgent need to reduce fossil fuel usage and greenhouse gas emissions, particularly carbon dioxide. Considerable effort has been directed towards developing energy conversion devices like solar cells and proton exchange membrane fuel cells (PEMFC) based on renewable resources. Central to this effort is the development of molecules and materials for membranes and electrodes that facilitate efficient ion and electron transport and conversion.

Graphene has garnered significant attention due to its fascinating structural, mechanical, and electronic properties. Nitrogen-doped graphene, in particular, has demonstrated catalytic activity for the oxygen reduction reaction (ORR), crucial in PEMFC. Moreover, single transition metal atoms such as Fe and Co embedded in nitrogen-doped graphene have shown comparable catalytic activity to platinum, a highly active catalyst for ORR. However, to enhance the catalytic activity and durability of these single atom catalysts (SACs) within nitrogen-doped graphene, understanding the origin of their catalytic activity is imperative.

Computational studies, predominantly based on density functional theory (DFT), have been extensively conducted for this purpose. Yet, estimated catalytic activities, represented by limiting potentials—a measure of cell voltage in PEMFC—vary widely across the literature and do not consistently align with experimental results. Thus, further refinement of theoretical modeling for SACs is essential.

In this work [1], we performed DFT calculations of ORR on Fe and Co SACs embedded in nitrogen-doped graphene (Fe-N_4-C and Co-N_4-C), in which Fe and Co atoms are surrounded by 4 nitrogen atoms in graphene. We employed effective screening medium method combined with the reference interaction site mode (ESM-RISM) [2,3,4] that allows the systematic investigation of the roles of solvation, pH, and electrode potential, which are essential in the electrochemical reactions at the electrode-electrolyte interface. We used aqueous HCl as a solution with different electrolyte ion concentration (pH) using SPC and TIP5P models. All the calculations were performed using the projector augmented wave method [5] and revised Perdew-Burke Ernzerhof functional with dispersion correction (RPBE-D3) [6,7,8] as implemented in the Quantum-ESPRESSO package [9].

We investigated the oxygen reduction reaction (ORR) via the 4-electron associative mechanism. Initially, we calculated the limiting potentials with and without the electrolyte solution under neutral conditions using the computational hydrogen electrode method. The obtained limiting potentials were 0.66 V (Fe-N_4-C) and 0.51 V (Co-N_4-C) without the electrolyte solution, and 0.93 V (Fe-N_4-C) and 0.72 V (Co-N_4-C) with the electrolyte solution. These results did not align well with experimental observations. Particularly, we were unable to reproduce the trend where Fe-N_4-C and Co-N_4-C exhibited comparable limiting potentials.

However, by conducting calculations at a constant electrode potential, we obtained more accurate limiting potentials of 0.78 V (Fe-N_4-C) and 0.80 V (Co-N_4-C), which better matched experimental data. Through electronic structure analyses, we determined that the discrepancy between the results obtained under neutral conditions and those at constant electrode potential stems from differences in the charge states. Notably, in simulations at constant electrode potential, the active sites exhibit

significant charging.

This study highlights the critical role of surface charge/charge state in simulating electrochemical interfaces, indicating that accounting for that factor is essential for accurate predictions in such systems.

References

[1] A. F. Z. Abidin and I. Hamada, J. Phys. Chem. C **127**, 13623 (2023).
[2] M. Otani and O. Sugino, Phys. Rev. B **73**, 115407 (2006).
[3] N. Bonnet, T. Morishita, O. Sugino, and M. Otani, Phys. Rev. Lett. **109**, 266101 (2012).
[4] S. Nishihara and M. Otani, Phys. Rev. B **96**, 115429 (2017).
[5] P. E. Blöchl, Phys. Rev. B **50**, 17953 (1994).
[6] J. P. Perdew, K. Burke, and M. Ernzerhof, Phys. Rev. Lett. **77**, 3865 (1996).
[7] B. Hammer, L. B. Hansen, and J. K. Norskøv, Phys. Rev. B **59**, 7413 (1999).
[8] S. Grimme, J. Antony, S. Ehrlich, and H. Krieg, J. Chem. Phys. **132**, 154104 (2010).
[9] P. Giannozzi, *et al*. J. Phys.: Condens. Matter **29**, 465901 (2017).

Contributions of Second-Order Exchange Interactions in GW Electron-Hole Interaction Kernel

Yoshifumi NOGUCHI

Department of Applied Chemistry and Biochemical Engineering, Graduate School of Engineering, Shizuoka University, Johoku 3-5-1, Hamamatsu, Shizuoka 432-8561, Japan

The electron-hole interaction kernel, defined as the functional derivative of the one-electron self-energy operator using the one-particle Green's function, describes exciton binding energies and plays an important role in the determination of optical gaps. Within a GW approximation, four terms appear in the electron-hole interaction kernel including a first-order screened Coulomb interaction, a first-order bare Coulomb interactions, and two second-order interactions. The conventional GW+Bethe-Salpeter simulations have neglected the two second-order exchange terms based on the assumption that they are negligible small contributions, however the assumption has never been verified. In our previous study [1, 2], we implemented the full GW electron-hole interaction kernel, which includes not only the first-order direct and exchange terms but also the two second-order exchange terms, in our original all-electron mixed basis program and applied it to typical organic molecules [1]. In this study, we applied our method to the inter- and intra-molecular charge transfer excitations and discussed the contributions of the two second-order exchange terms. The significant

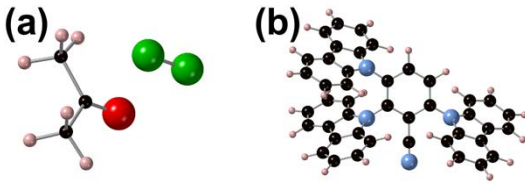

Fig. 1 Molecular geometries of (a) inter- and (b) intra-molecular charge transfer systems.

contributions were observed for thermally activated delayed fluorescence (TADF) molecules, in contrast to the typical organic molecules and the two-molecular systems. The two second-order exchange terms are several times larger than the first-order exchange term for the intra-molecular charge transfer excitations of TADF molecules. Our results suggest that the previous GW+Bethe-Salpeter simulations for TADF molecules should be reconsidered by considering the full GW electron-hole interaction kernel.

References

[1] Satoka Yamada, Yoshifumi Noguchi, Kohei Ishii, Daichi Hirose, Osamu Sugino, and Kaoru Ohno, Phys. Rev. B., **106**, 045113 (2022).

[2] Satoka Yamada and Yoshifumi Noguchi, J. Chem. Phys., **159**, 234105 (2023)

Equilibrium/nonequilibrium electrochemistry of disordered solid-state interfaces

Shusuke KASAMATSU

Academic Assembly (Faculty of Science),

Yamagata University, Kojirakawa, Yamagata-shi, Yamagata 990-8560

Simulation of solid-state electrochemical systems from first principles is challenging due to several factors including control of the chemical potential and handling of the combinatorial explosion in the possible number of ion configurations. To tackle these issues, we coded several new features into our original abICS framework for combination of high-throughput ab initio calculations (VASP, Quantum Espresso, or OpenMX), machine learning surrogate model training (aenet, nequip/allegro, MLIP3), and ensemble sampling [1].

To speed up the sampling for large-scale many-component systems, we implemented the population annealing Monte Carlo method for massively parallel ensemble sampling. We were also careful to cut back on file IO to minimize the impact on the network file system.

We also enabled calculation and control of the chemical potential through the implementation of free energy integration and grand canonical Monte Carlo sampling at fixed chemical potential. Figure 1 shows the state of charge in LiCoO2, an active material for Li-ion batteries, as a function of the Li chemical potential, which we calculated as a first test using the newly implemented grand canonical sampling. The results are in good general agreement with experiment. Further calculations on metal/solid electrolyte interfaces and electrocatalyst surfaces [2] are under way.

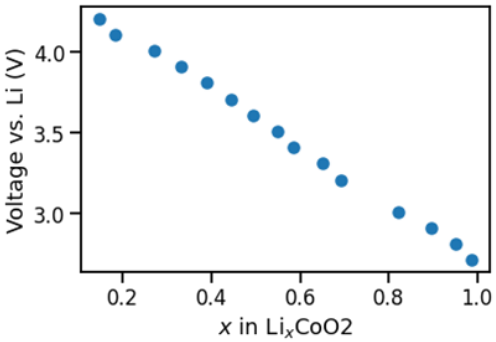

Fig. 1: Calculated state of charge vs. Li potential.

References

[1] S. Kasamatsu et al., Sci. Technol. Adv. Mater. Meth. 3, 2284128 (2023)

[2] A. Nakanishi et al., in preparation. arXiv:2307.11296

Large-scale simulations for magnetic nanopaticles

Hung Ba TRAN
Advanced Institute for Materials Research (WPI-AIMR), Tohoku University,
Email: *tran.ba.hung.a6@tohoku.ac.jp*,

Our previous works studied the effect of magnetic anisotropy on magnetocaloric properties by combining first-principles calculations and Monte Carlo simulations[1, 2, 3, 4]. The magnetic parameters, such as isotropic exchange coupling constants J_{ij}, the antisymmetric exchange also known as the Dzyaloshinskii–Moriya vector $\overrightarrow{D_{ij}}$, and magnetocrystalline anisotropy constants in uniaxial k_u and cubic k_c, are calculated from first–principles calculations. Then, the Monte-Carlo simulations are performed to estimate the magnetic properties at finite temperatures and external magnetic fields. We calculated the temperature dependence of magnetocrystalline anisotropy energy for uniaxial and cubic anisotropy. The Callen-Callen power law is widely used to determine the temperature dependence of magnetic anisotropy energy in the experiment, such as m^3 for uniaxial anisotropy and m^{10} for cubic anisotropy. Based on this power law, the magnetic anisotropy energy should be downed to zero at Curie temperature, where the magnetization disappears. However, we found that the magnetic anisotropy energy is not negligible even above Curie temperature in the case of uniaxial anisotropy. It comes from the magnetization anisotropy and anisotropic magnetic susceptibility. The evidence of finite magnetic anisotropy energy above Curie temperature from experimental works can be seen from the difference of isothermal magnetic anisotropy change when applying the magnetic field along the easy or hard axis in bulk CrI_3 and $AlFe_2B_2$[1, 2].

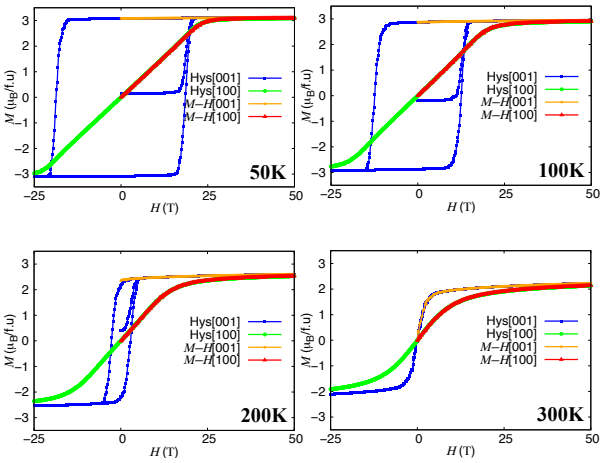

Figure 1: Temperature dependence of hysteresis loops and magnetization versus magnetic field M–H curves of $L1_0$ FePt nanoparticle.

In magnetic nanoparticles case, the magnetic anisotropy energy is the primary source of stabilizing magnetization against thermal fluctuation. The temperature dependence of the energy barrier in magnetic flips of the nanoparticles can be used to estimate the relaxation time of magnetic nanoparticles. In this study, we perform a large-scale simulation for $L1_0$ FePt nanoparticles by combining first-principles calculations and Monte Carlo simulations. Significantly, we found that the estimation of magnetocrystalline anisotropy energy of nanoparticles by using a hysteresis loop is not correct at finite temperatures due to the finite energy barrier of nanoparticles (Figure 1). In such cases, the magnetization versus magnetic field M–H curves are more reliable in estimating the temperature dependence of

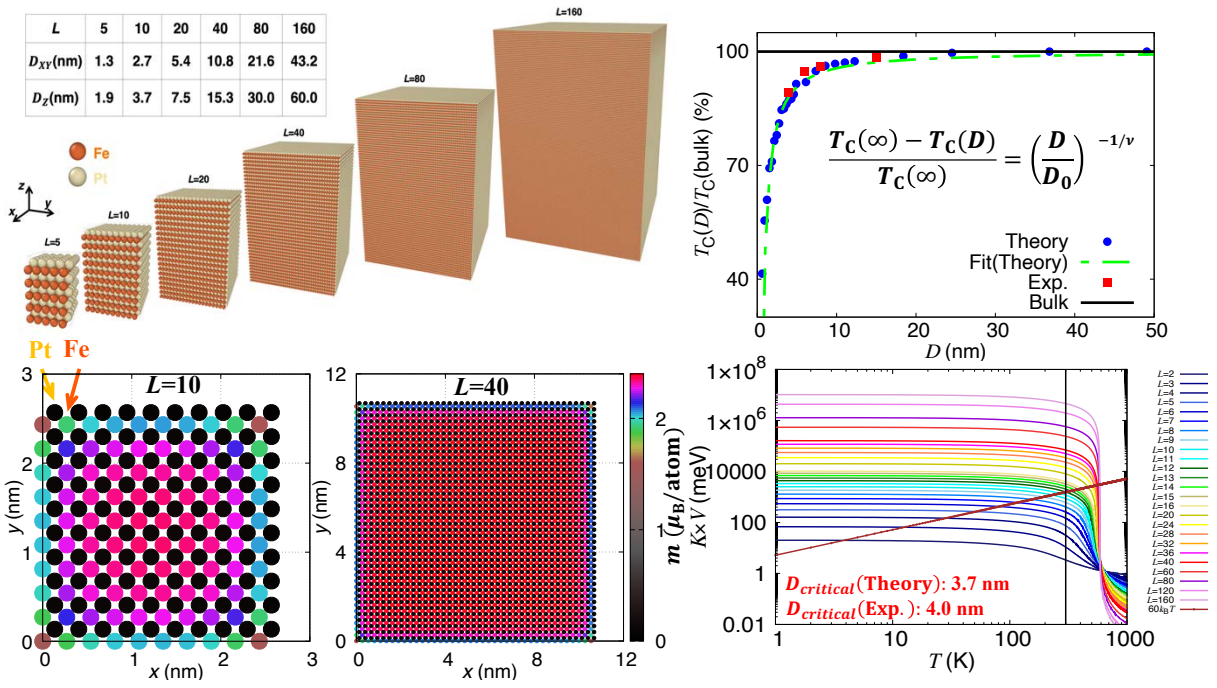

Figure 2: Size dependence of magnetic properties, such as Curie temperature, magnetic resolved, and energy barrier, of $L1_0$ FePt nanoparticle.

magnetic anisotropy energy.

The exponential behavior of the Curie temperature of various nanoparticle sizes is quantitatively reproduced compared with the data observed in the experimental works (Figure 2). The ferromagnetic order of nanoparticles will be absent at critical diameter D_0 due to the loss of the pairs in the exchange interaction at the surface. Moreover, the surface effect on the magnetic properties of $L1_0$ FePt nanoparticles is clarified by considering the magnetic profile in atomistic Monte Carlo simulations (Figure 2). Furthermore, the temperature and size dependence of the energy barrier for magnetic flips of $L1_0$ FePt nanoparticles is obtained in this work, demonstrating that the critical diameter of nanoparticles for long-term storage in hard-disk driver applications (10 years) is 3.7 nm, which is in good agreement with experimental work as 4.0 nm (Figure 2). Our work can be used as a guide to the experiment on developing the magnetic properties of nano-material applicable for magnetic recording.

References

[1] H. B. Tran, H. Momida, Y. Matsushita, K. Sato, Y. Makino, K. Shirai, and T. Oguchi, Phys. Rev. B **105**, 134402 (2022).

[2] H. B. Tran, H. Momida, Y. Matsushita, K. Shirai, and T. Oguchi, Acta Mater. **231**, 117851 (2022).

[3] H. B. Tran, Y. Matsushita, Appl. Mater. Today **32**, 101825 (2023).

[4] H. B. Tran, Y. Matsushita, Scr. Mater. **239**, 115799 (2024).

[5] H. B. Tran, Y. Matsushita, Scr. Mater. **242**, 115947 (2024).

Analyses on electronic/magnetic structuresinhigh-performance spintronics magnetic materials and parallelizationdevelopment/application in quasi-particleself-consistent *GW*code

Tatsuki ODA[1,2], Kazuki MURANAKA[2], Rinku MAJUMDER[2], Chandro PARDEDE[2], Jakub LUTSINEC[2], Ko HYODO[2], Masao OBATA[1,2]

[1]*Institute of Science and Engineering, Kanazawa University, Kanazawa, Ishikawa 920-1192*

[2]*Graduate School of Natural Science and Technology, Kanazawa University, Kanazawa, Ishikawa, 920-1192*

We have studied electronic structure in several systems of non-magnetic or magnetic material by means of density functional theory (DFT) approach or the quasi-particles self-consistent GW (QSGW) approach. Concerned with the latter calculation, we have successfully parallelized the corresponding part of computational code for the polarization function (PF), which is one of the most time-consuming parts in QSGW [1]. As a result, the computational time of PF was reduced by one order in the elapsed time using the ISSP computer for the system containing 16 atoms in the unit cell [2]. We have also developed the density functional theory (DFT) code optimized for GPU architecture [3].

(A) Migration of twin boundary

Migration of the twin boundary in a modulated martensite phase of the magnetic shape memory alloy Ni_2MnGa is significant to understand the magnetic shape memory effects. This work explored the migration mechanism of the nanotwin boundaries among the layers by first-principles calculations. We systematically analyzed intermediate structures throughout the migration path using the DFT approach [4]. We identified some key factors using the systems of 10M and 14M modulated phase. As a result, we obtained a concise barrier energy formula as empirical one. The resulting energy for barriers was found to be enough so low as a permission of the transition by the thermal energy.

(B) Ni_2MnX (X=Al, In) by QSGW

According to the QSGW, our group has found the Ni e_g orbitals appear just on the Fermi level in the cubic (austenite) phase of Ni_2MnGa, which leads to martensite phase transition by band Jahn-Teller effect. In addition, the generalized susceptibility provides the Fermi surface nesting vector, which coincides the experimental modulation for the

10M and 14M martensite phases [5]. These new achievements encourage several studies as revisit investigation. We investigated the electronic structures of Ni2MnX (X=Al, In) series using the QSGW [6].

(C) MAE in the alloy containing Pt element

Promising candidates for recording media, such as FePt alloys, have large magnetic anisotropy energy. This calculation aims to analyze the origin of magnetic anisotropy energy in a multilayer system of Pt/Fe/Pt. For this aim, in addition to a procedure of direct total energy calculation, the analysis for seeking the origins of anisotropy has been required. We are devoting the computational resources to set up a series of approach. It is one of the methods like the force theorem method. That will be completed in very near feature.

(D) Application to gallium oxide by QSGW

Wide band gap semiconductors are important materials for the power electronics applications. The beta-Ga_2O_3 has been fascinated recently because such material has a larger band gap and larger breakdown electric field compared with those of Si, SiC, and GaN, while it does not promote the removal of waste heat due to a shortcoming of its small thermal conductivity. To improve such heat removal, the interface with the sapphire substrate which promotes thermal conductivity has been studied in the experimental works. The final goal is of studies in such an interface, however, we calculated the band structures in the bulk and small slab systems using the QSGW at the present. We also used a hybrid exchange-correlation energy of QSGW and DFT for investigation. Using the hybrid method, the band gap energy was estimated to be the value obtained in the experiment within 1% accuracy [7]. We tried to investigate slab system of beta-Ga_2O_3. Using the effective screened medium approach, we successfully obtained a theoretical dielectric constant similar to the experimental values. Unfortunately, the calculations did not reach to an enough width of slab thickness for containing the layers of both tetrahedral and octahedral Ga atoms within the slab system due to its complexity of crystal structure and computational memory problems.

References

[1] T. Kotani, J. Phys. Soc. Jpn. **83**, 094711 (2014); *ecalj*: https://github.com/tkotani/ecalj/.

[2] K. Hyodo et al., accepted in the proceedings CCP2023.

[3] C. Pardede et al., accepted in the proceedings CCP2023.

[4] R. Majumder et al., accepted in the proceedings CCP2023.

[5] M. Obata, T. Kotani, and T. Oda, Phys. Rev. Mater. **7**, 024413 (2023).

[6] J. Luštinec et al., preparing for publication.

[7] JSAP Spring Meeting 2024: 24p-P16-27.

Development of Ceramic Protective Coating for High Corrosion Resistance of Metallic Materials

Yuji Kunisada

Center for Advanced Research of Energy and Materials, Faculty of Engineering, Hokkaido University, Sapporo, Hokkaido 060-8628

In order to develop efficient hydrogen permeation barriers, we investigated the adsorption and diffusion properties of hydrogen isotopes in the vicinity of the interface between different ceramic materials,[1] with the aid of the first-principles calculation based on the density functional theory (DFT). We also investigated the diffusion properties of hydrogen atoms at the grain boundaries of nanocrystalline ceramic materials.

We investigated the absorption energies and diffusion barriers of hydrogen isotopes in the vicinity of the α-Al_2O_3/α-Cr_2O_3 interface using The Vienna Ab initio Simulation Package (VASP). We installed a parallelized VASP with Intel® MPI Library and Intel® Math Kernel Library. We found that hydrogen atoms can form chemical bonds with coordinated oxygen atoms at the stable sites in the α-Al_2O_3 region as well as in the α-Cr_2O_3 region due to interfacial effects. On the other hand, in the transition state, hydrogen atoms cannot form chemical bonds with coordinating atoms. As a result, the diffusion barrier for hydrogen atoms is largest in the α-Al_2O_3 region adjacent to the interface rather than at the interface site. Obtained diffusion barrier is larger than that of the bulk α-Al_2O_3.

We also investigated the diffusion properties of hydrogen atoms at the grain boundaries of nanocrystalline TiN to reveal the effects of the grain boundaries. In grain boundaries, hydrogen atoms are negatively charged and become hydride ions. We found that the diffusion barrier of hydride ions varies significantly depending on the width of the grain boundary. Considering the grain boundary widths observed in the nanocrystalline TiN films prepared by RF magnetron sputtering, it is clear that the nanocrystalline TiN films have higher hydrogen permeability properties than conventional Pd hydrogen permeable films.

These results indicate that the hydrogen permeability of ceramic materials can be significantly changed by controlling the interface.

References

[1] Y. Kunisada, R. Sano, N. Sakaguchi, submitted.

[2] Y. Kunisada, C. Kura, N. Sakaguchi, C. Zhu, H. Habazaki, Y. Aoki, ACS Omega 9 (2024) 13738.

Analysis of incoherent interfaces by DFT calculations

Kazutoshi INOUE[1], Qian CHEN[2], Mitsuhiro SAITO[2], and Yuichi IKUHARA[1,2,*]
[1] *Advanced Institute for Materials Research, Tohoku University, Sendai, Miyagi, 980-8577*
[2] *Institute of Engineering Innovation, The University of Tokyo, Yayoi, Tokyo, 113-8656*

Materials interfaces are two-dimensional defects that significantly affect macroscopic properties due to their local atomic structures. Therefore, it is especially important to identify the stable atomic structure including interfaces, which strongly depends on the misorientation in both ionic and metallic materials. Coherent grain boundaries are classified by the coincidence-site lattice theory. However, it is necessary to effectively approximate the ratio of lattice constants by a rational number for modeling and prediction of incoherent interfaces. For a pair of lattices with a rational ratio of lattice constants, the CSL theory can be easily extended to give a possible pair of commensurate lattices. In this study, atomic models for incoherent grain boundaries were built with a 3D periodic boundary condition. The translation models are systematically constructed by the 0.1 Å steps within the Displacement-Shift-Complete lattice to screen the stable atomic structures. Each model was firstly calculated to obtain grain boundary energy to screen the translation states. The grain boundary energy is the interfacial excess free energy calculated by

$$\Delta E = \frac{1}{2A}\left(E_{\mathrm{total}} - N\sigma_i\right),$$

where E_{total} is the total energy of the system including grain boundaries, σ_i is the energy of the unit cell of the bulk crystal, N is the number of unit cells contained in the supercell, and A is the area of the grain bondary. We applied the first-principles DFT calculations with the plane-wave basis projector-augmented wave method included in VASP to screen and determine the stable atomic structure by using CPU nodes in System B. The generalized gradient approximation was used for the exchange-correlation potentials in the Perdew-Burke-Ernzerhof form, employing an ultrasoft pseudopotential. The cutoff energy was set 600 eV for all plane-wave basis sets. The Brillouin-zone integrations were performed over a $4\times4\times1$ k-point mesh generated by the Monkhorst-Pack scheme. Then, the atomic positions and supercell volumes of the most stable structures among those screened were fully relaxed to ensure that all forces on each relaxed atom were 1.0×10^{-5} eV/Å, and the residual force on each relaxed atom was 0.05 eV/Å under a constant pressure of 0 Pa and a constant temperature of 0 K.

It was anticipated that the longer the periodicity, the more precise the model would be. However, a comparison of the models with long and short periodicity revealed that the grain boundary energy and bandgaps were not dependent on the periodicity, contrary to expectations. Our findings indicate that the long periodicity model can be approximated by a summation of a few short periodicity models, which obeys the rule of approximation of the ratio of lattice constants by a rational number [1].

References

[1] K. Inoue, Q. Chen, K. Kawahara, M. Saito, M. Kotani, Y. Ikuhara: to be submitted (2023).

First-principles study on electron transport properties of heteroatom-doped graphene with adsorbed NO molecules

Yoshiyuki EGAMI
Division of Applied Physics, Faculty of Engineering, Hokkaido University
Kita 13, Nishi 8, Kita-ku, Sapporo, Hokkaido 060-8628

Adsorption of gas molecules on two-dimensional (2D) materials gives rise to significant modifications to atomic and electronic structures of the materials, affecting their electrical conductivity. Graphene is one of the typical 2D materials and shows high conductivity. On the other hand, a pristine graphene is not so suitable as a gas sensor material because the adsorption of gas molecules on the graphene is physisorption which is difficult to modulate the electronic structure of the graphene. Doping graphene with heteroatoms is expected to be the one of promising techniques to increase the detection sensitivity of graphene for adsorbed molecules. Several theoretical studies have shown that nitrogen-containing gas molecules such as NO can chemisorb with the doped heteroatoms and significantly affect the electronic structures of graphene.

In this study, we performed a first-principles study on the modulation in electronic structures and electron transport properties of the doped graphene with molecular adsorption. Here, Al, Si, or N atoms are doped into graphene, in which the ratio of dopant atoms X(=Al, Si, or N) to carbon atoms is 1:3, and NO molecules are adsorbed on the doped atoms. First-principles simulations were carried out using the "RSPACE" code based on the real-space finite-difference formalism[1, 2].

As the results of electronic structure calculations, it was confirmed that the density of states (DOS) near the Fermi level is lower for X=Si than that for X=N or Al. In all systems, the DOS increased in the vicinity of the Fermi level due to the NO molecular adsorption. On the other hand, the electron transport properties were slightly modified for SiC_3, whereas significant modifications in the transport properties were observed for AlC_3 or C_3N. In addition, the influence of the coverage of NO molecules over the graphene on the transport properties was evaluated. For example, in the C_3N system, significant differences in the transport properties were found even when a single NO molecule was adsorbed on the surface consisting of ∼1,000 atoms. This demonstrated the high detection accuracy of adsorbed molecules in the doped graphene.

This work has been performed on System B of the Supercomputer Center, the Institute for Solid State Physics, the University of Tokyo.

References

[1] K. Hirose *et al.*: First-principles calculations in real-space formalism (Imperial College Press, 2005).

[2] Y. Egami, S. Tsukamoto and T. Ono: Phys. Rev. Res. **3**, 013038 (2021).

Electronic properties of the supra-atomic-molecular-orbital-derived band in a solid C_{60}: Theoretical investigation with the GW approximation

Susumu YANAGISAWA
Faculty of Science, University of the Ryukyus
Senbaru 1, Nishihara, Okinawa 903-0213

Fullerenes such as C_{60} have attracted considerable attention as electron transport materials originating from their n−type semiconducting nature. C_{60}, with its soccer-ball molecular shape and thus its spherically high symmetry, has characteristic electronic properties, such as the Supra Atomic Molecular Orbital (SAMO). The SAMO originates from the spherical electronic potential due to the spherical molecular shape, which leads to the Rydberg-like electronic states. The spatial distribution of the wave function with few nodes leads to high electron mobility and free-electron-like nature of the band[1].

In this study, we theoretically estimated the electron mobility of the SAMO-derived band with the first-principles bandstructure calculation. To investigate the nature of the electronic band, we used the GW approximation for bandstructure calculation.

The Projector Augmented Wave (PAW) potential was used, as implemented in the VASP program code, and the valence wave function was expanded by the plane wave basis set with energy cutoff of 1000 eV. The atomic positions and the lattice constants of the C_{60} fcc crystal was optimized with the van der Waals density functional[2]. The 4×4×4 **k**-points were sampled in the Brillouin zone. The spatial distribution of the Kohn-Sham wave function was calculated with the STATE program code.

To calculate the band structure within the GW approximation, the GW space-time code[3] was used. The cutoff energy for the plane wave was 734 eV, and the unoccupied bands for calculating the Green's functions encompassed 440 eV above the Fermi level. The program code allows to calculate the GW band energies of arbitrary **k**-points without the Wannier interpolation. Inclusion of the many-body effect based on the zeroth-order wave functions and band energies, *i.e.* the one-shot GW, was conducted, by using the one-particle solutions obtained with the generalized gradient approximation (GGA) level of theory.

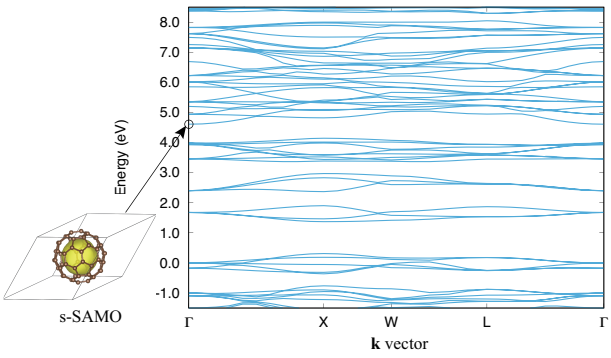

Figure 1: Band dispersion of C_{60} obtained with GGA, along with the spatial distribution of the s-SAMO wave function.

The optimized lattice constant of the C_{60} fcc crystal structure was 14.12 Å, in good

agreement with the experimental value of 14.3 Å measured at room temperature[4]. The band dispersion obtained with GGA level of theory indicates the parabolic band structure of the s-SAMO-derived band (Fig. 1), implying the suggested free-electron-like nature of the band. The effective electron mass estimated with the curvature of the band was 0.71, relative to the electron rest mass.

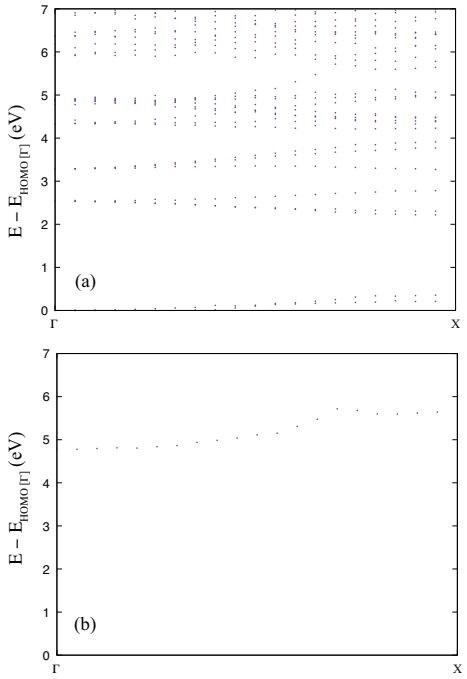

Figure 2: Band dispersion of C_{60} obtained with GW: (a) overall band structure, (b) s-SAMO derived band only.

By the many-body effect within the GW approximation, the calculated band gap was 2.0 eV, in fair agreement with the experimental value of 2.4 eV[5] (Fig. 2). It was found that compared to the band dispersion obtained with GGA the s-SAMO derived band shifted down relative to the other bands. The s-SAMO derived band obtained within GW (see Fig. 2 (b)) showed a parabolic band structure around the Γ-point, similarly to that obtained with GGA. The effective mass was estimated to be 1.13. The larger effective electron mass than that of GGA is consistent with the free-electron nature of the band: the polarization cloud attracts back the injected charge, which decreases the mobility of the charge compared to the free electron[6].

While the effective mass estimated within GW was consistently elucidated, the downward shift of the s-SAMO band by inclusion of the many-body effect needs consideration. Further investigation is in progress, *i.e.* further consistent inclusion of the many-body effect by the evGW approach.

References

[1] J. O. Johansson, E. Bohl, and, E. E. B. Campbell: Phil. Trans. R. Soc. A **374**, 20150322 (2016).

[2] I. Hamada: Phys. Rev. B **89**, 121103 (2014).

[3] M. M. Rieger et al., Comput. Phys. Commun. **117**, 211 (1999); L. Steinbeck et al., Comput. Phys. Commun. **125**, 105 (2000); C. Freysoldt et al., Comput. Phys. Commun. **176**, 1 (2007).

[4] K.-D. Tsuei et al., Phys. Rev. B **56**, 15412 (1997).

[5] A. Sugie et al., J. Phys. Chem. Lett. **14**, 11412 (2023).

[6] C. Friedrich, S. Blügel, and D. Nabok, Nanomaterials **12**, 3660 (2022).

Non-adiabatic excited-state time-dependent *GW* molecular dynamics simulation of photolysis of methane using TOMBO

Kaoru OHNO[1] and Aaditya MANJANATH[2]

[1]*Graduate School of Engineering, Yokohama National University*

79-5 Tokiwadai, Hodogaya-ku, Yokohama, Kanagawa 240-8501

[2]*Research Center for Structural Materials, National Institute for Materials Science*

1-2-1 Sengen, Tsukuba, Ibaraki 305-0047

There is a longstanding difficulty that time-dependent density functional theory relying on adiabatic local density approximation is not applicable to electron dynamics of an initially excited state such as in photochemical reactions. To overcome this, we developed non-adiabatic excited-state time-dependent *GW* (TD*GW*) molecular dynamics on the basis of the extended quasiparticle (QP) theory. Replacing Kohn-Sham energies with QP energies allows the full correspondence to excited-state surfaces and corresponding total energies, with satisfying extended Koopmans' theorem. Besides our other work [1-4], we demonstrated the power of TD*GW* using methane photolysis, $CH_4 \rightarrow CH_3^{\cdot} + H$, an important initiation reaction for combustion/ pyrolysis and hydrogen production of methane [5]. We successfully explored several possible pathways and showed how this reaction dynamics is captured accurately through simultaneously tracing all QP levels and orbitals (Fig. 1). TDGW scales as $O(N_B{}^{3-4})$, where N_B is the number of basis functions, which is distinctly advantageous to performing dynamics using configuration interaction and coupled cluster methods.

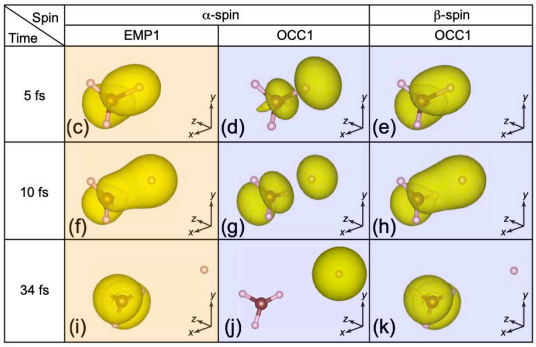

Fig. 1: Temporal change of QP orbitals in the reaction $CH_4 \rightarrow CH_3^{\cdot} + H$ at the excited state [5].

References

[1] T. Ohtsuki, R. Kuwahara, and K. Ohno, Phys. Rev. C **108** (2023) L011301.

[2] Z. Hajiahmadi, 8 人省略, and K. Ohno, Comp. Mat. Sci. **228** (2023) 112364.

[3] M. Khazaei, 10 人省略, K. Ohno, 3 人省略, J. Phys. Chem. C **127** (2023) 14906-14913.

[4] R. Kuwahara, K. Ohno, and T. Ohtsuki, Phys. Rev. C **109** (2024) 024609.

[5] A. Manjanath, R. Sahara, K. Ohno, and Y. Kawazoe, J. Chem Phys, **160** (2024) to appear.

Structural exploration and prediction of dielectric properties of molecular materials

Shinji TSUNEYUKI

Department of Physics, The University of Tokyo

Hongo, Bunkyo-ku, Tokyo 113-0033

In recent years, the need to calculate the dielectric properties of materials in the THz range has increased due to expectations for industrial applications. In this frequency range, changes in electronic states and polarization associated with lattice vibrations are essential, and there are many issues to be solved to treat them from first principles. Therefore, we are developing a predictive method of calculating complex permittivity using first-principles electronic structure calculation based on density functional theory, lattice dynamics calculation, molecular dynamics method, machine learning, etc. This academic year, we developed a method to calculate the complex permittivity of molecular liquids with high accuracy, with the application to polymers in mind.

Previously, we combined the lattice dynamics calculation incorporating anharmonic effects and the Born effective charges to calculate complex permittivity of crystals [1]. However, polymeric materials and molecular liquids have huge structural fluctuations that determine the dielectric constant, making it challenging to apply the above method, which starts from harmonic vibrations around the equilibrium point.

In such cases, if the time variation of the system's structure over a long period can be calculated by molecular dynamics, and if the dipole moment of the whole system at each time can be calculated, the dielectric constant is obtained from the time correlation function of the dipole moment by linear response theory. The dipole moments vary greatly depending not only on the internal structure of the constituent molecules but also on the interactions between the molecules, so they must be estimated by first-principles calculations rather than simple models such as classical fixed-charge models.

A problem here is that the computational cost of the dipole moments from first principles is very high; it is challenging to calculate the correlation function over a long period. Therefore, we developed a machine learning model that predicts the position of the Wannier center for each chemical bond from the results of short-time first-principles molecular dynamics calculations. This model is more versatile than the Wannier centroid machine learning model proposed in earlier works and

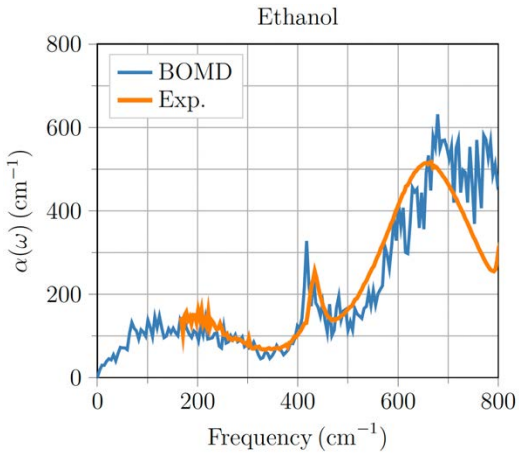

Fig.1 Infrared absorption coefficients of liquid ethanol at room temperature calculated from first principles (a blue line) and their experimental values (a smooth orange line, taken from Ref. [4]). The calculated values agree well with the experimental data by correctly evaluating the polarization due to intermolecular interactions.

can be applicable to larger molecules. By combining this model with the trajectory simulations by the classical or first-principles molecular dynamics methods, we successfully calculated the dielectric properties of liquid methanol, ethanol, propylene glycol (PG), PG dimers and 14-mers in the THz range within a realistic calculation time (see Fig.1) [2,3]. The method developed in this study will be helpful in the study of molecular or polymeric dielectric materials due to its excellent prediction capability.

This study was conducted in collaboration with JSR Corporation.

References

[1] T. Amano, T. Yamazaki, R. Akashi, T. Tadano and S. Tsuneyuki, Phys. Rev. B, 107, 094305 (2023).

[2] T. Amano, PhD Dissertation, The University of Tokyo (2024).

[3] T. Amano, T. Yamazaki and S. Tsuneyuki, to appear in Proceedings of the 34th IUPAP Conference on Computational Physics (CCP2023).

[4] E. Sani and A. Dell'Oro, Optical Materials 60, 137 (2016).

Thermal Properties of the Element and Binary Oxides toward Negative Thermal Expansion from First Principles

Yasuhide MOCHIZUKI

Department of Materials Science and Engineering,

Tokyo Institute of Technology, Ookayama, Meguro-ku, Tokyo 152-8550

Negative thermal expansion (NTE) materials have been vigorously studied for more than a century and are applied to many industrial applications such as heat resistance fillers, microdevices in light-emitting diodes (LED), large-scale integration (LSI), power semiconductors, and micropositioners in the telescopes. Although a tremendous amount of work on LTE and NTE materials has been dedicated so far [1], a comprehensive study showing the chemical aspects and materials-design concepts for realizing LTE and NTE behaviors is lacking. Specifically, it remains unclear as a nontrivial problem how we design LTE or NTE materials with various combinations of the elements. These fundamental uncertainties stem from unclear correlations between the thermal expansion coefficients and related parameters of crystals.

In this study, we present the systematic calculation results of thermal properties, namely, volumetric thermal expansion coefficients α_V, bulk moduli B_T, average atomic volumes V, and Grüneisen parameters γ for the 46 unary solids and 45 binary oxides through first-principles lattice-dynamics calculations using quasi-harmonic approximation (QHA). We provide a formulation of α_V based on the Mie─Grüneisen equation of states. From the analytic formulation of α_V, we thoroughly analyze the correlations between α_V, B_T, V, and γ using the calculation results.

The first-principles calculations were carried out using the projector augmented-wave (PAW) method [2] and the PBEsol functional [3] within the generalized gradient approximation as implemented in VASP [4]. The phonon dispersions were derived from the calculated force constants using PHONOPY [5]. Here, to derive the force constants, we adopted a 2×2×2 supercell for the cubic, rhombohedral, tetragonal, orthorhombic, and monoclinic structures, while a 3×3×2 supercell was used for the hexagonal structures. As an exception, we calculated the force constants of Cu_2O ($Pn\bar{3}m$) by expanding the supercell as 4×4×4 because the negative α_V were largely overestimated in the results from the 2×2×2 and 3×3×3 supercells. We did not calculate the thermal properties when a crystal structure has imaginary phonon modes because free energy calculations are unavailable. For the calculations through QHA, we isotropically

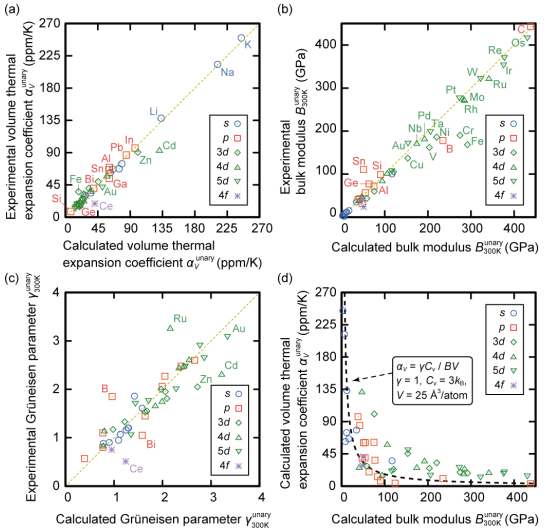

Fig. 1: Validations of the calculated (a) volumetric thermal expansion coefficients α_V, (b) bulk moduli B_T, and (c) Grüneisen parameters γ by using QHA compared to the experimental values. (d) Our calculated α_V as a function of B_T.

changed the relaxed lattice constants as −5 to +5% in the unary solids and −0.66 to +0.66% in the binary oxides. Here, in the calculations for the partially occupied 3*d* transition-metal oxides, we used the Dudarev formulation of +*U* correction with the antiferromagnetic configurations to obtain the dynamically stable phases. We applied the +*U* corrections for the on-site 3*d* electrons in V, Cr, Fe, and Ni as 3, 3, 4, and 7 eV, respectively.

We present the calculated and experimentally reported thermal expansion coefficients α_V, bulk moduli B_T, and Grüneisen parameters γ of the elements at 300 K (Figure 1a–c). The calculated and experimental values validate the predictability and accuracy of the QHA employed in this work. Additionally, Figure 1d shows that the α_V is determined mainly by the B_T, which has an inverse correlation with α_V. We also found that (i) a crystal possessing large *V* tends to have small B_T; (ii) the α_V of complex compounds tend to be large (small) when they are composed of the element with large (small) α_V; (iii) the major role of γ, which is ruled by the crystal structures and coordination environment, is the determination of the sign of α_V; (iv) the transverse-acoustic (TA) and/or low-frequency phonons are responsible for the negative thermal expansion behaviors; and (v) the NTE materials prefer the relatively large *V*, possessing negative mode Grüneisen parameters γ_{qv} [6].

References

[1] M. T. Dove and H. Fang, *Rep. Prog. Phys.* **79**, 066503 (2016).

[2] P. E. Blöchl, *Phys. Rev. B* **50**, 17953 (1994).

[3] J. P. Perdew *et al.*, *Phys. Rev. Lett.* **100**, 136406 (2008).

[4] G. Kresse and J. Furthmüller, *Phys. Rev. B* **54**, 11169 (1996); G. Kresse and D. Joubert, *ibid* **59**, 1758 (1999).

[5] A. Togo and I. Tanaka, *Scr. Mater.* **108**, 1 (2015).

[6] Y. Mochizuki, H. Koiso, K. Nagamatsu, S. Bae, T. Isobe, A. Nakajima, *J. Phys. Chem. C* **128**, 525 (2024).

Elucidating the Thermal Transport Mechanisms at Semiconductor Interfaces

Xu Bin

Department of Mechanical Engineering,

The University of Tokyo, 7-3-1, Hongo, Bunkyo-ku, Tokyo 113-8656

Semiconductor two-dimensional material heterostructures are widely used in manufacturing highly integrated, multi-interface electronic devices due to their excellent electronic, photonic, thermoelectric, and superconducting properties. However, heat dissipation at the interface between the substrate and two-dimensional material is a critical bottleneck for further device miniaturization and power-density improvement, significantly impacting device functionality, reliability, and failure thresholds. Thus, understanding the interfacial thermal transport of phonons is crucial for optimizing the performance and reliability of semiconductor-based devices.

This work combines experiments with molecular dynamics simulations to study the impact of phonon transport states on interfacial thermal transfer. Notably, during the molecular dynamics simulations, we employed a machine learning potential function to accurately describe the interactions between atoms. The time-domain thermoreflectance experimental model and the molecular dynamics simulation model are shown in Fig. 1(a) and (b), respectively.

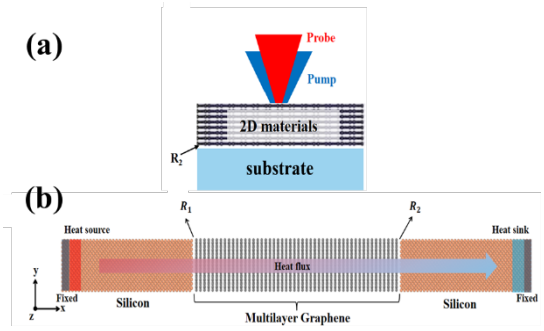

Figure 1 The thermal boundary conductance measurement schematic diagram of multilayer graphene-silicon substrate structure. (a) Non-transducer TDTR measurement setup and (b) Molecular dynamics simulation structure.

Fig. 2 shows the relationship between thermal boundary conductance and the thickness of multilayer graphene, while the inset calculates the average mean free path of graphene in the c-axis direction. The thermal boundary conductance increases with the thickness of graphene and gradually converges when the thickness reaches the average mean free path of graphene. The change in thickness dependency indicates a shift in the phonon transport state. This study bridges the gap between phonon transport mechanisms and thermal boundary conductance.

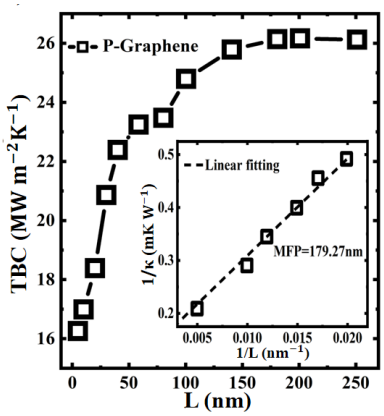

Figure 2 Thickness-dependent thermal boundary conductance of heterostructures

Reference

[1] J. Yue, S. Hu, B. Xu, R. Chen, L. Xiong, R. Guo, Y. Li, . Nian, J. Shiomi, and B. Zheng, Unraveling the mechanisms of thermal boundary conductance at the graphene-silicon interface: Insights from ballistic, diffusive, and localized phonon transport regimes, Phys. Rev. B **109**, 115302 (2024)

First-principles NEB calculations of proton tautomeric conduction pathways

Hatsumi MORI and Kaito NISHIOKA

The Institute for Solid State Physics,

The University of Tokyo, Kashiwa-no-ha, Kashiwa, Chiba 277-8581

We have been developing materials and elucidating the conduction mechanism in order to establish design guidelines for anhydrous superproton conductors, which are highly efficient proton conductors even without humidification [1-4]. Recently, we have discovered an anhydrous superproton conductor with a novel mechanism called "proton tautomerism", in which intramolecular protons are transferred in correlation with the bond recombination of π electrons. This mechanism replaced the conventional proton conduction mechanism by molecular motion with a high activation barrier and, in fact, led to the discovery of 1,2,3-triazolium dihydrogen phosphate (1,2,3-$TrzH^{+}$•$H_2PO_4^{-}$) single crystal.

The conduction mechanism of this system was investigated by ab initio Nudged Elastic Band (NEB) calculations by utilizing ISSP supercomputer. Assuming a perfect crystal, the calculated proton pathway based on proton tautomerism gave much higher activation energies than those of the experimental pathway. The ab initio molecular dynamics (MD) calculations also suggest that intermolecular proton transfer does not occur in a perfect crystal without proton defects. Therefore, proton pathways with lower barriers should be explored.

In this project, we performed ab initio NEB calculations on 1,2,3-$TrzH^{+}$•$H_2PO_4^{-}$ crystals with excess protons and proton defects in order to clarify the relationship between the conduction mechanism and proton tautomerism in this system. Then, the energy curves of single proton cycles in the crystals, namely long-range conduction pathway, were obtained.

NEB calculations for the conduction pathway with excess-proton-sites crystals have afforded the activation energy, which is good agreement with the experimental ones, unlike the case of perfect crystals. We first optimized four types of local minimum structures independently under the periodic boundary condition of a single unit cell. The transient structures obtained from the NEB calculations visually revealed the tautomerization process from the initial state to the final state. The activation energies for each of these processes involving proton tautomerism of (1,2,3-$TrzH^{+}$) assisted by ($H_2PO_4^{-}$) were estimated to be 1.048, 1.000, 0.846, and 1.034 eV. The activation energies are consistent with the experimentally obtained activation energy (~1 eV) from the temperature dependence of proton conductivity. Similarly,

for crystals with introduced proton defects, the activation energy associated with the proton tautomerism of (1,2,3-$TrzH^+$) assisted by ($H_2PO_4^-$) is consistent with the experimental value. These calculations strongly support that the proton conduction of 1,2,3-$TrzH^+$•$H_2PO_4^-$ is realized by the proton tautomerism on 1,2,3-$TrzH^+$.

References

[1] Y. Sunairi, S. Dekura, H. Mori et al., J. Phys. Soc. Jpn. **89**, 051008 (2020).

[2] Y. Hori, S. Dekura, H. Mori et al., J. Phys. Chem. Lett. **12**, 5390(2021).

[3] S. Dekura, H. Mori et al., Solid State Ionics **372**, 115775(2021).

[4] S. Dekura, M. Mizuno, H. Mori, Angew. Chem. Int. Ed. **61**, e202212872(2022).

First-principles study of phonon dynamics in all-inorganic halide perovskites

Terumasa TADANO
Center for Magnetic and Spintronic Materials, National Institute for Materials Science
Sengen, Tsukuba, Ibaraki 305-0047

All-inorganic halide perovskites $CsBX_3$(B=Sn,Pb;X=Cl,Br,I) have been studied intensively in recent years due to their unique physical properties, including high photovoltaic performance, ultralow thermal conductivity, and strong phonon damping near the structural phase transition [1]. However, elucidating and predicting these phonon-related properties of the halide perovskites quantitatively and consistently using first-principles calculations remain challenging as an accurate description of the potential energy landscape is required.

In this project, we have investigated how well the cutting-edge phonon calculation methods combined with density functional theory (DFT) predict the phonon linewidth, lattice thermal conductivity (LTC), and structure phase transition temperature (T_s) of the all-inorganic halide perovskites.

First, we calculated the renormalized phonons at the mean-field level theory, i.e., the first-order self-consistent phonon (SC1). To obtain a better one-body phonon picture, we further considered the bubble self-energy correction within the quasiparticle approximation (SC1+Bubble) following Ref. [2]. By using each renormalized one-body phonon Hamiltonian, we then calculated the phonon linewidth Γ_q by considering the three-phonon $\Gamma_q^{\rm 3ph}$ and four-phonon $\Gamma_q^{\rm 4ph}$ scattering processes. We found that the calculated Γ_q values were consistent with the experimental values only when we included the four-phonon scattering channel using the SC1+Bubble one-body Hamiltonian. However, even with the Γ_q values that were closest to the experimental linewidth, the LTC values computed using the Wigner formula underestimated the experimental values. This suggests a potential failure of the quasiparticle approximation in the Wigner theory, which is expected to be solved by employing the Kubo formula.

Second, we calculated the T_s value of the cubic-to-tetragonal phase transitions for $CsPbBr_3$ by applying the Curie-Weiss law to the temperature-dependent soft phonon frequencies. We fixed the lattice constant to the experimental value and estimated T_s using LDA, GGA (PBE, PBEsol), and meta-GGA (r^2SCAN). We found that LDA gave the lowest T_s value, which slightly underestimated the experimental value, and PBEsol T_s agreed nicely with the experimental value. On the other hand, PBE and r^2SCAN greatly overestimated T_s. Our study supports the common belief in the community that PBEsol is a better choice for predicting structure and phonon properties, but further investigation is still needed to find a best practice for the T_s prediction.

References

[1] E. Fransson *et al.*, Commun. Phys. **6**, 173 (2023).

[2] T. Tadano and W. A. Saidi, Phys. Rev. Lett. **129**, 185901 (2022).

Crystal Structure Prediction of Li-ion Solid Electrolyte Materials

Tomoki YAMASHITA
Department of Electrical, Electronics and Information Engineering,
Nagaoka University of Technology
Kamitomioka-machi, Nagaoka, Niigata, 940-2188

We have studied the structural stability of $Li_{4x}Mg_{2(1-x)}P_2O_7$ that can be a candidate material for solid electrolyte of Li-ion batteries. Crystal structure prediction simulations with CrySPY [1] and structure generation by cation substitution were performed to evaluate the phase stability of $Li_{4x}Mg_{2(1-x)}P_2O_7$. We employ the density functional theory (DFT) using the VASP code [2]. PBEsol was used as the exchange-correlation functional. We found that the structure with the same P_2O_7 framework as $Li_{2.2}Zn_{0.8}P_2O_7$ exhibits the lowest formation energy. Our results agree well with the experimental results.

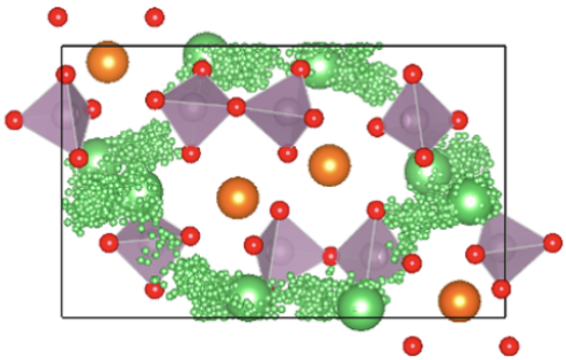

Figure 1: Li diffusion for $Li_2MgP_2O_7$. The small spheres represent the diffusion of Li.

Moreover, first-principles molecular dynamics calculations were performed for the stable P_2O_7 framework by varying the compositions of Li and Mg. Here the vasp code and PBEsol were used. The NVT ensemble was adopted for molecular dynamics calculations, and temperature control was achieved using the Nosé-Hoover [3] method, with temperatures set at 300, 700, 1000, and 1500 K. The time step for calculations was set to 2.0 fs, and the total simulation time was 30 ps.

The calculation results showed that for the $Li_4P_2O_7$ composition ($x = 1.0$), the Li atoms did not diffuse significantly. This is because the structure became too congested with Li, leaving no room for diffusion. On the other hand, in the case of $Li_2MgP_2O_7$ ($x = 0.5$), Li atom vacancies are created due to the substitution of one divalent Mg atom and two monovalent Li atoms, leading to making Li diffusion easier as shown in Fig. 1. In the $Li_{4x}Mg_{2(1-x)}P_2O_7$ system, controlling the conductivity of Li ions by substituting them with multivalent atoms is possible.

References

[1] T. Yamashita, S. Kanehira, N. Sato, H. Kino, H. Sawahata, T. Sato, F. Utsuno, K. Tsuda, T. Miyake, and T. Oguchi, Sci. Technol. Adv. Mater. Meth. **1** (2021) 87.

[2] G. Kresse and J. Hafner, Phys. Rev. B **47**, 558 (1993).

[3] W. G. Hoover, Phys. Rev. A **31**, 1695 (1985).

Response of nanographene device structures to external fields

Koichi KUSAKABE
Graduate School of Science, University of Hyogo
Kouto, Kamigori, Hyogo 5-8581

1 Introduction

To discover effective applications for quantum computation and spintronics of atomic layer materials, we are studying graphene-based quantum computation resources,[1, 2] and atomic-layer-material-based spin-electronic devices.[3] We have developed theoretical approaches to study enhanced functions of a bio-sensor made of adsorbed linkers on graphene in solvents,[4] and light-induced structural transformation of nano-scale material structures.[5]

2 New quantum computation resources by poly-PTM

We designed a two-dimensional $S = 3/2$ Heisenberg system by combining stable S=3/2 spin states on nanographene with antiferromagnetic interactions that exhibit sufficient strength. For this purpose, we have shown that the design method using poly-PTM is appropreate and much better than recent attempts by disjoint non-bonding molecular orbital method.

3 Functions and responses of atomic-layer devices

Optical experiments have confirmed that when multiple boron vacancies in hBN are selectively generated, ferromagnetically aligned magnetic moments appear. Calculations by Harfah *et al.*[3] have revealed that TMRs in excess of 400 can occur in vertical spintronics devices in which graphene is sandwiched between these magnetic hBN layers and Cu electrodes are further stacked on both sides.

Recently, optical responses of Bi_2Se_3 is detected by a pump-probe measurement method using the photoelectron emission microscope (PEEM). We analyzed the electronic local density of state at various surfaces focusing on the depth dependence from the surface.[6] The results indicate that detailed dependencies on atomic stacking are reflected in the PEEM data.

Acknowledgement

The author acknowledges strong collaboration with Dr. N. Morishita, Mr. K. Komatsu, and Prof. M. Kitatani on nanographene quantum computation resorces. He also thanks Dr. Y. Wicaksono, Dr. H. Harfah, Dr. G. K. Sunnardianto, and Prof. M. A. Majidi for fruitful collaboration on spintronics devices.

References

[1] N. Morishita, Y. Oishi, T. Yamaguchi, K. Kusakabe, Appl. Phys. Express **14**, 121005 (2021).

[2] K. Komatsu, N. Morishita, M. Kitatani, K. Kusakabe, preprint.

[3] H. Harfah, Y. Wicaksono, G. K. Sunnardianto, M. A. Majidi, and K. Kusakabe, Phys. Chem. Chem. Phys., **26**, 9733 (2024).

[4] Y. Oishi, M. Kitatani, and K. Kusakabe, Beilstein J. Org. Chem., **20**, 570 (2024).

[5] M. Nagai, Y. Higashitani, M. Ashida, K. Kusakabe, H. Niioka, A. Hattori, H. Tanaka, G. Isoyama, N. Ozaki, Commun. Phys., **6**, 88 (2023).

[6] K. Fukumoto, S. Lee, S. Adachi, Y. Suzuki, K. Kusakabe, R. Yamamoto, M. Kitatani, K. Ishida, Y. Nakagawa, M. Merkel, D. Shiga and H. Kumigashira, preprint.

HPC-based fusion of quantum simulation, experiment analysis and data-driven science

Takeo Hoshi[1,2]

[1] *National Institute for Fusion Science,*

322-6 Oroshi-cho, Toki city, Gifu Prefecture, 509-5292, Japan.

[2]*Slow Positron Facility, Institute of Materials Structure Science, High Energy Accelerator Research Organization (KEK), Oho 1-1, Tsukuba, Ibaraki, 305-0801, Japan.*

Several new features were added in 2DMAT [1-6], an open-source data-analysis software for advanced experimental measurement techniques. 2DMAT was developed by the PASUMS project at FY2020, 2021[1]. A major achievement was the efficient massively parallel computation of the population annealing Monte Carlo (PAMC) method [7]. An almost ideal parallel efficiency was found not only on the ISSP supercomputer (ohtaka) but also on the Fugaku supercomputer with upto 8×10^5 nodes, a half of the Fugaku supercomputer. We used 2DMAT for the data analysis of total-reflection high-energy positron diffraction (TRHEPD) at Slow Positron Facility, KEK [8]. The experimental setup of TRHEPD is similar to that of reflection high-energy electron diffraction (RHEED) but TRHEPD reveals the surface sensitivity and was used for the determination of surface structure. 2DMAT was applied to the analysis of the three-dimensional coordinates (x, y, z) for Ge(001)-c4x2 surface structure by the Bayesian inference using PAMC. [8] The PAMC analysis, as a global search, determined the correct surface structure without any initial guess. In addition, a new algorithm was proposed for a faster computation of the forward problem of TRHEPD analysis. [9]

References

[1] https://www.pasums.issp.utokyo.ac.jp/2DMAT

[2] K. Tanaka, *et al*. (T. Hoshi), Acta. Phys. Pol. A 137, 188 (2020).

[3] T. Hoshi, *et al*. (T. Hoshi), Comp. Phys. Commun. 271, 108186 (2022).

[4] T. Hanada, *et al*., Comp. Phys. Commun. 277 108371 (2022).

[5] Y. Motoyama, *et al*. (T. Hoshi), Comp. Phys. Commun. 280, 108465 (2022).

[6] K. Tanaka, *et al*. (T. Hoshi), JJAP Conf. Series 9, 011301 (2023).

[7] K. Hukushima, Y. Iba, AIP Conf. Proc. 690, 1604 (2003).

[8] https://www2.kek.jp/imss/spf/eng/

[9] S. Kudo *et al.*, (T. Hoshi), Comp. Phys. Commun. 296, 109029 (2024).

Computational Design of Novel Functional Materials and Catalysts for Energy-related Applications

Tetsuya TAKETSUGU

Department of Chemistry, Faculty of Science

Hokkaido University, N10W8, Kita-ku, Sapporo 060-0810

The main goal of this project is to develop a number of innovative real functional materials for energy and environment-related applications using computational approach. The density functional theory (DFT) methods as implemented in the VASP and Quantum Espresso software packages were used. The following main results were achieved:

1) Electrocatalytic activity of Au electrodes decorated by the size selected h-BN nanosheet (BNNS) for the oxygen reduction reaction (ORR) was investigated. It was demonstrated that the overpotential is reduced by all the BNNS modifications, and the smaller the size, the smaller the overpotential for ORR, i.e., the larger the ORR activity, in this size range. Our theoretical analysis of the change in free energy (Fig. 1) reveals that the ORR active sites are located at the edges of BNNS islands adsorbed on Au(111). The decrease in size of BNNS islands results in an increase in the number of the catalytically active sites and, hence, in the increase in the catalytic activity of the BNNS/Au(111) system.

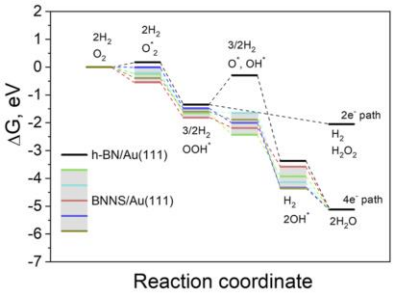

Fig. 1: Free energy diagram ORR calculated for the pristine h-BN monolayer on the Au(111) surface (black line) and small OH-terminated BNNS on Au(111) [1].

We have also explored the activity of the h-BN-based model catalyst for the methanol decomposition reaction. It was found that the methanol decomposition pathway consists of three-step processes (Fig.2). We found that the methanol interaction with the oxidized boron site leads to the H-transfer reaction and this is a crucial condition to initiate the decomposition reaction.

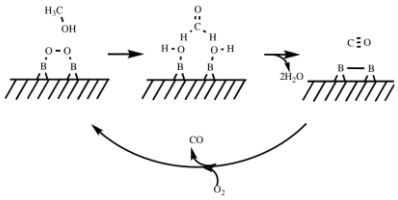

Fig. 2: Methanol decomposition over metal-free catalyst with >B-O-O-B< active sites.

2) Using the extensive large-scale DFT calculations we have modeled complicated molecular rotations in the newly developed molecular crystal consisting of triaryltriazine molecular rotor confined in a bulky crystalline phase (Fig. 3). We have demonstrated that the phenylene units of the crystalline rotors display two different and interconvertible correlated molecular motions [2] and it is possible to switch between these intermolecular geared rotational motions via a thermally induced crystal-to-crystal phase transition.

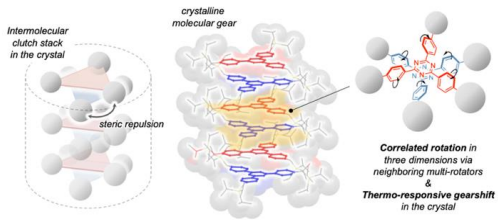

Fig. 3: A Steric-Repulsion-Driven clutch stack of triaryltriazines [2].

3) We performed a systematic investigation on the formation mechanism of complex organometallic oligomers on Cu(111) surface via bonding of phenanthroline derivatives by multiple Cu atoms (Fig. 4). Our DFT calculations revealed the important role of the Cu adatoms in the linking of enantiomers of the chiral oligomers [3]. This finding may help to increase the variety of organometallic nanostructures on surfaces.

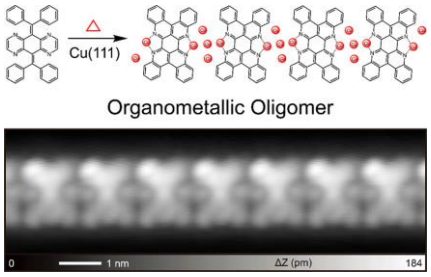

Fig. 4: Organometallic oligomer on Cu(111) surface [3].

4) Using large-scale DFT calculations we have investigated the mechanism of molecular passivation for improving the performance and operation stability of halide perovskite solar cells (HPSCs) [4]. We reveal discernible effects of diammonium molecules onto Methylammonium-free perovskites.

References

[1] H. C Dinh, G, Elumalai, H. Noguchi, A. Lyalin, T. Taketsugu, and K. Uosaki, J. Chem. Phys. **158**, 134713 (2023).

[2] M. Jin, R. Kitsu, N. Hammyo, A. Sato-Tomita, M. Mizuno, A. S. Mikherdov, M. Tsitsvero, A. Lyalin, T. Taketsugu, and H. Ito, J. Am. Chem. Soc. **145**, 27512-27520 (2023).

[3] K. Sun, K. Sugawara, A. Lyalin, Y. Ishigaki, K. Uosaki, O. Custance, T. Taketsugu, T. Suzuki, and S. Kawai, ACS Nano **17**, 24355-24362 (2023).

[4] D. B. Khadka, Y. Shirai, M. Yanagida, H. Ota, A. Lyalin, T. Taketsugu, and K. Miyano, Nat. Commun. **15**, 882 (2024).

First-Principles Molecular-Dynamics Study of Structural and Electronic Properties of Disordered Materials under Extreme Conditions

Fuyuki SHIMOJO

Department of Physics, Kumamoto University, Kumamoto 860-8555

To investigate the structural and dynamic properties of covalent liquids and glasses, such as SiO_2, calculations on a large number of atoms are required to reproduce their disordered atomic arrangement. However, accurate first-principles molecular dynamics (FPMD) simulations are limited for rather small systems because of the high calculation cost. One of solutions would be to use machine-learning interatomic potential based on artificial neural networks (ANN) trained from the results of FPMD simulations.

It has been known that the ANN calculations for enlarged systems are prone to instability when training data are insufficient. In the case of SiO_2 glass, we have found that potential averaging and active learning are useful to avoid computational instability efficiently [1]. The FPMD data were prepared with a system of 144 (48Si + 96O) atoms under periodic boundary conditions. We generated two models of the glass states at pressures of 0 and 60 GPa. For each pressure, simulations of liquid states were performed at several thousand kelvin, and subsequent calculations were carried out to 300 K by gradually lowering temperature. For the MD simulations with ANN potentials, a system of about 30,000 atoms was used. Figure 1 shows the comparison of partial pair distribution functions between the ANN-potential and FPMD calculations at aombient conditions. The profiles are in agreement with each other, indicating that the glass state of SiO_2 was succesfully reproduced using the fairly large system.

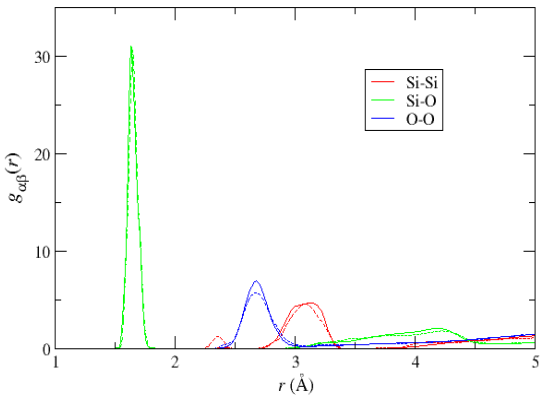

Fig. 1: Partial pair distribution function of SiO_2 glass at ambient conditions. The solid and dashed lines show the ANN-potential and FPMD calculations, respectively.

References

[1] D. Wakabayashi *et al.*, J. Phys. Soc. Jpn. **92**, 074002 (2023).

[2] E. Ryuo, *et al.*, Phys. Rev. B **96**, 054206 (2017)

Thermal Conductivity calculation with machine-learning interatomic potential for multi-component heterogeneous materials II

Kohei Shimamura

Department of Physics,

Kumamoto University, 2-39-1 Kurokami, Chuo-ku, Kumamoto 860-8555

The thermal conductivity calculation method based on the Green-Kubo (GK) formula can be applied to any materials, but require highly accurate interatomic potentials due to its high computational cost. Machine-learning interatomic potentials (MLIPs) constructed by training first-principles molecular dynamics data satisfy the high accuracy and low computational cost, so the combination with the GK formula has become applicable to many materials.

However, for materials with complex interactions, such as multi-component systems, the accuracy of the heat flux included in the GK formula is problematic. Since the heat flux cannot be the training target for MLIPs, an unphysical heat flux that depend on the training method are mixed in. This unphysical heat flux should not analytically affect the total thermal conductivity, but numerically it can cause errors to not only the total but also partial conductivities. For example, differences in the initial parameters of the machine learning models can cause variations in the obtained thermal conductivities.

To prevent heat flux bloat due to the unphysical heat flux, we proposed a training method using heat flux regularization [1]. The heat flux regularization works to reduce the heat flux as much as possible during training. The heat flux consists of atomic energy, atomic force, atomic pressure, and atomic velocity. Since these can be used during training, the heat flux can actually be defined during training. The intensity adjustment of this regularization can be determined by ensuring that both the regularization term and the root mean square errors of training targets (e.g. total potential energy, (total atomic) force, and total pressure) take small values.

The regularization would improve the accuracy of partial thermal conductivities such as atomic thermal conductivities and components in frequency space, which have been difficult in the thermal conductivity calculation based on the GK formula, and would be useful in the elucidation for the origin of thermal conductivity.

References

[1] K. Shimamura, *et al.*: Comp. Phys. Commun. **294**, 19258 (2024).

First-Principles Calculations of Altermagnetic Materials

Kunihiko Yamauchi
Center for Spintronics Research Network, Osaka University, Toyonaka, Osaka 560-8531, Japan

We have studied altermagnetic materials by means of first-principles DFT calculations using VASP and Wannier90 codes. Altermagnetism is a new type of magnetism that exhibits SOC-free spin splitting and some properties common to ferromagnetism despite the compensated magnetization. Previously, we have investigated the spin-split bandstructure and the anomalous Hall effect in perovskite $CaCrO_3$ [1]. This year, we focused on MnTe, in which the large spin splitting ($\Delta E \sim 1$ eV) appears in the bandstructure with a high Neel temperature ($T_N = 307$ K). In collaboration with the micro ARPES measurement, we found that the bandstructure in the antiferromagnetic phase exhibits the strongly anisotropic spin splitting of the bands associated with the time-reversal-symmetry breaking and provided a direct experimental evidence for the altermagnetic spin splitting [2]. When the Mn spins lie in the hexagonal ab plane, C_{3z} symmetry is broken but antiunitary C'_{2d} symmetry is kept to relate the up-spin and down-spin states as shown in Fig. 1. The spin-splitting bandstructure shows the good agreement with the ARPES result.

In addition, we worked on a hydrogen-induced metal-insulator transition in $SmNiO_3$ [3] and newly found a charge-ordered structure. We also studied 2D magnetic materials and confirmed that the Goodenough-Kanamori-Anderson rules stand in monolayer transition-metal chlorides, in which the d_{xy} and $d_{x^2-y^2}$ orbital states play an important role in the super-exchange interaction [4].

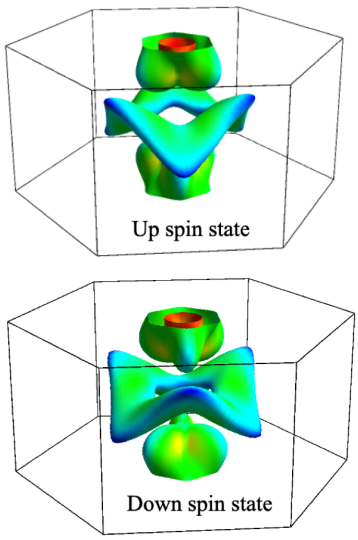

Figure 1: Iso-energy surfaces of the bandstructure at $E = E_F - 0.5$ eV for up-spin and down-spin states in altermagnetic MnTe.

References

[1] Thi Phuong Thao Nguyen and Kunihiko Yamauchi, Phys. Rev. B **107**, 155126 (2023).

[2] T. Osumi, S. Souma, T. Aoyama, K. Yamauchi, A. Honma, K. Nakayama, T. Takahashi, K. Ohgushi, and T. Sato, Phys. Rev. B **109**, 115102 (2024).

[3] Kunihiko Yamauchi and Ikutaro Hamada, Phys. Rev. B **108**, 045108 (2023).

[4] Thi Phuong Thao Nguyen and Kunihiko Yamauchi, J. Phys. Soc. Jpn. **93**, 034710 (2024).

Quantum transport theory based on large-scale first-principles electron transport calculations

NOBUHIKO KOBAYASHI
Department of Applied Physics, University of Tsukuba
1-1-1 Tennodai Tsukuba Ibaraki 305-8573

Quantum transport theory based on large-scale first-principles electron transport calculations is important from the viewpoint of materials science and technology. We have developed the nonequilibrium Green's function (NEGF) method and the O(N) time dependent wave-packet diffusion (TD-WPD) method on the basis of the density functional theory (DFT). By using these methods, we have investigated quantum transport properties of materials.

We have developed a Simulation code for Atomistic Kohn-sham Equation (SAKE) for the ab-initio electron transport calculation based on the DFT and NEGF formalism. [1] We have applied the method to analysis of electron transport in crystalline thin film of organic semiconductors. We reveal transport properties reflected by band dispersion and current characteristics due to good contact with organized electrode interface.

We developed the O(N) TD-WPD method for the quantum transport calculation of huge systems of up to 100 million atoms a decade ago, and have been applied organic semiconductors. [2] It is possible to calculate the conductivity and the mobility of the system with micron-order lengths at room temperature at the atomistic levels, and also to analyze the transport properties of materials weakly bonded by van der Waals interactions. The electron and hole mobilities of the pentacene thin-film are calculated taking the effect of intramolecular vibrations on both the partially dressed polaron and the dynamic disorder into consideration by using TD-WPD method. It is demonstrate that electron mobility in high-mobility organic semiconductors is indeed limited by polaron formation. [3]

We have also succeeded in O(N) thermoelectric transport calculation such as Seebeck coefficient and power factor. Different from a conventional method using the electric conductivity spectrum, it obtains the coefficients directly from the correlation function between heat and electric current based on linear response theory. We apply the methodology to a two-dimensional system and confirm that the calculated results are consistent with those obtained by the conventional method. The proposed methodology provides an effective approach to evaluate the thermoelectric performance of micron-scale materials based on quantum mechanics from an atomistic viewpoint. [4]

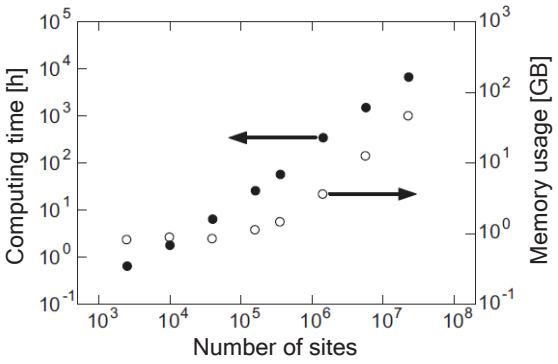

Figure 1: O(N) thermoelectric transport calculation using TD-WPD method.

References

[1] H.Takaki, N.Kobayashi, K.Hirose, *J. Phys.: Condens. Matter.* 32 325901(2020)

[2] H. Ishii, S. Obata, N. Niitsu, S. Watanabe, H. Goto, K. Hirose, N. Kobayashi, T. Okamoto, and J. Takeya, *Sci. Rep.* 10, 2524 (2020)

[3] H. Sato, S. A. Abd. Rahman, Y. Yamada, H. Ishii and H. Yoshida *Nat. Mater.* 21, 910 (2022).

[4] H. Ishii, N. Kobayashi, K. Hirose *J. Phys. Condens. Matter.* 36 (2024).

First-principles electron dynamics simulations for attosecond and nonlinear optical phenomena

Shunsuke SATO

Center for Computational Sciences

University of Tsukuba, Tsukuba, Ibaraki 305-8577, Japan

We have studied light-induced electron dynamics in solids using time-dependent density functional theory. This year, we developed a novel analysis technique for light-induced electron dynamics and nonlinear optical phenomena based on the microscopic current density, as reported in Ref. [1].

We further performed first-principles simulations on attosecond transient spectroscopy for bulk cobalt in order to investigate the transient optical properties of magnetic systems. Employing an intense femtosecond laser pulse as a pump pulse and an attosecond XUV pulse as a probe pulse, we computed the transient absorption spectra of bulk cobalt. As a result of the first-principles calculations, we observed a sharp reduction in photoabsorption around the absorption edge. We also analyzed the electron and spin density dynamics and found that the majority-spin electrons are ejected from the region close to cobalt atoms by the laser excitation, while the minority-spin electrons accumulate around the atom region. Consequently, the local spin polarization on the cobalt atoms is reduced, leading to a decrease in the exchange splitting of the core states of cobalt. Furthermore, this reduction in exchange splitting causes a blue shift in the absorption edge, resulting in a sharp reduction in photoabsorption around the edge.

This finding indicates that light-induced ultrafast spin dynamics can be investigated via attosecond transient absorption spectroscopy by focusing on photoabsorption around the absorption edge. Furthermore, since it relies on the local spin polarization of the atoms with the absorption edge, an element-specific spin dynamics detection can be realized on the attosecond timescale. We have summarized the results and submitted a manuscript to a journal.

References

[1] Shunsuke A. Sato, “"Frequency-resolved Microscopic Current Density Analysis of Linear and Nonlinear Optical Phenomena in Solids", J. Phys. Soc. Jpn. 92, 094401 (2023).

Exploring the mechanism of catalytic activity and degradation of electrodes

Minoru Otani

Center for Computational Sciences, University of Tsukuba, 1-1-1 Ten-nodai, Tsukuba, Ibaraki 305-8577, Japan

Improving energy conversion and storage technologies from renewable and sustainable sources is a significant issue in avoiding fossil fuel utilization. For this purpose, a physical understanding of electrochemical reactions at an electrode/solution interface plays a role in extracting the high electric power from low environmental impact energy sources.

Recently, a rhombohedral Boron mono-sulfide combined with a graphene nano-plate (r-BS+G) was experimentally found to be a promising material of an electrochemical catalyst for an oxygen evolution reaction (OER) in an alkaline medium [1]. We carry out the hybrid solution method based on the density functional theory and the classical solution theory (ESM-RISM) [2] to understand the catalytic mechanism at the interface between the r-BS(0001) surface and one molar KOH aqueous solution (1M-KOH(aq)). ESM-RISM enables us to control the electrode potential by varying the thermally averaged solvation structure. We apply ESM-RISM to the r-BS/1M-KOH(aq) with various surface defects because the previous experiment suggested the defect at the basal surface plays a role in the catalytic center of r-BS+G [1].

By the analysis of the change in the Gibbs free energy for the four-step OER intermediates, we found that the boron vacancy at the subsurface (V_{B2}) is considered one of the possible catalytic centers because of the low free energy barrier and stable surface structure for the OER intermediates. To understand the role of the electronic structure of V_{B2}, we applied bias voltage with the equilibrium potential of OER in the alkaline solution to the interface. The positive excess surface charge is induced at the r-BS electrode with V_{B2}, and it can attract the OH- ion, which triggers OER in alkaline media. Thus, V_{B2} has a favorable electronic structure for the OER catalyst [3].

References

[1] L. Li, S. Hagiwara, C. Jiang, H. Kusaka, N. Watanabe, T. Fujita, F. Kuroda, A. Yamamoto, M. Miyakawa, T. Taniguchi, H. Hosono, M. Otani, T. Kondo, Chem. Eng. J. **471**, 144489 (2023).

[2] S. Hagiwara, S. Nishihara, F. Kuroda, and M. Otani, Phys. Rev. Materials **6**, 093802 (2022).

[3] S. Hagiwara, F. Kuroda, T. Kondo, and M. Otani, ACS Appl. Mater. Interfaces, **43**, 50174 (2023).

First-principles calculations of exchange coupling constants dependent on magnetic short-range order

Tomonori TANAKA
Department of Materials Science and Engineering, Tokyo Institute of Technology
Nagatsuta-cho, Yokohama 226-8502

Exchange coupling constants (J_{ij}) in the classical Heisenberg model are widely used to understand finite temperature magnetism including thermal equilibrium properties and magnetic moment dynamics. A commonly used method to calculate these parameters is the one based on the magnetic force theorem (MFT), which utilizes the expression of energy change due to infinitesimal rotations of magnetic moments [1]. The validity of this expression is, however, questionable when the angles between magnetic moments become larger. Moreover, extending the MFT to include magnetic short-range order, a major temperature effect, is quite difficult.

In this project, we present a calculation method for J_{ij} with higher accuracy and extendability. In contrast to the previous perturbative method, we directly calculated the energy change resulting from small tilts of magnetic moments by using non-collinear density functional theory (DFT) with a large supercell. Exchange coupling parameters can be evaluated by fitting the energy changes to the Heisenberg model. The DFT calculations were performed within the GGA-PBE functional using PAW method as implemented in VASP.

Figures 1 (a) and (b) show the calculated J_{ij} of bcc Fe and bcc Co, respectively. The results of our method agree well with those of MFT in bcc Fe. On the other hand, there is a large difference in the J_{ij} on the first nearest neighbor between our method and MFT in the case of bcc Co. We carried out the same calculations for fcc systems and obtained the same trend. The mechanism of the deviation from the results of MFT is under consideration. Our results, however, clearly demonstrate the importance of non-perturbative calculation of J_{ij} for quantitative finite-temperature magnetism. We will further develop this method for more magnetic parameters in wide magnetic models, such as the Dzyaloshinskii-Moriya interaction.

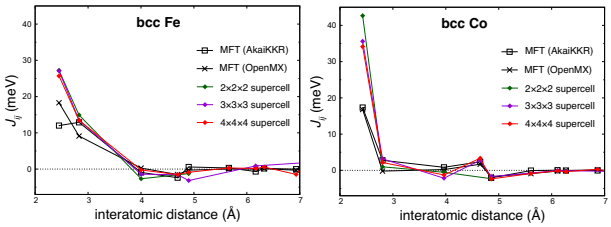

Figure 1: Exchange coupling constants as a function of interatomic distance of bcc Fe and bcc Co. Different supercells are used to check supercell-size dependence. Exchange coupling constants calculated by MFT using OpenMX[2] and AkaiKKR[3] are also shown for comparison.

References

[1] A. I. Liechtenstein *et al.*: J. Magn. Magn. Mater. **67**, 65-74 (1987).

[2] A. Terasawa *et al.*: J. Phys. Soc. Jpn. **88**, 114706 (2019).

[3] H. Akai: J. Phys.: Condens. Matter **1**, 8045 (1989).

Machine learning prediction of Lewis acidity of supported oxide single-atom catalysts

Kyoichi SAWABE
Graduate School of Engineering, Nagoya University, Chikusa, Nagoya 464-8603

Feature selection is crucial in constructing machine learning (ML) prediction models, but there is no definitive method. Eliminating multicollinearity is effective for feature selection, with the Variance Inflation Factor (VIF) serving as an indicator. However, in practical ML workflows, multiple VIFs often tend towards infinity, leading to arbitrariness in feature selection. To address this issue, we have developed the Feature selection by Random screening using VIF (FRV) method.

Figure 1 shows multiple linear regression (MR) models of the ionization energy (IE) of various transition metals as an example of this FRV method extracting high-quality features. In the case of (a), features were simply selected in order of strong correlation with IE and extracted by cross-validation. On the other hand, in the case of (b), features were extracted using the FRV method. By eliminating multicollinearity, the FRV method provides more accurate results.

Additionally, we adopt the FRV method for the ML prediction of CO adsorption energy on single-atom catalysts (SAC) using TiO_2 substrates. Slab units with n ($n = 2 - 6$) layers were used as models of TiO_2 surfaces. Three polymorphic structures of rutile, anatase, and brookite TiO_2 were used. To perturb the electronic structures of CO adsorption sites, a Ti atom with five coordinates on the TiO_2 surface was replaced with transition metals (Mn, Fe, Co, Ni, Ru, Rh, Pd, Re, Os, Ir, Pt). In this way, we have obtained the DFT energies of CO adsorption. The VASP program was used for spin polarization DFT calculations.

Figure 2a shows the results of Gradient Boosting Regression (GBR) prediction using features from the FRV method. The RMSE values for the training and test data are 0.033 and 0.151, respectively, showing good performance. However, there are outlier predictions in the test results. Therefore, to further improve the prediction, feature selection based on the chemical interactions (FC) was added. As a result, as shown in Figure 2b, the outlier elements are eliminated, and the test RMSE is improved to 0.126. This suggests that features suitable for ML models with good accuracy and generalization can be obtained by the FRV + FC method.

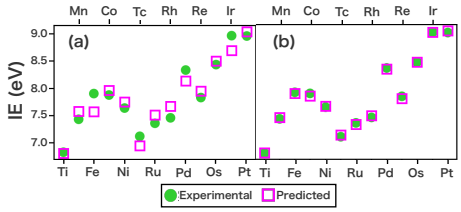

Figure 1: Experimental values versus predicted values of ionization energy (IE) for each metal by MR models. Refer to the text for the difference between (a) and (b).

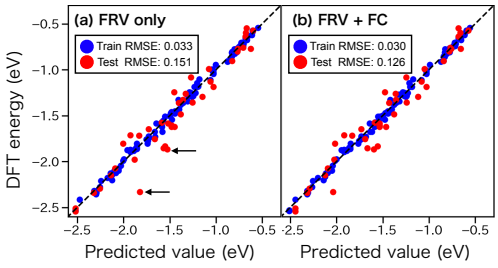

Figure 2: GRB prediciton of CO adsorption energy. The points indicated by the arrows are outlier data.

Ab-initio research on nano particles, and surfaces and grain boundaries of magnetic materials

Yasutomi TATETSU

Meio University, Biimata, Nago, Okinawa 905-8585

Recent advancements in chemical synthesis techniques have enabled precise control over nanoparticles, leading to the discovery of novel functional materials with unique properties. This targeted approach is particularly exciting for researchers seeking materials with both thermodynamic stability and instability, depending on the desired application. Teranishi's group at Kyoto University synthesized a new *Z*3-type Fe(Pd, In)$_3$ crystal structure by introducing indium as a third element into *L*1$_2$-FePd$_3$ [1].

In previous study, we conducted theoretical calculations for the *Z*3- and *L*1$_2$-type Fe–Pd–M systems where M represents Zn, Cd, Hg, Ga, In, Tl, Ge, Sn, and Pb. Conventional cells were chosen as 1 × 1 × 1 and √2×√2 × 1 for the *Z*3- and *L*1$_2$-type Fe–Pd–M systems, respectively, so the numbers of atoms in these unit cells can be the same for comparing the energy difference between these systems easily. When Cd, Hg, In, Tl, and Pb were introduced at the Pd site, we found that the Z3-type structure demonstrated higher stability than the *L*1$_2$-type structure. In contrast, the *Z*3-type structure was not stable when adding Zn, Ga, Ge, and Sn.

This year, we investigated the accuracy of neural network potentials [3] by comparing the formation energies calculated with OpenMX and Matlantis [4]. We conclude that the trends in the formation energies observed in these materials can be also seen in the results obtained using the Preferred Potential version 5.0.0 in Matlantis. However, there are inconsistencies in the formation energies calculated for materials containing heavy elements using these two methods. Further investigations will be needed by comparing some results calculated with VASP, as the Preferred Potential was referenced to a large number of calculations using VASP.

References

[1] K. Matsumoto *et al.*, Nat. Commun., **13**, 1047 (2022).

[2] S. Takamoto, et al., Nat Commun., 13, 2991 (2022).

[3] Matlantis (https://matlantis.com/), software as a service style material discovery tool.

GGA-SCAN failure for copper oxides and related superconductors

Noriyuki Egawa,[1] Soungmin Bae,[2] Hannes Raebiger[1]

1) Department of Physics, Yokohama National Universtiy, Yokohama

2) Institute of Materials Research, Tohoku University, Sendai

SCAN is a promising meta-GGA functional for strongly correlated systems [1], which has shown to open up band gaps for Mott insulators [2] and cuprate superconductors [3-5] without tunable parameters. However, SCAN has also shown to *overcorrect* the localization of carriers by opening band gaps where there should be none, predicting unphysical symmetry breakings and magnetizations [6]. Such localization errors can be corrected by $+U$ type corrections, and indeed, SCAN+U has been shown to improve oxidation enthalpies for various transition metal oxide systems, but copper oxides appear to exhibit some pathological failure [7-8]. We investigate the reliability of SCAN and SCAN+U for copper oxides and Yttrium-based cuprates, namely, $YBa_2Cu_3O_{7-\delta}$ (YBCO).

YBCO is a particularly interesting superconductor due to its high transition temperatures and the multivalence of copper. Copper in YBCO occupies two different lattice sites (Cu_{edge} and Cu_{plane} shown in Figure 1), and in $YBa_2Cu_3O_7$ (YBCO7) copper on ether site is in the Cu^+ state, whereas in $YBa_2Cu_3O_6$ (YBCO6) Cu_{edge} is in the Cu^{2+} state, and Cu_{plane}

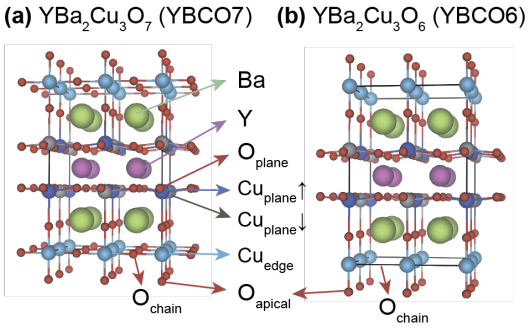

Figure 1. Lattice structures of (a) $YBa_2Cu_3O_6$ (YBCO6) and (b) $YBa_2Cu_3O_7$ (YBCO7). The arrows of Cu atoms indicate the local magnetic moments in antiferromagnetic configurations. Three oxygen sites O_{plane}, O_{chain}, O_{apcial} and two copper sites Cu_{plane} and Cu_{edge} in YBCO7 and YBCO6 are indicated.

is in the Cu^+ state. YBO6 can be formed by removing all of the oxygen in the so called *chain site* O_{chain}, but it has been recently observed that close to optimal doping, oxygen vacancies are formed not only at O_{chain} site, but also at the apical site O_{apical} [9]. We test the reliability of SCAN by investigating the formation of these different oxygen vacancies as well as the thermochemical stability of copper oxides CuO and Cu_2O.

We carry out density-functional calculations using the VASP package using PBE+U, SCAN, and SCAN+U functionals. For lattice parameters, all tested functionals show excellent agreement with experiment. We then

turn our attention to the thermochemical stability of CuO and Cu_2O by plotting their formation enthalpies in the chemical potential phase space ($\Delta\mu_O$, $\Delta\mu_{Cu}$) shown in Figure 2. $\Delta\mu_O$ and $\Delta\mu_{Cu}$ are defined by thermochemical stability conditions $\Delta H_f(CuO) = \Delta\mu_{Cu} + \Delta\mu_O$ and $\Delta H_f(Cu_2O) = \Delta\mu_{Cu} + 2\Delta\mu_O$, where $\Delta H_f(CuO)$ and $\Delta H_f(Cu_2O)$ are the formation enthalpies of the respective compounds. The zero values of $\Delta\mu_O$ and $\Delta\mu_{Cu}$ correspond to the formation of the elemental reference phase (O_2 gas and bulk copper), so the compounds are only stable in the negative quadrant of the ($\Delta\mu_O$, $\Delta\mu_{Cu}$) phase space. As seen in Figure 2, the relative stabilities of CuO and Cu_2O are well described by PBE+*U*, whereas SCAN and SCAN+*U* fail to stabilize Cu_2O at any value of the *U* parameter. This is caused by an overstabilization of $Cu^{2+}(d^9)$ against $Cu^{+}(d^{10})$ by SCAN, which becomes even worse in SCAN+*U*. We further find that this overstabilization is also translated to YBCO, where SCAN and SCAN+*U* excessively stabilize the oxygen vacancies in the apical site, associated with the oxidation of copper into $Cu^{2+}(d^9)$.

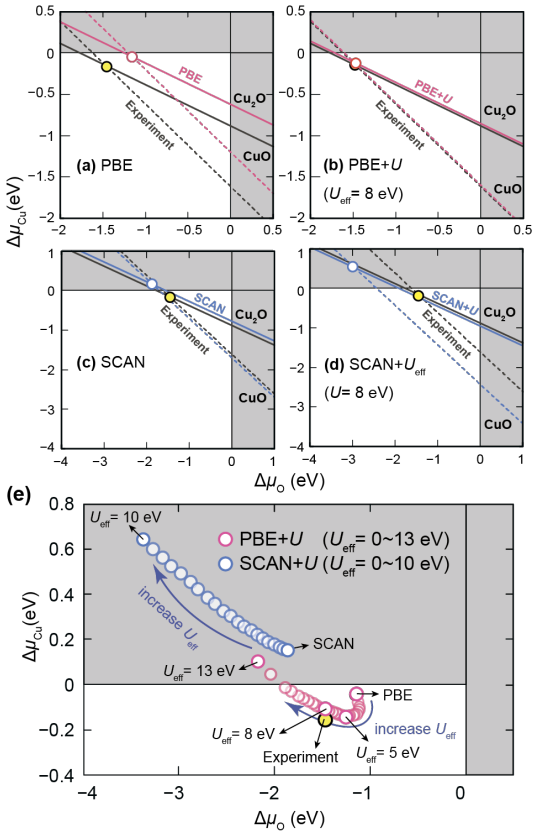

Figure 2. The phase stabilities with (a) PBE, (b) PBE+U (U_{eff} = 8 eV), (c) SCAN, and (d) SCAN+U (U_{eff} = 8 eV). The circles denote crossings where CuO and Cu_2O coexist. (e) The U_{eff} parameter dependence of the crossings predicted by PBE+U and SCAN+U functionals.

References

[1] J. Sun, A. Ruzsinszky and J. P. Perdew, *Phys. Rev. Lett.*, 2015, **115**, 036402.

[2] Y. Zhang et al., *Phys. Rev. B*, 2020, **102**, 045112.

[3] C. Lane et al., *Phys. Rev. B*, 2018, **98**, 125140.

[4] Y. Zhang et al., *Proc. Natl. Acad. Sci. U. S. A.*, 2020, **117**, 68-72.

[5] K. Pokharel et al., *npj Comput. Mater.* , 2022, **8**.

[6] Y. Zhang, W. Zhang and D. J. Singh, *Phys. Chem. Chem. Phys.*, 2020, **22**, 19585-19591.

[7] G. S. Gautam and E. A. Carter, *Phys. Rev. Mater.*, 2018, **2**, 095401.

[8] O. Y. Long, G. S. Gautam and E. A. Carter, *Phys. Rev. Mater.*, 2020, **4**, 045401.

[9] S. T. Hartman et al., *Phys. Rev. Mater.*, 2019, **3**, 114806.

Microscopic structure of water/CeO_2 interface

Akira NAKAYAMA

Department of Chemical System Engineering,

The University of Tokyo, Tokyo 113-8656, JAPAN

The structural properties, dynamical behaviors, and ion transport phenomena at the interface between water and cerium oxide are investigated by reactive molecular dynamics (MD) simulations employing neural network potentials (NNPs). The NNPs are trained to reproduce the density functional theory (DFT) results, and DFT-based MD (DFT-MD) simulations with enhanced sampling techniques and refinement schemes are employed to efficiently and systematically acquire training data that include diverse hydrogen-bonding configurations caused by proton hopping events. The water interfaces with two low-index surfaces of (111) and (110) are explored with these NNPs, and the structure and long-range proton and hydroxide ion transfer dynamics are examined with unprecedented system sizes and long simulation times. Various types of proton hopping events at the interface are categorized and analyzed in detail. Furthermore, in order to decipher the proton and hydroxide ion transport phenomena along the surface, a counting analysis based on the semi-Markov process is formulated and applied to the MD trajectories to obtain reaction rates by considering the transport as stochastic jump processes. Through this model, the coupling between hopping events, vibrational motions, and hydrogen bond networks at the interface are quantitatively examined, and the high activity and ion transport phenomena at the water/CeO_2 interface are unequivocally revealed in the nanosecond regime.[1]

In this work, the CP2K program package[2] was used for DFT-MD simulations, and the PLUMED program[3] was employed to perform the enhanced sampling simulations. The DeePMD-kit was used to construct NNPs.

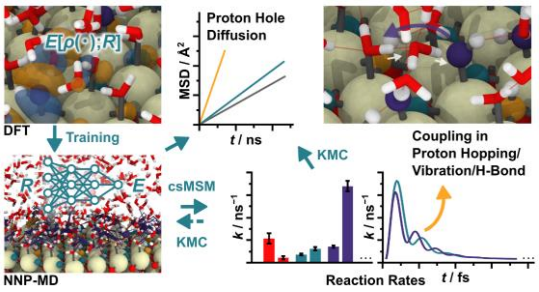

References

[1] T. Kobayashi, T. Ikeda, and A. Nakayama, Chem. Sci. **15**, 6816 (2024).

[2] T.D. Kühne, et al., J. Chem. Phys. **152**, 194103 (2020).

[3] G.A. Tribello, et al., Phys. Commun. **185**, 604 (2014).

Search for high temperature superconductivity in hydrides

Takahiro ISHIKAWA
Department of Physics, The University of Tokyo
7-3-1 Hongo, Bunkyo-ku, Tokyo 113-0033

Lanthanum hydride (La-H) shows superconductivity at 260 K at 170 GPa [1, 2]. Recently, it was reported that the superconducting critical temperature T_c was further increased to 550 K by repeatedly cooling and heating the sample [3]. The large enhancement of the superconductivity has been speculated to be caused by the reaction of La-H with contaminants in the sample chamber of the diamond anvil cell. Dominant candidates for the contaminants are nitrogen (N) and boron (B), which originate from ammonia borane, NH_3BH_3, used as a hydrogen-source material for the synthesis of La-H.

In this study, assuming that La-H reacted with N, we searched for stable and metastable phases in the La-N-H system at 20 GPa using an evolutionary construction scheme of a formation-energy convex hull [4]. At each generation, first, we quickly optimized a few thousand structures created by the scheme using universal neural network potentials on Matlantis [5], and extracted only a few ten structures showing that the enthalpy difference to the hull is less than 4.4 mRy/atom. Next, for the extracted structures, we performed structural optimization based on the density functional theory with the Quantum ESPRESSO (QE) code [6] using the ISSP supercomputer and updated the convex hull. We repeated this process up to the 20th generation. For the stable compounds, we calculated the electron-phonon coupling constant λ and the logarithmic averaged phonon frequency $\omega_{\log}$ with the QE code using the ISSP supercomputer and evaluated T_c from the Allen-Dynes formula [7]. As the results of the exploration, we found that La_2NH_2 shows the highest T_c value of 14.4 K at 20 GPa [8, 9], whereas further exploration is required to obtain concrete evidence of the high-T_c superconductivity at 550 K reported earlier.

References

[1] M. Somayazulu *et al.*: Phys. Rev. Lett. **122**, 027001 (2019).

[2] A. P. Drozdov *et al.*: Nature **569**, 528 (2019).

[3] A. D. Grockowiak *et al.*: Front. Electron. Mater. **2**, 837651 (2022).

[4] T. Ishikawa and T. Miyake: Phys. Rev. B **101**, 214106 (2020).

[5] Matlantis (https://matlantis.com/), software as a service style material discovery tool.

[6] P. Giannozzi *et al.*: J. Phys.: Condens. Matter **21**, 395502 (2009).

[7] P. B. Allen and R. C. Dynes: Phys. Rev. B **12**, 905 (1975).

[8] T. Ishikawa and S. Tsuneyuki: Proceeding of of CCP2023 (Accepted).

[9] T. Ishikawa *et al.*: Phys. Rev. B **109**, 094106 (2024).

Stable Structure Exploration of $K_2NdNb_5O_{15}$ and Phase Transition Mechanism Analysis Based on First-Principles Calculations

Hodaka ABE, Sou YASUHARA

School of Materials and Chemical Technology,

Tokyo Institute of Technology, Ookayama, Meguroku, Tokyo 152-8550

Antiferroelectric (AFE) materials have attracted considerable attention for applications in energy-storage dielectric capacitors. While numerous studies have reported perovskite-type AFEs with high energy storage properties, there have been very few reports on non-perovskite-type AFEs so far. To expand exploration range of AFEs, it is important to understand the mechanism of antiferroelectricity in non-perovskite compounds. Herein, we focused on $K_2NdNb_5O_{15}$ with a tungsten bronze (TB)-type structure. While our experimental study has reported AFE properties of Ta-substituted $K_2NdNb_5O_{15}$ at room temperature [1], the origin of the antiferroelectricity is still unclear. In this study, we investigated the mechanism of AFE phase transition in $K_2NdNb_5O_{15}$ using first-principles phonon calculations.

To deduce phase transition pathway from the high-symmetry structure, we calculated phonon dispersion curves of the $K_2NdNb_5O_{15}$ with the aristotype *P*4/*mbm* structure. First-principles phonon calculations were carried out using VASP and ALAMODE. Phonon dispersions of $K_2NdNb_5O_{15}$ at finite temperature were calculated based on self-consistent phonon (SCP) theory [2].

Figure 1 shows calculated phonon dispersion curves of $K_2NdNb_5O_{15}$ with the *P*4/*mbm* structure. We found that the phase transition behavior can be understood more clearly by focusing on a temperature dependence of phonon frequency obtained by SCP calculations rather than analyzing imaginary frequency modes calculated under the harmonic approximation. By comparing the temperature dependence of phonon frequencies, the most significant softening behavior is observed for the lowest frequency mode at the Z(0, 0, 1/2) point. The soft mode at the Z point is related to NbO_6 octahedral tilting, indicating that the high-symmetry structure can be stabilized by tilt displacement of NbO_6 octahedra.

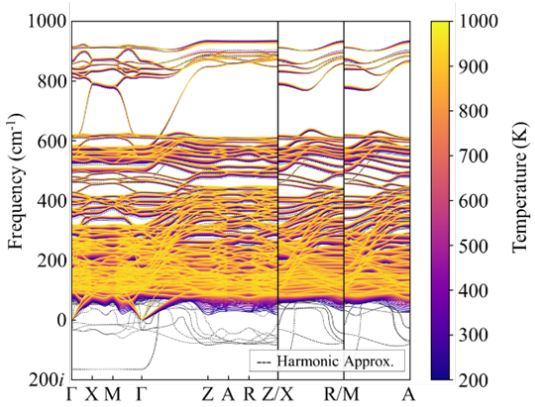

Fig. 1 Phonon dispersion curves of $K_2NdNb_5O_{15}$ with the aristotype *P*4/*mbm* structure calculated using harmonic approximation (dashed lines) and SCP theory (solid lines).

References

[1] H. Abe, S. Yasuhara, T. Tsurumi and T. Hoshina: J. Ceram. Soc. Jpn. **131**[7], 189(2023).
[2] T. Tadano and S. Tsuneyuki: Phys. Rev. B, **92**, 054301 (2015).

Investigation on a mechanism of ferroelectricity in a wurtzite-type $LiGaO_2$

Sou YASUHARA

School of Materials and Chemical Technology,

Tokyo Institute of Technology, Ookayama, Meguroku, Tokyo 152-8550

Since a discovery of ferroelectricity in a wurtzite-type structure of Sc doped AlN in 2019[1], the structure haves gathered much attention. Exploring new material is necessary for understanding the polarization switching mechanism, therefore, we have started to investigate new wurtzite-type ferroelectric materials. We now focus on $LiGaO_2$ with a distorted wurtzite-type structure, which distortion is originated from the difference of ionic radii between Li^+ and Ga^{3+}. In this study, we carried out first principles calculations for evaluating a polarization switching in $LiGaO_2$.

The density functional theory calculations were carried out using the projector augmented wave method as implemented in the VASP. The modified Predew-Burke-Ernzerhof generalized gradient approximation was utilized as an exchange correlation functional. The k-point mesh was 8×8×8. The cutoff energy and convergence energy were 550 eV and 1.0×10^{-7} eV, respectively. The barrier height energy of a polarization switching was evaluated by performing a nudged elastic band (NEB) method.

The calculation result of NEB in non-doped $LiGaO_2$ is shown in Fig. 1, in which the calculated results of AlN and ZnO are also shown (the energy was standardized by the total number of atoms). The barrier heigh energy (E_b) of polarization switching in AlN and ZnO are 0.257 eV and 0.135 eV, respectively. That in $LiGaO_2$ is 0.182 eV, indicating that the material is more favor to the polarization switching than that in AlN. We have revealed effectiveness of chemical doping to reduce the E_b value in $LiGaO_2$ as same as that in AlN or ZnO. Further investigations are kept going to understand the new ferroelectric material of $LiGaO_2$.

References

[1] S. Fichtner, N. Wolff, F. Lofink, L. Kienle, and B. Wagner, J. Appl. Phys. **125**, 114103 (2019).

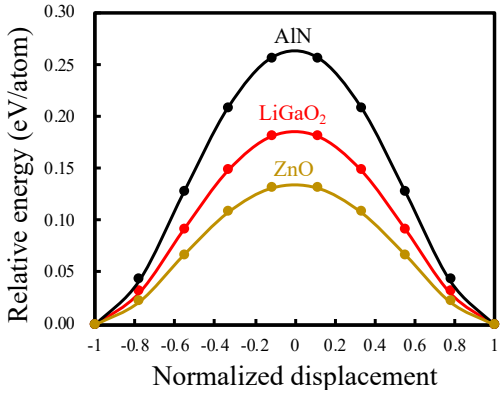

Fig. 1 The calculation results of NEB.

First-principles calculations for molecular junction

Tatsuhiko OHTO

Graduate School of Engineering,

Nagoya University, Furo-cho, Chikusa-ku, Nagoya, Aichi 464-8603

Enhancing hydrogen production is key to achieving a carbon–neutral world. Among the various technologies available, using renewable energy for water electrolysis stands out as a leading method for creating green hydrogen. Because fresh water only represents a minuscule 0.01 % of our planet's water reserves, seawater electrolysis is a potential solution to resolve this limitation and attain sustainable hydrogen production. Nevertheless, electrolysis of seawater in its neutral state demands stringent reaction conditions, making it imperative to thoughtfully design the electrodes, particularly the anodes. This study presents the development of highly durable, noble-metal-free, high-entropy alloy anodes suitable for neutral seawater under highly fluctuating power operation. Using high-throughput DFT calculations, we assessed the Gibbs free energy of the oxygen evolution reaction (OER) intermediates (H*, OH*, O*, and OOH*) and adsorption energy of a chlorine intermediate (Cl*) under an applied potential of 1.23 V on a 9 elements high entropy alloy (9eHEA). DFT calculations reveal that the oxidized surface (passivation layer) of the anode prevents Cl− adsorption, helping to protect the catalytically active sites and prevent catalyst degradation.

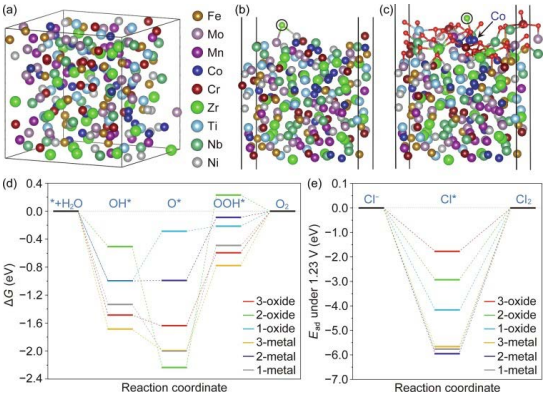

Fig. 1: (a) Model of 9eHEA without oxidation. Models of 9eHEA (b) without oxidation and (c) with oxidation with a chlorine intermediate on structure 3. Black circles indicate Cl intermediates on catalytically active sites. Red spheres represent O atoms. An arrow presents an initial adsorption side of Cl on Co. (d) Gibbs free energy profiles for the OER with oxidation under an applied potential of 1.23 V. (e) Adsorption energies of the chlorine intermediate under an offset of 1.23 eV with and without oxidation.

References

[1] F. Shiokawa et al. Chem. Eng. J. **479**, 147862 (2024).

Theoretical analysis of anion intercalation process into cathode conductive carbon

Atsuo YAMADA

Department of Chemical System Engineering,

The University of Tokyo, Bunkyo-ku, Hongo, Tokyo 113-8656

5 V-class cathode materials for high-voltage Li-ion batteries have been developed, but long-term stable operation has not been achieved. The reduced cycle stability is mainly attributed to the unintended anion intercalation into a cathode conductive carbon [1]. Herein, we theoretically investigated the insertion process of PF_6^- anion into the graphite layer in EC-based electrolyte.

The ESM-RISM method was adopted to evaluate the activation energy for the anion insertion into the graphite. The simulation cell is composed of graphite electrode ($C_{252}(PF_6)_9H_{36}$) and the 1 M $LiPF_6$/EC electrolyte. The activation energy was obtained by computing the grand potential (Ω) at each point while moving a PF_6^- anion from the electrolyte side (r = 20 Å) to the electrode interior (r = 0 Å). All the calculations were conducted with Quantum Espresso code.

The Ω profile of PF_6^- anion insertion into the graphite is shown in Fig.1. The activation energy was estimated to be 0.37 eV at the equilibrium potential, considerably smaller than that of Li^+ (0.6 eV) [2]. Notably, Ω increased as N_{EC} decreased from r = 10 Å, suggesting a significant contribution of PF_6^- desolvation process to the activation barrier. Therefore, the further exploration of solvent species that increase the desolvation energy of the anion is crucial to suppress the anion insertion into the cathode conductive carbon.

References

[1] S. Ko, Y. Yamada, A. Yamada, *Joule*, **5**, 998 (2021).

[2] J. Haruyama, T. Ileshoji, M. Otani, *J. Phys. Chem. C*, **122**, 9804 (2018).

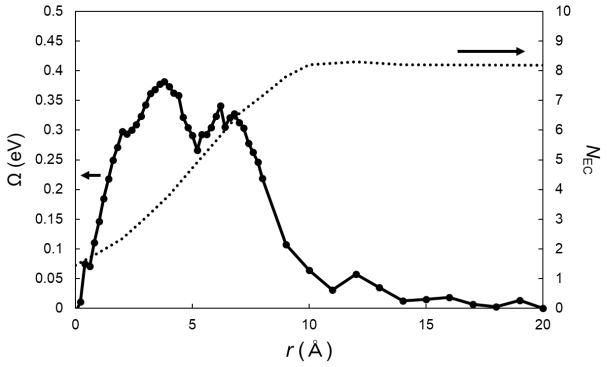

Figure 1 The variation of the ground potential (Ω, left axis) and solvent coordination number around the anion (N_{EC}, right axis) along the insertion process of the PF_6^- anion into the graphite in 1 M $LiPF_6$/EC electrolyte.

Extension of finite temperature calculation with random-phase sates to general variational wave functions

Toshiaki IITAKA

Center for Computational Science,

RIKEN, 2-1 Hirosawa, Wako, Saitama, 351-0198 JAPAN

Calculation of thermal average of an observable A of a closed quantum many-body system in its thermal equilibrium at an inverse temperature is one of the most important problems in computational physics. It has, however, two major computational difficulties. The number of quantum states to be included and the dimension of each quantum state vector are both exponentially increases as the temperature and the system size increases, respectively. Each difficulty has been independently attacked using *random state method* [1, 2] and *variational wave function*, respectively.

Thermal average of observable A at inverse temperature β is calculated using *random state* $|\Phi\rangle$ as

$$\langle A\rangle = \frac{tr[e^{-\beta H}A]}{Z} = \frac{\langle\langle\langle\Phi|A|\Phi\rangle\rangle\rangle}{Z}$$

where

$$Z(\beta) = tr[e^{-\beta H}] = \langle\langle\langle\Phi|\Phi\rangle\rangle\rangle$$

is the *partition function* and the double bracket indicates statistical average over random states. The *thermal state* is defined by the imaginary time evolution of the random state.

$$|\Phi(\beta)\rangle = e^{-\beta H/2}|\Phi\rangle$$

Thermal energy E and specific heat C are expressed as

$$E(\beta) = \langle H\rangle$$

and

$$C(\beta) = k_B\beta^2\left[\langle E^2\rangle - \langle E\rangle^2\right].$$

Variational wave function is a point on a manifold embedded in the Hilbert space,

$$|\psi(w)\rangle = \sum_{\boldsymbol{\sigma}} c(w,\boldsymbol{\sigma})|\boldsymbol{\sigma}\rangle$$

which is parameterized with variational parameters, $w = \{w_i\}$, whose number is much less than the dimension of the Hilbert space.

Thermal state has been introduced in some variational wave functions such as MPS and PEPS [3-7] as

$$\left|\Psi(\beta;w)\right\rangle = e^{-\beta H/2}\left|\Psi(w)\right\rangle$$

where $\left|\Psi(w)\right\rangle$ is a variational wavefunction with random parameters w.

In this project, the above formulation was extended to general form of variational wavefunctions for 2D spin lattice system whose coefficients $c(w,\boldsymbol{\sigma})$ are linear with respect to each parameter w such as in String-Bond States and Entangled Plaquette States [8]. The imaginary time evolution was calculated with stochastic reconfiguration[3, 9]. The program is written with NetKet [10] library and parallelized with respect to initial random states, Markov chains, and plaquettes.

References

[1] T. Iitaka, and T. Ebisuzaki, Phys. Rev. Lett. **90**, 047203 (2003).

[2] T. Iitaka, and T. Ebisuzaki, Phys. Rev. E **69**, 057701 (2004).

[3] K. Takai *et al.*, J Phys Soc Jpn **85**, 034601 (2016).

[4] S. Garnerone, T. R. de Oliveira, and P. Zanardi, Phys. Rev. A **81**, 032336 (2010).

[5] T. Iitaka, arXiv:2006.14459 (2020).

[6] A. Iwaki, A. Shimizu, and C. Hotta, Phys. Rev. Res. **3**, L022015 (2021).

[7] S. Goto, R. Kaneko, and I. Danshita, Phys. Rev. B **104**, 045133 (2021).

[8] I. Glasser *et al.*, Physical Review X **8**, 011006 (2018).

[9] S. Sorella, Phys. Rev. Lett. **80**, 4558 (1998).

[10] G. Carleo *et al.*, SoftwareX **10**, 100311 (2019).

Analysis of phonon-assisted ionic transport in solid electrolytes

Susumu FUJII
Division of Materials and Manufacturing Science, Osaka University
Yamadaoka, Suita, Osaka, 565-0871
Nanostructures Research Laboratory, Japan Fine Ceramics Center
Mutsuno, Atsuta, Nagoya 456-8587

Exploration for solid electrolytes that exhibit high ionic conductivity at room temperature is one of the important issues in the development of all-solid-state batteries. The relationship between phonons and ionic conduction has been investigated extensively, to design fast ionic conductors based on the insights from lattice dynamics [1].

Recently, fast alkali-ion conduction has been reported in the series of antiperovskite compounds M_3XCh, where M is Li or Na, X is H or F, and Ch is S, Se, or Te [2, 3]. Interestingly, the frequency of a specific phonon mode in the antiperovskites, which corresponds to the rotation of an XM_6 octahedron (Fig. 1), has a linear correlation with the migration energy barrier of alkali ions via vacancy and interstitial sites. The softness of a specific phonon mode that enhances ionic conduction may guide the development of fast ionic conductors. However, the influence of anharmonicity at finite temperature and the existance of point defects on the rotational phonon mode is still unclear, inhibiting the understanding of underlying mechanisms behind ionic conduction.

In this study, to reveal the relationship between phonons and ionic conduction in M_3XCh antiperovskites, anharmonic effects on the frequency of the rotational phonon mode has been investigated by self-consistent phonon (SCPH) theory implemented in ALAMODE code [4]. In addition, the influence of M ion vacancy has been calculated by band unfolding method implemented in Phonopy code [5] (Fig. 1). The computational resources were almost spent on the first principles molecular dynamics simulations, which were to obtain the atomic displacements and forces for estimating fourth-order force constants necessary in the SCPH calculations.

The calculations based on the SCPH theory showed the increase in frequency (hardening) of the rotational phonon mode with increasing temperature. The magnitude of hardening depends on the compounds. The linear relationship between the frequency and migration energy barrier is more evident by considering the anharmonic effect at 300 K, excluding the compounds that contain large anions.

The band unfolding calculations for large supercells including an M ion vacancy also showed that the frequency of rotational phonon mode is not significantly varied by the vacancy. This behavior is still observed in the projected band dispersions for the M ions adjacent to the vacancy.

These results demonstrate that the frequency of the rotational phonon mode is the good indicator of fast ionic conduction in the series of antiperovskites, even considering anharmonic effects.

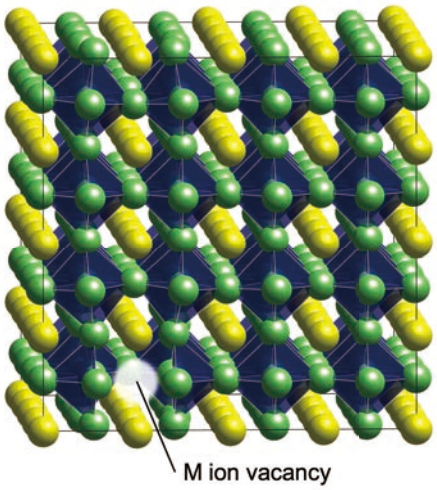

Figure 1: An example of vacancy models for the band unfolding calculations.

References

[1] S. Muy, R. Schlem, Y. Shao-Horn, and W. G. Zeier, Adv. Energy Mater. **11**, 2002787 (2021).

[2] S. Gao, T. Broux, S. Fujii, C. Tassel, H. Kageyama et al., Nat. Commun. **12**, 201 (2021).

[3] S. Fujii, S. Gao, A. Kuwabara, H. Kageyama et al., J. Am. Chem. Soc. **143**, 10668 (2021).

[4] T. Tadano, and S. Tsuneyuki, Phys. Rev. B **92**, 054301 (2015).

[5] A. Togo, L. Chaput, T. Tadano, I. Tanake, J. Phys. Condens. Matter **35**, 353001 (2023).

Analysis of mechanical properties of alloy materials using first-principles and molecular dynamics calculations

Naoki UEMURA

The Nagamori Institute of Actuators, Kyoto University of Advanced Science,

18, Yamanouchi-Gotandacho, Ukyo-word, Kyoto, 615-8577

The mechanical properties of structural materials, including strength, ductility, and toughness, as well as hydrogen embrittlement, which are causes of degradation of structural materials, have been studied using DFT and MD simulations.

In the year, the slip properties of a magnesium alloy with crystal structures called Long-Period Stacking-Ordered (LPSO) were investigated. This alloy is reported to exhibit a yield strength of more than 600 MPa [1]. Experimental studies have indicated that the basal slip is predominant, while the prismatic slip occurs as a non-basal slip [2–4]. We evaluated the slip system of Mg–Zn–Y alloys with LPSO structures by creating slab models for the basal and prismatic planes and obtaining stacking fault (SF) energies by DFT calculations [5]. The DFT calculation code used was the package VASP, which is implemented in the ISSP supercomputers.

Here we report the SF energies of the prismatic planes for two models with different initial crystal structures of 10H LPSO structure in Mg–Zn–Y alloys (Fig. 1). The difference between the two initial structures is that one of the two solute clusters in the unit cell is shifted relative to the other by (1/2, 1/2) in the ab plane. We found no difference in the SF energies of the prismatic slip of these two crystal structures. This result is consistent with previous studies showing that the long-range interactions of solute clusters are very small [6].

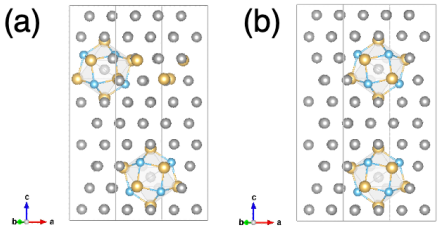

Fig. 1: Crystal structures of 10H LPSO in Mg–Zn–Y alloys. The gray, blue, and yellow spheres are magnesium, zinc, and yttrium, respectively.

References

[1] Y. Kawamura *et al*., Mater. Trans. **42** (2001) 1172–1176.

[2] K. Hagihara *et al*., Mater. Trans. **52** (2011) 1096–1103.

[3] K. Hagihara *et al*., Mater. Trans. **54** (2013) 693–697.

[4] K. Hagihara *et al*, Acta Mater. **109** (2016) 90–102.

[5] N. Uemura, S. Singhaneka, and R. Matsumoto, submitted.

[6] T. Murakami *et al*., Comput. Mater. Sci. **153** (2018) 297–302 .

Two-dimensional structures for non-layered materials

Shota ONO
Institute for Materials Research, Tohoku University, Sendai 980-8677, Japan

Two-dimensional (2D) materials have been studied extensively due to their intriguing properties and potential applications. 2D materials are usually exfoliated from layered materials that consist of atomically thin layers vertically stacked via van der Waals (vdW) forces. On the other hand, 2D materials created from non-layered materials have also been synthesized experimentally.

In this project, we have studied non-vdW 2D materials using Quantum ESPRESSO package. First, we investigated the structural properties of 2D strontium titanate ($SrTiO_3$) [see Fig. 1(a)] [1]. This is constructed by stacking SrO, TiO_2, and SrO monolayers, and the chemical formula is Sr_2TiO_4. We have shown that the TiO_6 octahedral rotations emerge with a rotation angle twice that in the 3D bulk. The rotation angle decreases when the film thickness is increased. Using the molecular dynamics (MD) simulation, we have demonstrated that the cubic-like phase appears above 1000 K [see Fig. 1(b) and 1(c)]. Such a phase transition temperature is higher than of 3D bulk. The effect of octahedral rotations on the electronic properties is also discussed.

We have also explored fluorite-type (CaF_2-type) materials in the 2D limit [2]. The crystal structures of fluorite-type materials are extracted by using Materials Project database and pymatgen code. More than 30 monolayers truncated from the surface have negative formation energy and they are dynamically stable. In addition, several monolayers are identified to exhibit negative Poisson's ratio. The present work has provided novel non-vdW materials in the 2D limit.

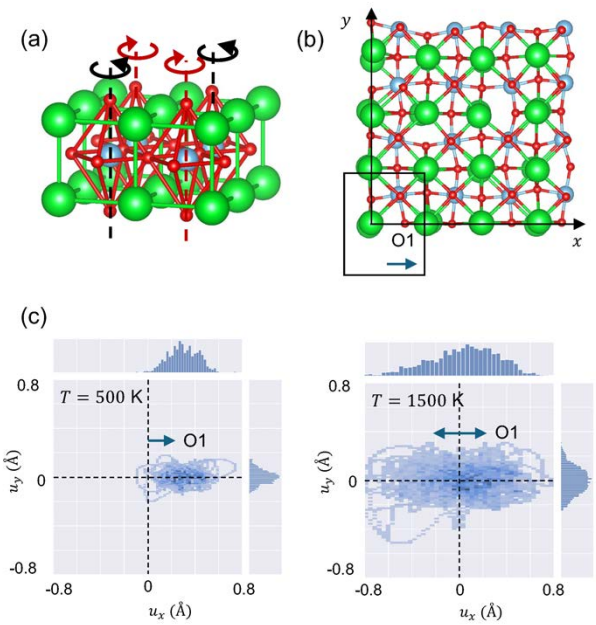

Figure 1: (a) 2D $SrTiO_3$ monolayer. The TiO_6 octahedra are elongated along the out-of-plane direction and rotate around the z axis. (b) Atomic distribution of 2D $SrTiO_3$ monolayer after a MD simulation of 5 ps for 500 K. The O1 atom shifts in the x direction. (c) The displacement distribution of O1 atom within the x-y plane at 500 K (left) and 1500 K (right).

References

[1] S. Ono and Y. Kumagai: J. Phys. Soc. Jpn. **92**, 114601 (2023).

[2] S. Ono and R. Pawar: *in preparation.*

Surface Bain distortion

Shota ONO
Institute for Materials Research, Tohoku University, Sendai 980-8677, Japan

This project is motivated by the recent experiment of bending silver (Ag) nanowires [1]: the structural transformations from fcc to bcc to hcp to fcc structures are observed by bending the Ag nanowire. The fcc-bcc transformation has been explained by tetragonal Bain distortion [see Fig. 1(a)]. However, bcc Ag has been observed only near the surface [1]. In addition, bcc-structured fcc metals are known to be unstable at ambient condition. Therefore, the realization of bcc Ag is questionable.

In this project, we study the effect of surface on the Bain distortion. The DFT calculations are performed by using Quantum ESPRESSO, and the slab models are constructed by using Atomic Simulation Environment (ASE). Through the surface Bain distortion, fcc is transformed into "body-centered tetragonal (bct) structure", followed by a reoriented fcc structure [see Fig. 1(b)]. The bct phase is thermodynamically stable only when a fixed boundary condition is imposed, implying that such a metastable phase must be surrounded by fcc ground state [see Fig. 1(c)]. The present work has extended the Bain distortion concept to apply the surface systems and indicated that the surface could play an important role in phase transitions [2].

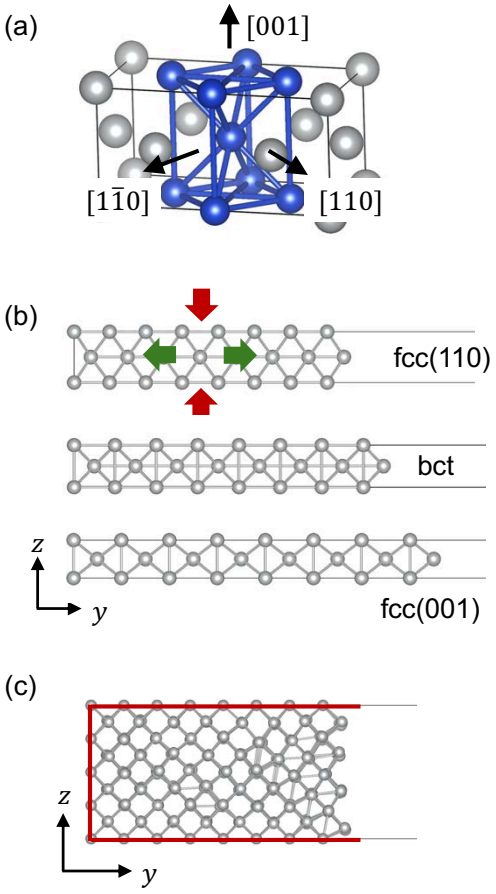

Figure 1: (a) Tetragonal unit cell in the fcc structure. A compression along the z-axis induces a transformation from fcc ($c/a = \sqrt{2}$) to bcc ($c/a = 1$) structure. (b) The surface Bain distortion of the Ag nanowire. The bct phase appears due to the free-boundary condition along the y-axis. (c) Atomic distribution of Ag nanowire in the bct phase after a molecular-dynamics simulation of 1.5 ps. Atoms on the boundary (red) are fixed during the simulation. Without the boundary condition, the bct phase is unstable [2].

References

[1] S. Sun *et al.*,: Phys. Rev. Lett. **128**, 015701 (2022).

[2] S. Ono and K. Tamura: Comp. Mater. Sci. **237**, 112920 (2024).

Study on structural elementary excitations at semiconductor surfaces and interfaces

Hiroyuki KAGESHIMA
Graduate School of Natural Science and Technology, Shimane University
1060 Nishi-Kawatsucho, Matsue, Shimane 690-8504

In this project, we have been focused on physical properties of structural elementary excitations, such as point defects and precursors, of semiconductor surfaces and interfaces [1, 2, 3]. In this year, we have focused on the physical properties of SiO self-interstitial in SiO_2 [4] and of hBN island on Cu(111) [5]. The calculations were performed based on the first-principles calculation. Program package PHASE/0 was employed [6].

The oxidation of Si is a seemingly simple phenomenon in which Si reacts with O to form Si oxide. However, when one looks at this phenomenon on an atomic scale, an interesting and complex atomic transport phenomenon occurs. O diffuses and moves through the Si oxide film as if it were sewing through the gaps between the atomic bonds of Si and O while maintaining the shape of O_2 molecules. The O_2 decomposes at the interface and breaks into Si atoms to form Si oxide, which induces a large volume expansion and distortion at the interface. The reaction of this distortion causes the Si atoms to move around in the oxide film in a complex manner, resulting in structural deformation of the oxide film and release of the distortion.

The problem is the reaction of this distortion. Roughly speaking, the oxide film seems to be able to deform freely as if it were a gas in a high-temperature environment, but the oxidation temperature is about 700°C to 1000°C, much lower than the melting point of silicon oxide, 1710°C. Therefore, the oxide film should be considered as a solid, and the reaction of strain is thought to induce various defects and set them in motion. The most fundamental of these defects are point defects, and because O is scarce in the oxide film near the interface, O vacancies and interstitial Si are the key points. But considering that compressive stress is applied, interstitial Si is considered to be the most important.

We have been focusing our attention on this point. We have shown from the first-principles calculations that the transport process of interstitial Si in the near-interface oxide film can be constructed by assuming only three fundamental atomic processes (O vacancy transport, Si coordination number conversion, and ACBD bond order conversion). The metastable structures at that time and their energy landscapes are also identified by the first-principles calculations [3]. Finally, the transition structures and barrier heights for each fundamental atomic process are identified [4]. Furthermore, we succeeded in determining the details of the energy landscape of the entire transport process and the maximum barrier height. The values are consistent with the experiment. The climbing image-nudged elastic band method (CI-NEB method) was applied in this calculation.

The hBN growth process on Cu surfaces is also a seemingly simple phenomenon in which B and N precursors aggregate to form hBN islands. However, since this is a binary system of B and N, the shape of the hBN island

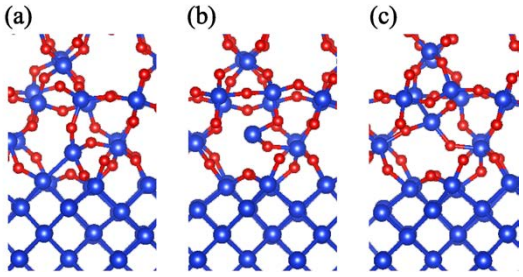

Figure 1: Fundamental processes of Si coordination number conversion. (a) 4-coordinated Si becomes (b) 2-coordinated Si and then returns to (c) 4-coordinated Si.

can change depending on the balance of the number of B and N atoms. The balance between the number of B and N atoms depends on the chemical potential. Therefore, we investigated the relationship between island size, island shape, and chemical potential by the first-principles calculations [5]. Two van der Waals force correction methods, vdwDF2-b86r and D3, were used in the study to confirm the quantitative nature of the relationship.

The basic framework of hBN islands on the Cu surface is the six-membered ring of BN. When the island size is small, only equilateral triangular islands can be formed in principle. However, as the island size increases, equilateral triangular islands are formed only when the chemical potential is extreme, otherwise ribbon-like square islands are formed. Ribbon-shaped islands have both B-only and N-only edges of equal length, which seems to be the origin of the stability of such shaped islands. In fact, the B and N at the edges interact strongly with the Cu substrate, and this interaction may be responsible for the shape of the islands.

These results are interesting when compared to the results for hBN islands that are not on the Cu surface and are completely freestanding. In freestanding islands, islands with B-only edges are unstable and do not form. Moreover, islands in which the six-membered ring is not the basic framework also become stable. In other words, when the interaction between the Cu substrate and the edge atoms of the island is eliminated, the stability and shape of the island become completely foreign.

The importance of the interaction between the edge atoms of the island and the Cu substrate becomes even clearer when looking at the cross-sectional shape of the island: for B-only edges, the distance from the Cu substrate becomes shorter due to the interaction, and the cross-section of the island becomes arched. On the other hand, the N-only edge does not have such a short distance from the Cu substrate, and thus the cross-section of the island is relatively flat. However, the distance to the Cu substrate does not necessarily indicate the strength of the interaction. In fact, when the energy of the edge is evaluated, the N-only edge is more stable than the B-only edge. In other words, the interaction with the Cu substrate is stronger for the N-only edge. This may be related to the fact that N prefers to be more negatively charged and B and Cu prefers to be more positively charged.

References

[1] H. Kageshima, Y. Yajima, K. Shiraishi, and T. Endoh, Jpn. J. Appl. Phys. **58** (2019) 111004 (11 pages).

[2] K. Yata and H. Kageshima, Jpn. J. Appl. Phys., **60** (2021) 035504 (6 pages).

[3] H. Kageshima, T. Akiyama, and K. Shiraishi, Matter. Sci. Semicon. Process. **162** (2023) 107527 (7 pages).

[4] H. Kageshima, T. Akiyama, and K. Shiraishi, Jpn. J. Appl. Phys., 63 (2024) 04SP08 (5 pages).

[5] R. Imamura and H. Kageshima, Jpn. J. Appl. Phys., 63 (2024) 04SP39 (11 pages).

[6] https://azuma.nims.go.jp

First-Principles Investigation of Energy-Conversion Processes in Biological and Material Systems

Takatoshi Fujita
National Institutes for Quantum Science and Technology
Anagawa, Inage-ku, Chiba 263-8555

We have developed a multi-scale computational methodology to investigate the exciton dynamics in complex molecular systems based on large-scale excited-state calculations [1] and open quantum system approaches. Recently, we have extended the method to calculating various time-resolved spectroscopic signals, including pump-probe and two-dimensional spectroscopy. Our multi-scale computational framework enables us to explore the relationship among the electronic structure, quantum dynamics of an exciton or a charge carrier, and the time-resolved spectroscopic signals in realistic material or biological systems. This year, we have applied our approaches to studying photo-energy conversion processes in the organic solar cell and the natural photosynthetic system.

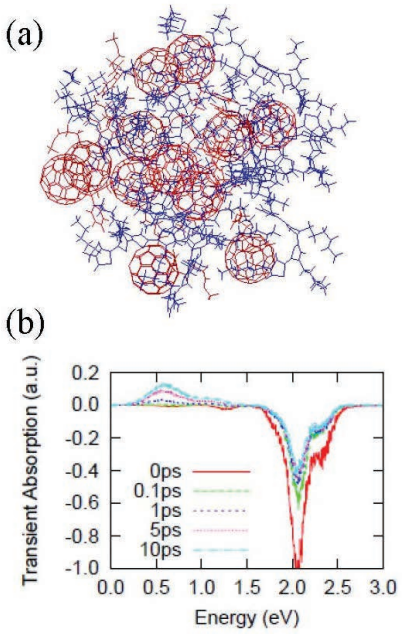

Figure 1: (a) The amorphous structure of P3HT(blue) and PCBM(red) prepared using molecular dynamics simulations. (b) The simulated transient absorption spectra, which show the negative signal at 2.1 eV of stimulated emission plus ground-state bleaching contributions and the positive signal of excited-state absorption at around 0.5–0.9 eV.

As an application [2], we have investigated the charge separation dynamics and pump-probe spectroscopy in the amorphous P3HT/PCBM blend (Fig.1(a)). The P3HT/PCBM blends have been widely studied as typical model systems as organic bulk heterojunction solar cells. To simulate quantum dynamics and time-resolved spectroscopy, the model Hamiltonian for single-excitation and double-excitation manifolds was derived on the basis of fragment-based excited-state calculations within the GW approximation and the Bethe-Salpeter equation. We explore the energetics of the electron-hole separation and the linear absorption spectrum. Then, we investigated the quantum dynamics of exciton and charge carriers; in addition, we compared it with the pump-probe transient absorption spectra (Fig.1(b)). In particular, we introduced the pump-probe excited-state absorption (ESA) anisotropy as a spectroscopic signature of charge carrier dynamics after exci-

ton dissociation. We found that the charge separation dynamics correlate well with the anisotropy dynamics of the pump-probe ESA spectra after charge-transfer excitation. The present study provides the fundamental information for understanding the experimental spectroscopy signals by elucidating the relationship between the excited states, the exciton and charge carrier dynamics, and the time-resolved spectroscopy.

As another application, we considered the charge-separation dynamics in the photosystem II-reaction center (PSII-RS) (Fig.2 (a)). Despite extensive experimental studies, the charge-separation pathway (Fig.2(b)) in the PSII-RC is still controversial. In this study, we have investigated the excited-state dynamics in the PSII-RC using fragment-based excited-state calculations, wavepacket propagation, and time-resolved spectroscopy. To improve the accuracy of the quantum dynamics method, we have applied the empirical thermal correction method, in such a way that the wavepacket propagation provides the correct thermal equilibrium state in the long-time limit. Based on the thermal-corrected wavepacket approaches, we have suggested that the ESA anisotropy dynamics can become a sensitive probe of the charge-separation pathways. The developed computational methods will also be applied to other light-harvesting systems in collaboration with the experimental group [3].

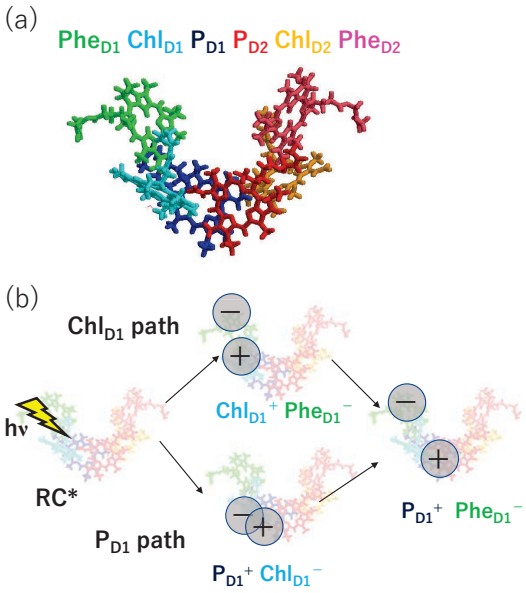

Figure 2: (a) The pigments complex in the PSII-RC (PDB ID: 3wu2), which consists of special-pair chlorophylls (P_{D1} and P_{D2}), accessory chlorophylls (Chl_{D1} and Chl_{D2}), and pheophetyns ($Pheo_{D1}$ and Phe_{D2}) (b) Two charge-separation pathways in the PSII-RC.

References

[1] T. Fujita, Y. Noguchi, J. Phys. Chem. A **125** (2021) 10580.

[2] T. Fujita, T. Hoshi, J. Phys. Chem. B **127** (2023) 7616.

[3] M. Tsubouchi, N. Ishii. Y. Kagotani, R. Shimizu, T. Fujita, M. Adachi, R. Itakura, Opt. Express **31** (2023) 6890.

Ab-initio simulation of electron energy distribution in an insulator excited by an intense laser pulse

Yasushi SHINOHARA[1,2]

[1]*Photon Science Center,*

The University of Tokyo, Hongo, Bunkyo-ku, Tokyo 113-8656.

[2]*NTT Basic Research Laboratories,*

NTT Corporation, 3-1 Morinosato Wakamiya, Atsugi, Kanagawa 243-0198.

We have investigated responses of insulators exposed to strong light fields via time-dependent density-functional theory (TDDFT) [1]. When the field strength of light is comparable to the material's internal strength, the material exhibits extremely nonlinear responses that cannot be described by perturbative series. The only viable option to describe these responses is a direct solution of the time-dependent Kohn-Sham equation in real-time. The SALMON-TDDFT code [2] provides opportunities for solving the Kohn-Sham equation for crystalline solids, molecules, and atoms. We used system B at SCC-ISSP.

To simulate subsequent phenomena after the strong field excitation, we need to consider multi-physical nature of spatiotemporal evolution beyond electron quantum degree of freedom such as thermalization over whole subsystems, energy/momentum flows in microscopic spatial range, phase transition and so on. We propose an electron energy distribution after excitation to bridge from TDDFT to a more macroscopic theoretical framework. The electron distribution is obtained by projecting the time-dependent orbitals $\psi_{c\boldsymbol{k}}(t)$ onto the ground state orbitals $\phi_{b\boldsymbol{k}}$:

$$f_{b\boldsymbol{k}}(t) = \sum_{c} |\langle \phi_{b\boldsymbol{k}} | \psi_{c\boldsymbol{k}}(t) \rangle|^2.$$

The occupation $f_{b\boldsymbol{k}}$ at crystal momentum $\boldsymbol{k}$ is interpreted as particle (hole) distribution for b belongs to a conduction (valence) band. We obtain laser-excited (LE) particle/hole distributions as

$$f_p^{\mathrm{LE}}(E) = \sum_{b(\in \mathrm{val.})\boldsymbol{k}} f_{b\boldsymbol{k}}(t = t_{\mathrm{end}})\, \delta(E - \epsilon_{b\boldsymbol{k}}),$$

$$f_h^{\mathrm{LE}}(E) = \sum_{b(\in \mathrm{cond.})\boldsymbol{k}} f_{b\boldsymbol{k}}(t = t_{\mathrm{end}})\, \delta(E - \epsilon_{b\boldsymbol{k}}),$$

where $\epsilon_{b\boldsymbol{k}}$ is the eigenvalue of the initial Kohn-Sham Hamiltonian. We obtain particle and hole effective temperatures, T_p, T_h, as characteristics of the distribution by fitting such that the particle (hole) distribution gives minimum error to a Fermi-Dirac distribution $f(E, \mu, T)$ at the effective temperature:

$$\arg\min_{T} \left(\int dE \left| f_{p/h}^{\mathrm{LE}}(E) - f\left(E, \mu_{p/h}, T\right) \right| \right) = T_{p/h},$$

where chemical potential is determined by a fact that energy integrals of the distribution give the same value, namely number of particle/hole conservation.

We perform TDDFT simulation for α-quartz with a driving field that have 1.60 eV, 13 fs pulse duration. The temperature depending on peak intensity are presented in Fig. 1. The Keldysh parameter, a characteristic value whether tunneling picture is valid or not, is equal to unity when the intensity is equal to 10 TW/cm^2. The temperatures monotonically increase as a function of the peak intensity. The sum of temperatures, interpreted as the averaged kinetic energy of the particle-hole pair, is 17.8 eV at 100 TW/cm^2. The value is close to the ponderomotive energy 19 eV evaluated with the reduced effective mass of 0.3. This coincidence invokes that kinetic energy gain is understood as free particle-hole motion after the tunneling ionization.

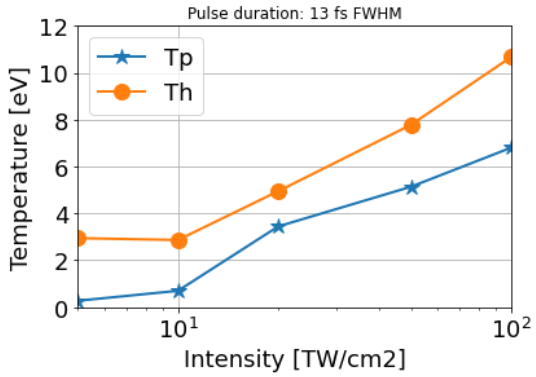

Fig. 1: Evolution of particle- and hole-temperatures.

References

[1] Erich Runge and E. K. U. Gross, Phys. Rev. Lett. **52**, 997 (1984).

[2] https://salmon-tddft.jp/, M. Noda, S.A. Sato, et al., Computer Physics Communications. **235**, 356 (2019).

Nanoscale properties and CO_2 fixation of cement-based materials : ab initio molecular dynamics simulations

Ikumi Kanemasu and Satoshi Ohmura

Department of Civil and Environmental Engineering,

Hiroshima Institute of Technology, saeki-ku, HIroshima 731-5193

The production of cement is responsible for about 8% of man-made CO_2 emissions. Therefore, CO_2 fixation technology for cementitious materials is attracting attention as a way to achieve carbon neutrality. In this project, the reaction mechanism of CO_2 with cementitious materials, specifically calcium silicate hydrate C-S-H has been reproduced using ab inito molecular dynamics simulations. Owing to its structural similarity with calcium-silicate-hydrate (C-S-H), formed by cement hydration, tobermorite is one of the main models used to simulate and study cement. First, in this study, the atomic-scale mechanism of deformation in crystalline and amorphous 11Å tobermorite under uniaxial tension and compression has been investigated using molecular dynamics (MD) simulations based on CLAYFF force field. Based on the stress-strain relationships of the uniaxial tensile and compressive deformation obtained from the MD simulations, crystalline 11Å tobermorite shows heterogeneous mechanical properties in three directions of deformation. For the amorphous state, no difference in mechanism appears depending on the direction of deformation in both tension and compression [1, 2]. Next, ab initio molecular dynamics simulations based on DFT are used to reproduce the adsorption of CO_2 on C-S-H. Figure 1 shows the atomic configurations of the adsorption process of CO_2 on C-S-H obtained from the simulation. In this process, $CaCO_3$-like structure is observed.

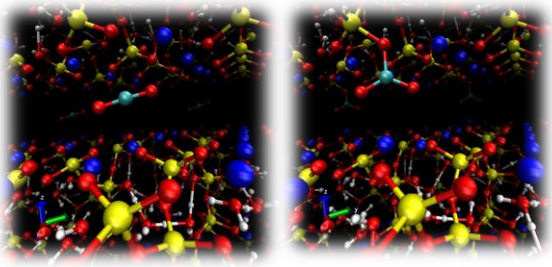

Fig. 1: Absorption process of CO2 on C-S-H.

References

[1] I Kanemasu S. Ohmura and N. Takeda, Cement Science and Concrete Technology **77** 9-16 (2023).

[2] I Kanemasu and S. Ohmura, Springer Proceedings in Physics. accepted (2023) for CCP 2023

Bowing of Energy Gap Curve for InAsSb Calculated Using VASP Based on Hybrid Density Functional Theory

Hiroki I. FUJISHIRO and Akira ENDOH

Department of Applied Electronics,

Tokyo University of Science, Niijuku, Katsushika, Tokyo 125-8585

High electron mobility transistors (HEMTs) are one of the fastest transistors for future terahertz electronics [1]. InAsSb is the most promising candidates for the channel layer of high-speed HEMTs [2] since InAsSb has the lightest electron effective mass in the III-V compound semiconductors [3]. The experimental bandgap energy E_g values for $InAs_xSb_{1-x}$ significantly lower than the linear interpolation between the E_g values for InAs and InSb, reaching a minimum at InAs content x of about 0.35. The E_g value for $InAs_{0.35}Sb_{0.65}$ is about 0.10 eV, which corresponds to the far infrared region. In this work, we obtained the energy gaps between Γ and L valley $E_{\Gamma\text{-L}}$ and between Γ and X valley $E_{\Gamma\text{-X}}$ for $InAs_xSb_{1-x}$ using Vienna Ab initio Simulation Package (VASP) based on the method in the local density approximation.

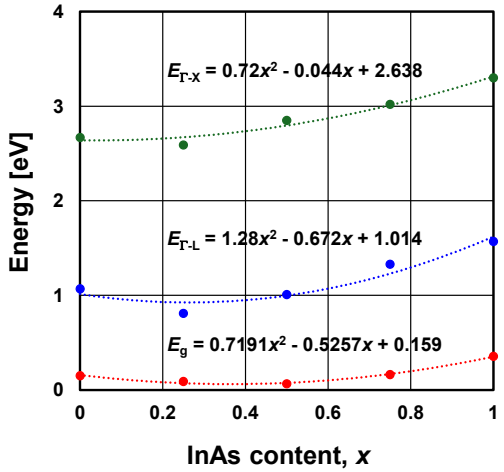

Fig. 1: InAs content x dependence of energy gaps E_g, $E_{\Gamma\text{-L}}$ and $E_{\Gamma\text{-X}}$ for $InAs_xSb_{1-x}$.

We used the hybrid coefficient of the density functional [4]. The hybrid functional is constructed by the mixing of a fraction α of the Fock exchange with a fraction $1-\alpha$ of the PBE (Perdew-Burke-Ernzerhof) exchange. The exchange-correlation energy E_{xc} can be expressed by

$$E_{xc} = \alpha E_x + (1-\alpha)E_x^{PBE} + E_c^{PBE}, \quad (1)$$

where E_x is the Fock exchange, E_x^{PBE} is the PBE exchange, and E_c^{PBE} the PBE correlation [4]. We obtained the E_g values, which are closest to the literature ones by using $\alpha = 0.21$ for InSb and $\alpha = 0.24$ for InAs. For $InAs_xSb_{1-x}$, we used linearly interpolated α values as a function of As content x, i.e., 0.2175 for $InAs_{0.25}Sb_{0.75}$, 0.225 for $InAs_{0.5}Sb_{0.5}$, and 0.2325 for $InAs_{0.75}Sb_{0.25}$ [5]. Figure 1 shows the InAs content x dependence of energy gaps E_g, $E_{\Gamma\text{-L}}$ and $E_{\Gamma\text{-X}}$ for $InAs_xSb_{1-x}$. Closed circles are the calculated values. $E_{\Gamma\text{-L}}$ and $E_{\Gamma\text{-X}}$ have

their minimum values at x = 0.25. The dashed lines in Fig. 1 indicate the fitting results by quadratic equations. The fitting equations are shown in Fig. 1. The x-dependent $E_{\Gamma\text{-L}}$ and $E_{\Gamma\text{-X}}$ curves show downwardly convex dependencies, which show similar trends to E_g [3]. The x-dependence of $E_{\Gamma\text{-L}}$ and $E_{\Gamma\text{-X}}$ obtained in this work can be applied to Monte Carlo (MC) device simulation under higher electric field where the electron intervalley transition occurs.

Acknowledgment

This work was partly supported by JSPS KAKENHI Grant Number 21K04158.

References

[1] H.-B. Jo *et al.*, Tech. Dig. 66th IEDM, no. 8-4, On-line, US, Dec. 2020.

[2] J. Zhang *et al.*, IEEE Access **7**, 102710 (2019).

[3] O. Borelo *et al.*, Phys. Rev. B **8**, 3794 (1973).

[4] T. Garwood *et al.*, Infrared Physics & Technology, 2017.

[5] H. I. Fujishiro *et al.*, Activity Report 2020, p. 128.

First-principles calculations on the electronic states of novel organic semiconductors with extended hydrogen-bonding networks

Shun DEKURA

Institute of Multidisciplinary Research for Advanced Materials (IMRAM), Tohoku University, 2-1-1 Katahira, Aoba-ku, Sendai 980-8577

The control of the molecular arrangement in organic semiconductors is important to optimize transport properties. However, conventionally, changes in molecular structure had been inevitable for the modulation of molecular arrangement. We have recently succeeded in controlling the molecular arrangement using sulfonated BTBT (= **H_2BTBTDS**) and simple amine species (**R–NH_2**) by changing only the **R–NH_3^+** cations without modulating the chemical structure of **BTBTDS^{2-}**.[1] On the other hand, the conventional evaluation of the transfer integrals between isolated molecules is insufficient for such organic semiconductors with extended hydrogen-bonding networks. In this study, we performed first-principles band calculations, and calculated the maximally localized Wannier functions (MLWFs) and the corresponding transfer integrals between MLWFs with periodic boundary condition.[2]

The first-principles band calculations were performed by using Quantum Espresso (version 6.8) for the experimentally obtained crystal structures. We employed SG15 ONCV pseudopotentials (verion 1.2) with plane-wave basis sets and GGA-PBE functional. Reasonable band structures for four types of **BTBTDS^{2-}** salts. Based on the band structures, MLWFs were calculated for HOMO- and LUMO-derived bands, respectively, by using RESPACK program. The obtained MLWFs were consistent with the shape of HOMO and LUMO calculated on the neutral semiconductor molecule, not protonated cationic state, which emphasize the importance of our approach considering periodic boundary condition. The calculated transfer integrals were also consistent with the experimentally obtained hole mobilities. The results shows that our approach is efficient to predict transport properties of hydrogen-bonded organic semiconductors.

References

1) R. Akai, K. Oka, S. Dekura, H. Mori, N. Tohnai, Bull. Chem. Soc. Jpn. **95**, 1178 (2022).

2) R. Akai, K. Oka, S. Dekura, K. Yoshimi, H. Mori, R. Nishikubo, A. Saeki, N. Tohnai, J. Phys. Chem. Lett. **14**, 3461 (2023)

First-principles study of defects in GaN

Kaori SEINO
Department of Materials Science and Engineering, Kyushu Institute of Technology
Sensui-cho, Tobata, Kitakyushu, Fukuoka 804-8550

GaN devices are the preferred candidates for next-generation power electronics. While silicon is the conventional material for power electronics, GaN offers superior physical properties such as high electron mobility, wide bandgap, and excellent thermal conductivity. Therefore, GaN devices provide much higher performance and energy savings compared to traditional silicon-based devices. One of the key technologies for high-performance GaN power devices is selective doping for *p*-type GaN using ion implantation. Recently, high-quality *p*-type GaN was achieved by Mg ion implantation with ultra-high-pressure annealing [1]. Ion implantation is advancing as an experimental technique, but theoretical efforts using first-principles calculations are necessary for atomic-scale understanding of Mg impurities in GaN. Thus far, there have been numerous investigations into various defects in GaN by first-principles calculations.

In this project, properties of defects in GaN, particularly Mg impurities in GaN, were studied by first-principles calculations. We focused on the atomic diffusion of a Mg atom in GaN here because it is crucial to understanding Mg ion implantation. We investigated the vacancy mechanism which is one of the fundamental diffusion mechanisms, using models that consist of a complex of a Mg substitutional to Ga (Mg_{Ga}) and a Ga vacancy (V_{Ga}). In the vacancy mechanism, the Mg atom migrates to the vacancy site in a complex of Mg_{Ga} and V_{Ga} (Mg_{Ga}-V_{Ga}). Thus, we analyzed diffusion processes using models as shown in Fig. 1.

We performed calculations using the hybrid approximation of Heyd-Scuseria-Ernzerhof (HSE) as implemented in the VASP code. We prepared 360-atom wurzite supercells and considered spin polarization. For the calculations of diffusion processes, we performed two approaches: using total energy surfaces and implementing the nudged-elastic-band (NEB) scheme [2]. In the NEB calculations, seven intermediate structures were employed in the reaction pathways, and parallel calculations were performed on 21 nodes in the System B. A detailed discussion will be presented elsewhere [3].

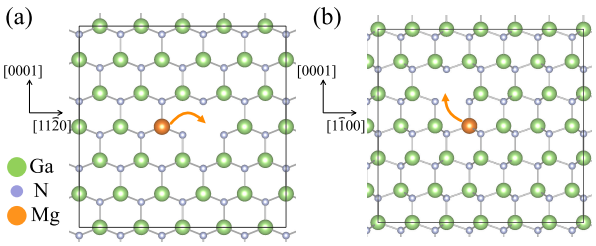

Figure 1: Schematic illustrations of the diffusion of an Mg substitutional impurity via the vacancy mechanism (a) perpendicular and (b) parallel to the c-axis.

References

[1] H. Sakurai *et al.*: Appl. Phys. Lett. **115**, 142104 (2019).

[2] G. Henkelman and H. Jónsson: J. Chem. Phys. **113**, 9978 (2000).

[3] K. Seino, A. Oshiyama, and K. Shiraishi: to be published.

Development of Stretchable Electret Materials for Energy Harvesting with the Aid of Machine Learning

Yucheng ZHANG, Yuhan Gu, Rui WANG, Kuniko SUZUKI, and Yuji SUZUKI

Department of Mechanical Engineering

The University of Tokyo, Hongo, Bunkyo-ku, Tokyo 113-8656

Electret is a dielectric material with quasi-permanent charges and can trap charges stably for decades. Vibrational electret energy harvester (VEEH) can generate electricity efficiently from kinetic energy via electrostatic induction.

CYTOP (Cyclic Transparent Optical Polymer, AGC Chemicals) shown in Fig. 1 is one of the best polymer electret materials. Recently, we utilized quantum chemical analysis for evaluating the charge trap of CYTOP electrets [1, 2]. It is found that although the repeat-unit number of CTX-A is above 1000, the trapped charge is localized at the amide bond, which is formed by a dehydration reaction between the carboxyl end group and the amine.

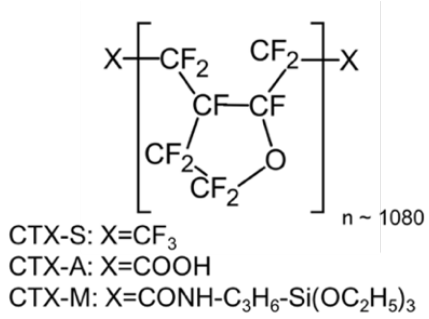

Fig. 1. Chemical structure of CYTOP series.

This result encouraged us to move further to search for a new end group in large chemical databases, aimed at designing a better polymer electret based on CYTOP CTX-A after the dehydration reaction. It is also shown that the solid-state ionization potentials (IPs) computed by the density functional theory (DFT) with the polarizable continuum model (PCM) agree well with the trends of the surface charge density and charge stability measured by the wet experiments [3, 4]. Then, the deep learning model named MEGNet [5] is employed for rapid screening of the PubChem database. We have discovered that CTX-A/BAPP (1,4-Bis(3-amino-

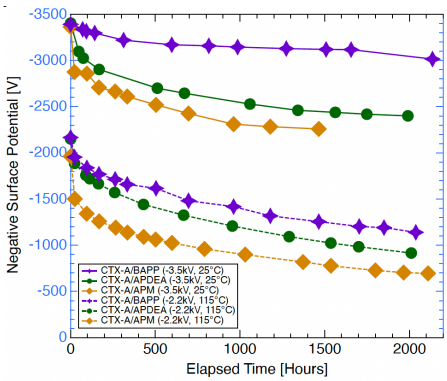

Fig. 2 Surface potential decay of different CYTOP electrets for negative/positive charging.

propyl)piperazine is one of the best candidates. Figure 2 shows the surface potential for 15 μm-thick films after charging to -3.5 kV and -2.2 kV. It is found that CTX-A/BAPP is superior to our previous materials including CTX-A/APDEA [2] in terms of charge stability. The charge-decay time constant at 80 ºC is as long as 150 years (now shown).

Based on these findings, we are now working on quantum chemical analysis of strechable electret based on fluorinated elastomer FFKM as shown in Fig. 3. Unlike CYTOP, the choice of cross linker is crucial for both higher elasticity and higher surface charge density. In addition, the molecular structure of the cross-linked structure is much bigger than CYTOP, which makes the computational cost of DFT too expensive.

All the quantum chemical calculations are made with the software GAUSSIAN [6] at the DFT level with the CAM-B3LYP functional, while PCM is combined for solid-state analysis due to the solvation effect correction.

In CYTOP cases, the 6-31+G(d,p) basis set is used and the molecule configuration is optimized with DFT. We spent a lot of effort on the systematic investigation of the simulation accuracy for different basis sets to reduce the computational cost. Finally, we found that we can get accurate solid-state IP even if we use an unoptimized molecule configuration and the 6-31+G(d,p) basis set, while the CPU time becomes at least 10 times smaller. Now, a series of DFT is made for searching a new cross-linker for a deeper charge trap in FFKM.

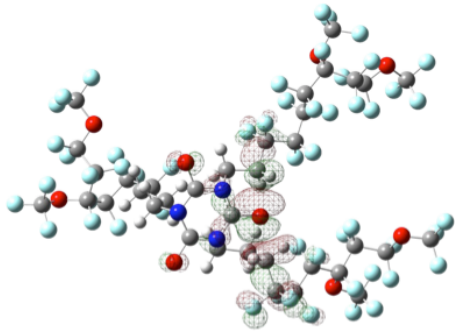

Fig. 3. Preliminary DFT results of cross-linked FFKM with TAIC.

This work was partially supported by JSPS KAKENHI 22KK0054. The calculations are performed with SGI ICE XA ISSP system B with 1 node (24 CPUs).

References

[1] Kim S., et al., J. Phys. Chem. B, Vol. 124, No. 46, pp. 10507-10513 (2020).

[2] Zhang, Y., et al., Appl. Phy. Lett., 118, 223904 (2021).

[3] Mao, Z., et al., IEEE Conf. Electr. Insul. Dielectr. Phenom., pp. 667-670 (2021).

[4] Mao, Z., et al., Adv. Mater., 2303827, (2023).

[5] Wang, R., et al., Transducers ’23, pp. 1284-1287 (2003).

[6] Frisch, M., et al., “Gaussian 09, Rev. A. 1,” Gaussian, Inc. Wellingford, CT, (2009).

Theoretical analysis of the role of neutral molecules in metal hydride ionic conductors

DOS SANTOS, E. C.

Advanced Institute for Materials Research (WPI-AIMR)

Tohoku University, Sendai, Japan 980-8577

Efficient energy storage material is vital for sustainable society establishment. Currently, lithium-ion battery is widely applied for electrical storage devices, but their cost and safety cannot satisfy large-scale applications. Fortunately, all-solid-state batteries (ASSBs) are promising alternatives with mechanical flexibility, safety, variety, and high energy density. In particular, the addition of neutral molecules is prone to promote the battery performance of multivalent closo-type metal hydrides (CTMHs), which have significant influences on the local structure of the electrolytes, thereby mixtures and multiple-phase systems are commonly obtained.

We investigate the role of neutral molecules in metal hydride ionic conductors using parallel computer simulations. The density functional calculations and molecular dynamics simulation were conducted using VASP and AIMD, respectively. Theoretical studies elucidate the structure of the closo-type boron hydrides, and a global optimization strategy is applied to generate unveiled structures. After a single system test, the individual phase effect of the CTMH complex mixtures is obtained. The global optimization and metadynamics were utilized to identify stable crystal phases of $MgB_{12}H_{12}.nH_2O$ and $ZnB_{12}H_{12}.nH_2O$ (n = {0, 6, 12}), first-principles kinetics and molecular dynamics were employed for ion diffusion kinetics, such as H_2O, NH_3, NH_3BH_3, and THF. After that, scaling relations were proposed to predict the ion diffusion performance of CTMH candidates. Based on theoretical calculations, a database was established to evaluate all possible descriptors that scale with the activation energy of the materials. The following descriptors were also evaluated: cation vacancy-free energy, number of neutral molecules in the cell, cell volume, and electronegativity of the system. Combined with the obtained scaling relations and database, new materials candidates will be selected for further evaluation.

This project analyzed local atomistic environments of the neutral molecules and diffusion of the metal ion, which strengthens the importance of CTMHs and promotes their industrial application. Furthermore, the structure performance relations (i.e., scaling relations) are established to predict new CTMH

materials candidates for battery electrolytes. Based on theoretical calculations, a database was established to evaluate all possible descriptors that scale with the activation energy of the materials. The following descriptors were also evaluated: cation vacancy-free energy, number of neutral molecules in the cell, cell volume, and electronegativity of the system. Combined with the obtained scaling relations and database, new materials candidates will be selected for further evaluation. However, obtaining SSEs with high ionic conductivity is challenging due to the complex structural information and the less-explored structure-performance relationship. This project developed a database containing typical SSEs from available experimental reports. The acquired data includes the SSE materials consisting of mono- and divalent cation components (e.g., Liþ, Naþ, Kþ, Agþ, Ca2þ, Mg2þ, and Zn2þ) and various anions (e.g., halide, hydride, sulfide, and oxide). This database provides essential guidelines for the design and development of high-performance SSEs in ASSB applications. According to machine learning and feature analyses, this database provides an opportunity to explore diverse SSE materials, which also proposes reliable structure-performance relationships. Overall, this dynamic database accelerates the discovery of novel SSEs materials with improved electrochemical performance and guides the design of optimal solid-state electrolytes. Importantly, the online surface of this database is user-friendly with dynamic updates (namely, the DDSE). This database covers critical performance indicators (i.e., ionic conductivity and ionic diffusion activation energy) of SSE materials in a wide range of temperatures.

Overall, this dynamic database accelerates the discovery of novel SSEs materials with improved electrochemical performance and guides the design of optimal solid-state electrolytes.

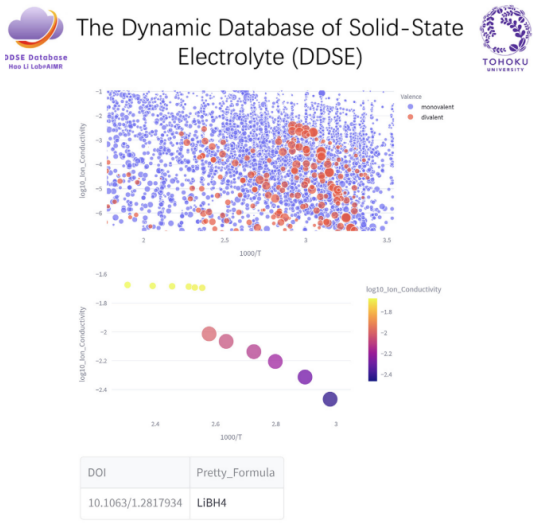

Fig. 1. Example of the online interface of the latest version of DDSE.

References

[1] Guo, Z., Yu, Y., Li, C., **Campos dos Santos, E.**, Wang, T., Li, H., Xu, J., Liu, C. and Li, H., *Angew. Chem. Inter. Edit.*, 2024,*63*, 202319913

[2] Yang, F., **Dos Santos, E.C.**, Jia, X., Sato, R., Kisu, K., Hashimoto, Y., Orimo, S.I. and Li, H., *Nano Materials* Science. 2023, DOI: 10.1016/j.nanoms.2023.08.002.

Theoretical study of oxygen-evolution reactions by first-principles calculations

Yuta TSUJI

Faculty of Engineering Sciences,

Kyushu University, 6-1, Kasuga-koen, Kasuga, Fukuoka, 816-8580, Japan

Water electrolysis devices, which can produce hydrogen either directly from solar power or from an external power source, are very attractive as a solution to the growing global demand for energy and the associated environmental problems. However, the slow reaction rate of the oxygen evolution reaction (OER) occurring at the anode of these electrolyzers has hindered the widespread use of such technologies. Therefore, the development of efficient and stable OER catalysts has been actively investigated: IrO_2 is considered the best OER electrocatalysts [1]. The high activity is also known to depend on the surface index, in the following order: $IrO_2(100) > IrO_2(110)$.

In this study, we performed ab initio calculations of the OER catalytic activity of IrO2 with various surface structures and theoretically predicted the order of catalytic activity.

Three density functional methods (PBE, RPBE, and optPBE) implemented in VASP were used to compare the activity of IrO_2 with (110), (100), and (101) surfaces (Fig. 2). The PBE and optPBE results are found consistent with the experimental results [2], but the RPBE one was found to be inconsistent with the expected.

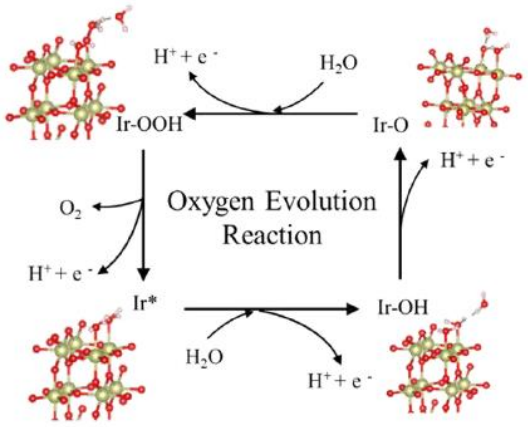

Fig. 1 Mechanism of OER.

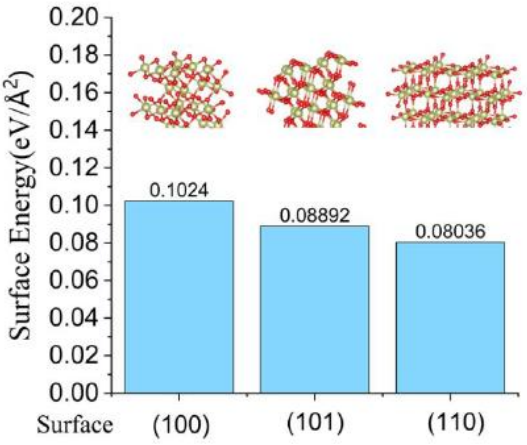

Fig. 2 Surface energies of three different surfaces of IrO_2.

References

[1] T. Reier, M. Oezaslan, P. Strasser, ACS Catalysis **2**, 1765 (2012).

[2] L. G. V. Briquet, M. Sarwar, J. Mugo, ChemCatChem **9**, 1261 (2017

Electronic state analysis on molecular thin film surface

Kaori Niki

Graduate school of science

Chiba University, Yayoi-cho, Inage-ku, Chiba 263-8522

Introduction

In photoelectron spectroscopy, significant advances in detectors have been made since around 2015, allowing measurements in all directions in wavenumber space in a short time. This method is called wave number resolved photoelectron spectroscopy. Recently, structural changes of Copper(II)phthalocyanine (CuPc) adsorbed on $TiSe_2$ surface were observed under laser irradiation. It was suggested that the electron transition from the $TiSe_2$ surface to CuPc induces the structural deformation due to the change in charge distribution. In this study, ground-state and Molecular Dynamics (MD) performed to calculate the electronic state during adsorption.

Method

We performed density functional theory (DFT) calculations using the Vienna Ab Initio Software Package (VASP) version 5.4.4 [1,2]. The exchange correlation effects were described by the spin-polarized generalized gradient approximation (GGA) within the Perdew-Burke-Ernzerhof (PBE) formalism [3]. We used a 8×8×1 $TiSe_2$ slab with lattice constants a = b = 3.53 Å, c = 20.0 Å, α = β = 90° and γ = 120°, and a plane-wave basis set with the projector augmented wave (PAW) approach with an energy cutoff of 380 eV. The Brillouin zone integration was performed on a Monkhorst-Pack of 18×18×1 grid of k-points. The energy convergence criterion chosen for the self-consistency cycle was 1×10^{-7} eV. To account for Fermi surface broadening, temperature parameter σ for Methfessel-Paxton smearing was applied. So far, we have found the parameter set (Hubbard parameter = 3.9 eV and σ = 0.01 eV), which reproduces the experimental results [4]. We used these parameters for the MD simulation of the CuPc / $TiSe_2$ structure. After relaxing the geometries at 0 K, the systems were brought up to 654 K by repeated velocity rescaling using the spin-polarized PBE+U DFT-D3 functional at the Γ-point. Then 5 ps microcanonical MD trajectories were generated with a 1 fs time step.

Results

MD calculations of the structures of CuPc and CuPc+ on $TiSe_2$ show that CuPc and CuPc+ are bent, which reflect the structures under light irradiation.

Using this structures, we succeeded in reproducing the X-ray photoelectron spectroscopy (XPS) calculations by using the original photoelectron intensity calculation

software.

Conclusion

By performing MD calculations using VASP, we clarified structural changes and substrates with increasing temperature by irradiation.

References

[1] G. Kresse and J. Hafner, Phys. Rev. B **47**, 558 (1993).

[2] G. Kresse and D. Joubert, Phys. Rev. B **59**, 1758 (1999).

[3] J. P. Perdew, K. Burke, and M. Ernzerhof, Phys. Rev. Lett. **77**, 3865 (1996).

[4] B. Singh *et. al.*, Phys. Rev. B **95**, 245136 (2017).

Modeling of the Ammonia Decomposition Reaction on Iron-based Material Surfaces

Peijie FENG, Minhyeok LEE, and Yuji SUZUKI

Department of Mechanical Engineering, School of Engineering,

The University of Tokyo, 7-3-1 Hongo, Bunkyo-ku, Tokyo 113-8656

Ammonia is considered a promising next-generation green energy carrier, but employing ammonia directly as a fuel is challenging because of its low flammability and the potential for NOx emissions [1]. Currently, research on ammonia-related reaction kinetics primarily focuses on DeNOx applications, leading to models that often lack robustness in environments devoid of oxygen, where thermal decomposition predominates [2].

Our previous study [3] revealed a mutual interaction between ammonia and iron-based materials: ammonia thermally decomposes on iron-based materials, converting them into iron nitride. This iron nitride, in turn, facilitates the thermal decomposition of ammonia more significantly than pure iron does. To understand the dynamics of the nitriding process in conjunction with thermal decomposition, molecular dynamics that can simulate chemical reactions is preferred.

However, there is a lack of an iron-nitrogen molecular dynamics force field capable of accurately representing both crystalline iron/iron nitride and molecular ammonia, along with other gas-phase products. Furthermore, existing force fields predict energies and forces poorly, particularly at high temperatures where thermal decomposition occurs.

To address these challenges, we embarked on conducting *ab initio* molecular dynamics (AIMD) using the Vienna Ab initio Simulation Package (VASP) via the supercomputer system at ISSP. This allowed us to generate a series of training trajectories, along with related energies/forces. The target crystal systems are listed in Table 1. Subsequently, DeepMD-kit [4] is incorporated to construct a machine learning interatomic force field (MLFF) for running MD simulations using the ISSP system C.

Figure 1a demonstrates that the MLFF, even with a limited amount of input data, significantly outperforms the conventional Modified Embedded Atom Method (MEAM) force field, exhibiting lower errors and virtually no bias compared to Density Functional Theory (DFT) results. The capability of transfer learning and extrapolation by the MLFF is evidenced in Fig. 1b, which assesses the MAE and RMSE

Table 1. AIMD calculate systems.

		Space Group	Crystal system	Magnetic	N %	N wt%	Exp. Observed	MD Atoms Fe:N	Minimum Size	Short AIMD 500~1000fs
01	Fe (mp12)	Im3-m	Cubic	o	0.00%	0.00%	o	250:0	15.0Å	**1000,500K**
02	Fe (mp-136)	$P6_3/mmc$	Hexagonal	x	0.00%	0.00%	o	288:0	13.0Å	**1000,500K**
03	Fe (mp-150)	Fm3-m	Cubic	x	0.00%	0.00%	o	108:0	10.9Å	**800**,500K
04	Fe8N (mp-555)	I4/mmm	Tetragonal	o	11.11%	3.03%	o	432:54	16.7Å	**1000,500K**
05	Fe4N (mp-535)	Pm3-m	Cubic	o	20.00%	5.88%	o	256:64	14.8Å	**1000,500K**
06	Fe3N (mp-1804)	$P6_322$-	Hexagonal	o	25.00%	7.69%	o	384:128	15.9Å	**1000,500K**
07	Fe12N5 (mp-27908)	P3-1m	Trigonal	o	29.41%	9.43%	o	288:120	12.7Å	**1000,500K**
08	Fe2N (mp-248)	P3-1m	Trigonal	o	33.33%	11.11%	o	216:108	12.7Å	**1000,500K**
09	Fe2N (mp-21476)	Pbcn	Orthorhombic	o	33.33%	11.11%	o	162:81	12.7Å	**1000,800,500K**
10	FeN (mp-6988)	F4-3m	Cubic	o	50.00%	20.00%	o	150:150	11.7Å	**1000,500K**
11	FeN (mp-12120)	$P6_3/mmc$	Hexagonal	o	50.00%	20.00%	o	256:256	16.8Å	**1000,500K**

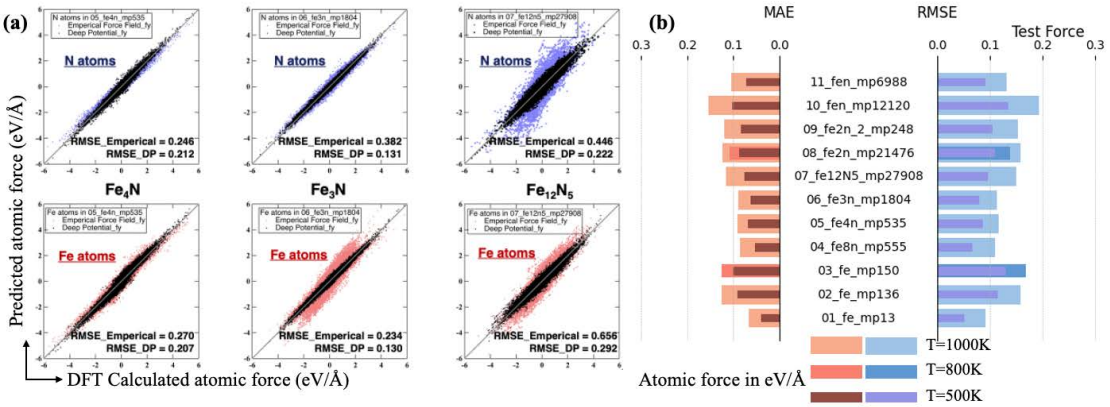

Figure 1. Testing result of force predictions using the trained MLFF. DP denotes MLFF from DeepMD, Emperical denotes the force predicted from the only available MEAM classical force field [5]. (a) Comparing the force prediction between MLFF and Emperical, using DFT calculated force as grouped truth. (b) Mean average error (MAE) and root-mean-square error (RMSE) of atomic forces in the test dataset.

through k-fold cross-validation. This evaluation was achieved by entirely omitting the training data for one system, thereby implying that the MLFF, without being trained on such a system, can predict it with an average error of less than 0.2eV/Å.

In conclusion, the MLFF surpasses the classical MEAM force field in performance and shows great promise for accurately predicting the potential energy surface of chemical reactions, assuming the MLFF is trained with well-curated DFT data. The capability of the MLFF to predict forces accurately along reaction pathways will be verified in future studies.

References

[1] M.V. Manna, P. Sabia, R. Ragucci, M. de Joannon, Fuel **264**, 116768 (2020).
[2] P. Glarborg, H. Hashemi, and P. Marshall, Fuel Commun. **10**, 100049 (2022).
[3] P. Feng, M. Lee, D. Wang, Y. Suzuki, Int. J. Hydrog. Energy **48**, 75 (2023).
[4] H. Wang, L. Zhang, J. Han, E. Weinan. Comput. Phys. Commun. **228**, 178 (2018).
[5] B. Lee, T. Lee, S. Kim, Acta. Mater. **54**, 17 (2006)

First-principles study of surface atomic structure and chemical properties of intermetallic compounds

Kazuki Nozawa

Department of Physics and Astronomy, Kagoshima University,

1-21-35, Korimoto, Kagoshima 890-0065

Trace-amount Pt-doped $Al_{13}Fe_4$ is considered a promising model system for investigating single-atom catalysis, as the doped Pt atoms are dispersed by occupying a specific atomic site[1]. Although it was reported that the conversion of the doped system for the hydrogenation of C_3H_4 is higher than that of the non-doped system, details, including the surface structure, are still unclear.

Thus, this year, we investigated the surface structure of trace Pt-doped $Al_{13}Fe_4$ using first-principles calculations. We used the VASP code for the calculation. The unit cell contains 102 atoms (Al:78, Fe:24) occupying 20 inequivalent crystallographic sites. First, we evaluated the formation enthalpy by replacing one of the crystallographic sites with Pt, corresponding to approximately 1 atom % doping. Then, we composed the convex hull using the obtained formation enthalpy to determine the thermodynamically stable phase. The results indicate that doped Pt prefers to substitute the Fe(1) site as experimentally reported for a 0.2 atom % doped system[1]. The crystal structure of $Al_{13}Fe_4$ is described by alternatively stacking two atomic layers, the flat layer and the puckered layer, along the [010] direction. We performed simulated cleavage calculations[2] by extending the simulation cell in this direction to obtain a stable surface structure. The puckered layer is divided into two parts during the cleavage process, and the obtained most stable surface is composed of the incomplete puckered layers and the flat layer exposed between the incomplete puckered layers. The doped Pt atom is situated in the flat layer, most of which is exposed to the surface. Therefore, the doped Pt atoms can be worked as a catalytically active site. Further studies on the catalytic properties of this surface are ongoing.

References

[1] T. Yamada et al., J. Am. Chem. Soc. **140**, 3838 (2018).

[2] M. Kračji and J. Hafner, Phys. Rev. B 84, 115410 (2011).

[3] S. Iwado, Master Thesis (Kagoshima University, 2024).

Prediction of properties of organic ferroelectrics and piezoelectrics by first-principles calculation

Shoji ISHIBASHI
National Institute of Advanced Industrial Science and Technology (AIST)
Tsukuba, Ibaraki 305-8568

For the 2,5-dihydroxybenzoic acid (DHBA) crystal, two possible switching mechanisms have been noted recently [1]. One is a flip-flop (FF) motion of hydroxy groups, and the other is inter-molecular proton transfer (PT). In Fig.1, structural snapshots of hydroxy groups in both the processes together with Berry phase variation [2]. λ and λ' are parameters to describe the FF and PT processes, respectively. $\lambda = +1$ and $\lambda' = +1$ correspond to the same target ferroelectric structure. The polarization-inverted structure in the PT process is described as $\lambda' = -1$ and its phase differs by 2π from that of $\lambda = -1$ reflecting the proton movements at the hydroxy groups. The Berry phase variation shows that the sign of the polarization-vector component differs between the two processes. The direct piezoelectric coefficient is evaluated, adjusting the polarization-vector component to be positive, from its change upon applying stress. The converse piezoelectric coefficient is evaluated by adjusting the sign of the electric-field component to be the same as that of the polarization-vector component. On the other hand, small structural changes are expected under a stress or an electric field. The change in polarization as a vector is uniquely defined and independent of the switching mechanism. Hence, the switching modes can be distinguished.

Using the QMAS code, we have performed computational simulations of the direct and converse piezoelectric effects for DHBA and also for Hdabco-ReO_4. By comparison with the experimental results, it is concluded that DHBA employs the FF process for its switching mechanism, whereas Hdabco-ReO_4 adopts the PT process.

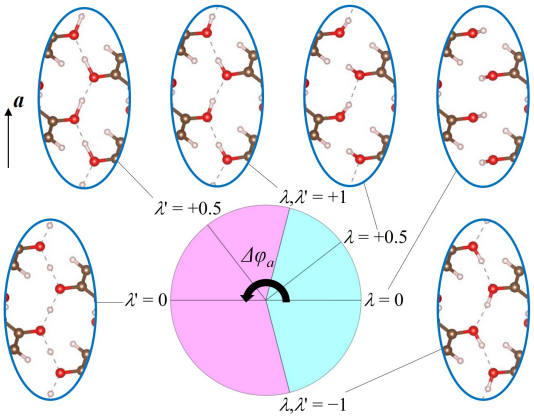

Figure 1: Berry phase variation ($\Delta\phi_a$) and structural snapshots of hydroxy groups during ferroelectric switching in the FF (λ) and PT (λ') processes for DHBA (S. Ishibashi, R. Kumai, and S. Horiuchi, Sci. Rep. **13**, 8810 (2023), DOI: 10.1038/s41598-023-34923-0).

References

[1] Y. Shimoi, S. Tsuzuki, R. Kumai, M. Sotome, and S. Horiuchi, J. Mater. Chem. C **10**, 10099 (2022).

[2] S. Ishibashi, R. Kumai, and S. Horiuchi, Sci. Rep. **13**, 8810 (2023).

Development of First-principles Codes for Evaluation of Physical Properties Through Local Berry Phases

Naoya YAMAGUCHI
Nanomaterials Research Institute (NanoMaRi), Kanazawa University
Kakuma-machi, Kanazawa, Ishikawa 920-1192

This year we continued to develop the calculation code for the coefficients of the magnetic thermoelectric effects, the anomalous Hall and Nernst effects [1], as a code for the evaluation of the physical properties of the local Berry phase method. First, we performed applied calculations on the subject of Heusler alloy systems to investigate their defect effects. When expanding the system using supercells, the computational cost increases due to the larger number of atoms, but in addition, there is the problem of increasing the number of degenerate points that induce numerical instability due to the folding of the Brillouin zone. To avoid that numerical instability, we tried devising various calculation methods for the Berry curvature evaluation routine and found that the most robust results were obtained by approximating with the minor determinant. The implementation is already MPI parallelized for k points. It will also be extended to a combined version of the modified tetrahedron method, and the improved calculation code will be evaluated through trial application calculations in the future.

We have also developed a calculation method to decompose the anomalous Hall and Nernst conductivity into the contributions of each layer in layered materials. By unitary transformation of the Bloch wavefunctions, we constructed hybrid Wannier functions localized only in the direction orthogonal to the plane of each layer, formulated a method for finding the anomalous Hall conductivity at the Wannier center, and implemented the code with the MPI parallelization for the k-points. Using this, it was confirmed that the even-layered antiferromagnetic $MnBi_2Te_4$ is an axion insulator exhibiting a surface anomalous Hall effect, where the conductivity is $1/2$ in e^2/h units at the surface. The computational model was based on the structure of odd-layered $MnBi_2Te_4$ used in last year's study [2], which was an interlayer antiferromagnetic magnetic structure. Such a calculation method for "layer anomalous Hall conductivity" is expected to be applied to a wide range of systems, including two-dimensional stacking materials and artificial superlattices.

As an application of the code developed last year for the evaluation of magnetic thermoelectric properties [1], we predicted the anomalous Nernst coefficient in Cr-doped Bi_2Se_3 which is a Chern insulator [3]. The code was also used in a theoretical study of the mechanism of the giant magnetic thermoelectric effect induced by the van Hove singularities [4].

Furthermore, in the case of tight-binding models or atomic basis set, we developed a method to avoid many eigenvalue problems by combining a highly efficient Berry phase calculation routine developed last year when implementing the electric field application method [5] with the density matrix based on that basis.

The development of the above calculation codes was done while implementing them in the first-principles calculation code OpenMX [6].

References

[1] H. Sawahata, N. Yamaguchi, S. Minami, F. Ishii, Phys. Rev. B **107**, 024404 (2023).

[2] Y. Morishima, N. Yamaguchi, H. Sawahata, F. Ishii, Appl. Phys. Express **16**, 043003 (2023).

[3] R. Syariati, V. Saraswati, H. Sawahata, N. Yamaguchi, F. Ishii, Jpn. J. Appl. Phys. **63**, 01SP26 (2024).

[4] K. Shibata, N. Yamaguchi, H. Sawahata, F. Ishii, J. Phys. Soc. Jpn. **92**, 124704 (2023).

[5] N. Yamaguchi, F. Ishii, Comput. Phys. Commun. **280**, 108487 (2022).

[6] http://openmx-square.org.

Oxygen and hydroxyl groups on Pt Nanoparticles

Takehiko SASAKI and Yasumasa IMAI

Department of Complexity Science and Engineering, Graduate School of Frontier Sciences, The University of Tokyo, Kashiwa-no-ha, Kashiwa, Chiba 277-8561

In order to elucidate and improve the operation of fuel cells (PEFC), it is important to elucidate the electrochemical cycle on the surface of platinum nanoparticles and the adsorption state on the electrode surface. We determined the structures of various oxygen adsorption states on the surface of platinum nanoparticles and the free energy for the electrochemical process of oxygen and OH adsorption reactions.

The Pt nanoparticles to be calculated are Pt nanoparticles composed of 586 atoms of the cuboctahedron type corresponding to the actual catalyst particle size range of 2.5 nm. DFT calculations were conducted using VASP. The unit cell has a volume of 22.13×44.26×33.19 ($Å^3$) and contains 215 Pt atoms and oxygen atoms. After optimization of this unit cell, cuboctahadral nanoparticle is obtained by symmetry operation. The structure optimization calculation was performed by allowing the relaxation of the first and second neighbors of oxygen atoms and hydroxyl groups. The energy cutoff was 400 eV and the k-point mesh was 3x2x2. For each structures free energy change (ΔG) for electrochemical adsorption process was calculated following previous studies [1,2]. The obtained relationship as a function of electrochemical potential is shown in Fig. 1. From this figure the major species on Pt nanoparticles can be assigned as the one with the negative largest ΔG value upon sweeping the electrochemical potential. This information is used for the analysis of *in-situ* XANES.

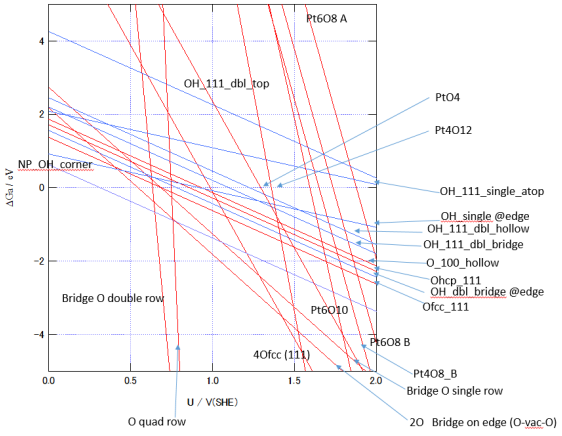

Fig. 1 ΔG for surface oxygen and hydroxyl groups on Pt cluster as a function of electrochemical potential.

References

[1] J.K. Norskov et al. , J. Phys. Chem. B **108**, 17886 (2004).

[2] R. Jinnouchi et al., Catal. Today **262**, 100 (2016).

Finite-temperature electronic transport of CoSi alloys with transition metals (Fe, Cr, Mn, Ni) using KKR-CPA method

Ho Ngoc NAM

Department of Materials Process Engineering,

Nagoya University, Furu-cho, Chikusa, Nagoya 464-8603

Most state-of-the-art thermoelectric materials are semiconductors, whereas metallic materials are abundant but have received less attention due to their typically low Seebeck coefficients and high thermal conductivity values. CoSi, an intermetallic compound with a high power factor, has recently attracted significant curiosity as a potential metallic candidate. However, theoretical studies on electronic transport in CoSi using Boltzmann's approach within relaxation time approximation suggested significant deviations compared to experimental observations, especially electrical resistivity [1]. Accordingly, the efficiency in the treatment of phonon scattering or the lack of vertex correction could be reasons.

To handle these issues, in FY2023, we employed a superior approach using the Korringa-Kohn-Rostoker Green's function method combined with the coherent potential approximation (KKR-CPA) to gain insight into the electronic transport properties of CoSi. In addition, to improve its electrical conductivity, we alloyed this material with transition metals.

In particular, by taking into account both scatterings of random chemical species and thermal-induced atomic displacements as well as the vertex correction, the electrical resistivity of CoSi observed in experiments could be quantitatively reproduced [2]. It also reveals the effect of antisite disorders on resistivity in a low-temperature range. Alloying CoSi with several transition metals (i.e., Fe, Cr, Mn, Ni) at various concentrations reveals significant changes in states of conduction electrons for specific dopants (Fig. 1) and successfully improved the system's conductivity (~25%) with Ni dopant.

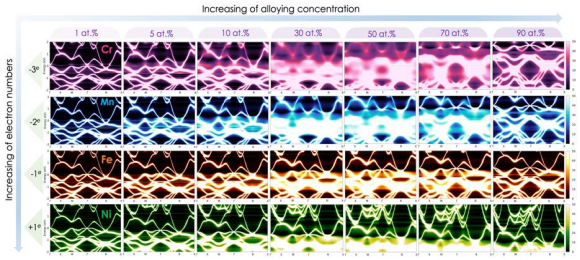

Fig. 1: Room temperature Bloch spectral function of $Co_{1-x}M_xSi$ (where M = Fe, Cr, Mn, Ni) at different alloying concentrations.

References

[1] H. N. Nam, K. Suzuki, A. Masago, H. Shinya, T. Fukushima, and K. Sato: Jpn. J. Appl. Phys. **62** (2023), 020904.

[2] H. N. Nam, Q. M. Phung, K. Suzuki, H. Shinya, A. Masago, T. Fukushima, and K. Sato: J. Mater. Chem. A **12** (2024), 451-459.

Simulations of small cluster of CeO_2

Akira Yoko

Advanced Institute for Materials Research,

Tohoku University, Katahira 2-1-1, Aoba-ku, Sendai, Miyagi 980-8577

We have studied the synthesis and characterization of CeO_2 nanoparticles. CeO_2 nanoparticles have great performance as catalyst or oxygen carrier when the surface is well controlled [1,2].

Recently, it was found that the catalytic activity of CeO2 nanoparticles had clear particle size dependence, which is not explained by the surface area increase. The origin of the catalytic performance enhancement was studied experimentally, and lattice distortion was raised as the potential origin of the high performance. The lattice distortion was caused because of the decrease in particle size, and that affects the activity of oxygen in CeO_2 nanoparticles [1,2].

In addition, we have recently achieved precise control of CeO_2 nanoparticles using continuous flow hydrothermal method. CeO_2 nanoparticles ranging from 1 nm to 9 nm were synthesized just by changing residence time based on the precursor chemistry and the elucidation of the organic modification mechanism. Interesting physical properties such as ferromagnetism and luminescent were emerged for these CeO_2 nanoparticles, and further study of these new materials are required. In this study, small clusters of CeO_2 were studied in terms of the structure and structural distortion. Without any vacancies, particles distorted because of the surface effects and surface construction with Ce and O with polarity (Fig. 1). Further simulations are necessary to elucidate new properties of those clusters.

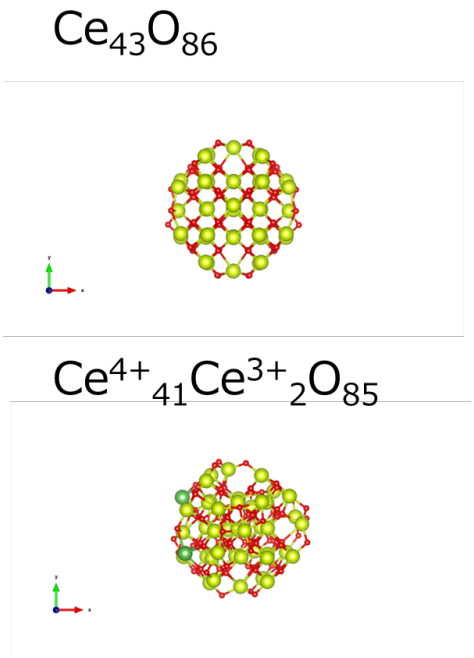

Fig. 1 Example of the simulated clusters

References

[1] X. Hao, et.al., Small, 14(42), 1802915 (2018).

[2] X. Hao, et.al., Acta Materialia, 203, 116473 (2021)

Machine learning study on static structure of light metals alloys based on *ab initio* molecular dynamics

Akihide KOURA

Technical division, Kumamoto University, Kumamoto 860-8555, Japan

It is important to investigate the microscopic mechanism of amorphization of $Mg_xZn_yY_{1-x-y}$ alloy, which is expected to be the material for vehicles and airplanes due to its light mass and strength. It is considered that the Zn_6Y_8 cluster is related with the toughening, however, the detail of the clustering mechanism during amorphization process is not clear. In this project, we focused on the concentration of $Mg_{0.816}Zn_{0.008}Y_{0.111}$ alloy to clarify the structure and dynamics of the liquid and amorphous state based on the *ab initio* molecular dynamics (AIMD) simulations. Furthermore, to decrease the calculation time, we also employ the artificial neural network [1] to make machine learning interatomic potential (MLIP) from the data of the AIMD simulations. Here, we employed the QXMD code for AIMD and MD simulations [2]. To construct the MLIP, we also used the Aenet package [1].

Figure 1 shows partial radial distribution functions $g_{\alpha\beta}(r)$ of liquid state of the Mg alloy at 1000 K. The red dashed line shows $g_{\alpha\beta}(r)$ obtained from AIMD consisting of 288 (232 Mg, 24 Zn, and 32 Y) atoms. The black and green lines correspond to those from MD simulations using different MLIPs consisting of 2304 (1856 Mg, 192 Zn, and 256 Y) atoms. Due to the small number of Zn and Y atoms, training was difficult as shown by the green line, however, averaging several MLIPs makes MD simulation robust as indicated by the black line, of which correlation functions are in good agreement with those by AIMD simulations. While, there was still room for improvement on the learning about small number of atoms.

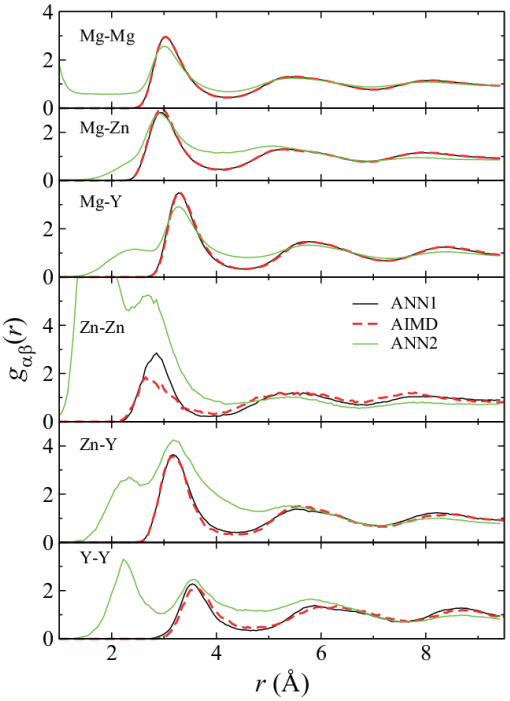

Fig.1: Partial radial distribution functions $g_{\alpha\beta}(r)$. The red dashed line shows the result of the AIMD simulation. The black and green solid lines indicate that of MLIP-MD simulations.

References

[1] N. Artrith and A. Urban, Comput. Mater. Sci. **114**, 135 (2016).

[2] F. Shimojo, *et al.*, SoftwareX **10**, 100307 (2019).

Study on the Removal Mechanism of Copper Oxide Processing by Catalyst-Referred Etching Method

Pho Van BUI, Daisetsu TOH, Kouji INAGAKI, Yoshitada MORIKAWA

Graduate School of Engineering,

Osaka University, 2-1 Yamada-oka, Suita, Osaka 565-0871

Polishing is an extremely important technique used in the finishing processes for optical and semiconductor surfaces and determines the performance of the final products. To produce smooth surface without introducing any crystallographically damaged surface, only pure chemical etching method is desired. Recently, catalyst-referred etching (CARE) method using Pt catalyst and water (as an etchant) has been proposed [1]. CARE can planarize SiC and various crystalline semiconductor materials to atomically smooth surfaces [2,3]. The main role of the catalyst is to dissociate water molecules and to stabilize the five-fold coordinated states.

Recently, transition metal oxide processing has raised much attention thanks to its importance in electronic device fabrication. Cu is commonly used as a lead in electronics thanks to its excellent electrical conductivity. In the processing, Cu is oxidized and is planarized to the desired surface quality. Experimental results have indicated that a Copper oxide layer could be planarized via CARE with a Pt catalyst. Thus, it is important to understand the removal mechanism to fully develop this technique for the practical application of CARE. Thus, density functional theory (DFT+U) based calculations for CuO(100) and CuO(111) (Fig. 1) have been performed in this study. The calculations were performed by the first-principles approach using the STATE-senri program package. The first-principles simulations were based on the generalized gradient approximation (GGA) with the Perdew-Burke-Ernzerhof (PBE) functional. Ion cores were replaced by ultrasoft pseudo-potentials for the Cu, H, O, and Pt atoms. Valence wave functions and charge densities were expanded in the plane wave basis sets with cut-off energies of 25 and 225 Ry, respectively. To calculate the reaction pathway, the climbing image nudged elastic band method was adopted.

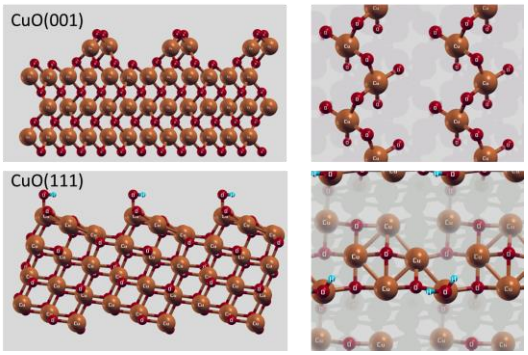

Fig. 1: Side and top views of the CuO(001) and CuO(111) slab models.

In the first step of calculations, the interaction

of the stepped CuO(001) and CuO(111) with water molecules is investigated. For the CuO(001), the first water molecule adsorption and first Cu-O bond dissociation required no activation barrier. By introducing one more water molecule, there is no required activation barrier too. However, the dissociation barrier for the Cu-O bond required an activation barrier of approximately 1.18 eV. The obtained results are summarized in Fig. 2.

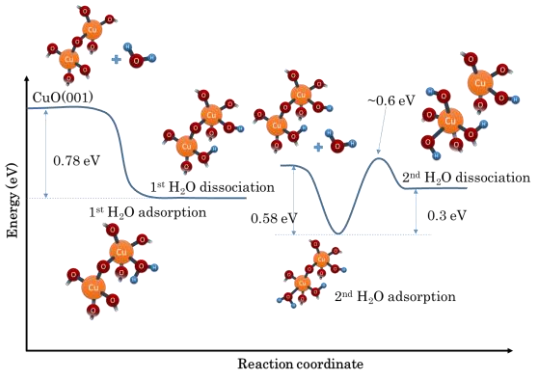

Fig. 2: Water adsorption and dissociation on the stepped CuO(001) surface.

For the CuO(111) surface, the first water molecule adsorption and dissociation required an activation barrier of 0.42 eV (Fig. 3).

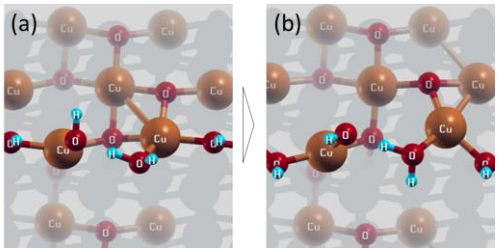

Figure 3: First water molecule adsorption and dissociation on the CuO(111) surface: (a) Adsorbed state and (b) Dissociated state.

In the next step of study, we tried to put a Pt(111) slab model on top of the CuO model to investigate the catalytic effects of Pt to the etching of CuO (Fig. 4).

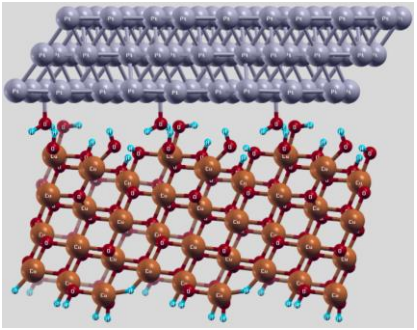

Fig. 4: Pt-CuO model

In the Pt-CuO model, due to the complexity of the interface interaction, some modifications to the code is required. Thus, we will try to solve this problem by implementing Vanderwal correction to DFT+U in the near future.

In summary, by using simplified models of CuO, the interaction of CuO with water was investigated. Without Pt catalyst, the chemical reaction of water with CuO is difficult to occur. However, by implementing Pt slab model, the calculation of the Pt-water-CuO system did not go well due to the complicated interaction between the two solid interfaces.

References

[1] H. Hara, Y. Sano, H. Mimura, K. Arima, K. Kubota, K. Yagi, J. Murata, and K. Yamauchi, J. Electron Mater. **35**, L11 (2006).

[2] D. Toh, P.V. Bui, N. Kidani, S. Matsuyama, Y. Sano, Y. Morikawa, and K. Yamauchi, K. Rev. Sci. Instrum. **90**, 045115 (2019).

[3] A. Isohashi, P.V. Bui, D. Toh, S. Matsuyama, Y. Sano, K. Inagaki, Y. Morikawa, and K. Yamauchi, Appl. Phys. Lett. **110**, 201601 (2017.

Transport study of graphene and carbon nanotubes

Yoshitaka FUJIMOTO
School of Engineering, Kyushu University
Moto-oka, Fukuoka-city, Fukuoka 819-0395

Carbon-based materials like carbon nanotubes (CNTs) and graphene are one of the most promissing device materials in electronics and sensors. The doping of heteroatom to graphene and CNTs is reported to modify their electronic structures. In addition, the adsorption properties of the carbon-based materials are reported to be improved by doping with heteroatoms [1]. Actually, it has been reported that the boron-doped graphene can strongly bind with harmful NO_x molecules [2, 3]. Furthermore, the B-doped CNTs can adsorbe the toxic CO molecule and the conductivity of the B-doped CNTs is largely changed by the adsorption of the CO molecule, suggesting the possibility to fabricate the toxic CO sensors [3, 4]. However, in the previous study, the calculation of the transport property has been performed with only a single dopant in the CNT. In the real systems, CNTs might have many defects [5]. Here, we investigate the effects of the molecular adsorption on the electronic transport of the nanotube with a defect density.

We here exmaine the adsorption properties of various molecules including environmentally toxic molecules on the B-doped (14,0) CNTs. Table 1 shows the adsorption energy and the binding distance between the molecule and the B atom in the B-doped CNTs. It is found that the CO and O_2 molecules are adsorbed with relatively large adsorption energies as well as short binding distances. It is also found that the B atoms in the B-doped CNTs protrude from the tube surface when CO and O_2 molecules are adsorbed on the B-doped CNTs. On the other hand, the CO_2 and N_2 molecules weakly bind with relatively small adsorption energy and long binding distances. In addition, the adsorption energy of the CO molecule on the B-doped (14,0) CNT is smaller than those on the B-doped (8,0) and (10,0) CNTs.

We here investigate how the introduction of the B atom and the adsorption of molecules affect the electronic transport of (14,0) CNTs. The (14,0) CNT is a semiconductor with a band gap of about 0.46 eV. The conductance spectrum of the pristine CNT shows a quantized value and step-like structures. It is found that the pristine (14,0) CNT possesses the conductance of 2 G_0 ($G_0 = 2e^2/h$) near the valence-band and the conduction-band edges.

When a B atom is doped to the semiconducting CNTs, the acceptor states appear near the valence-band maximum, and the Fermi energy of the B-doped CNT relatively moves toward the valence bands. Therefore, the B-doped CNT should act as a *p*-type semiconductor. When a CO molecule is adsorbed to the B-doped CNT, the conductance spectrum largely changes: the adsorption of the CO molecule overall reduces the conductance of the B-doped CNTs. When the O_2 molecule is adsorbed, the conductance spectrum of the B-doped CNTs overall reduces as well. However, the slope of conductance spectrum of the O_2-adsorbed B-doped CNT between $E = 0$ and -0.5 eV is different from that of the CO-adsorbed one.

In summary, the effects of doping and adsorption of molecules on energetics and electronic transport of B-doped (14,0) CNTs have been examined based on the first-principles electronic transport study. The CO and O_2 molecules are adsorbed on the B-doped CNTs with relatively large adsorption energies, while CO_2 and N_2 molecules are weakly adsorbed with long binding distances. The calculation of the electronic conductance of the (14,0) CNTs has been carried out. It is found that the electronic conductance of the CNTs changes

Table 1: Adsorption energy E_a (eV) and distance d (Å) from the B atom for each molecule adsorbed on B-doped (14,0) CNT.

	CO	CO_2	O_2	N_2
E_a	−0.30	−0.01	−0.20	−0.21
d	1.54	2.62	1.66	3.37

largely by the introduction of the dopant atom and the adsorption of the molecules. Thus, the B-doped CNT is a useful material to selectively detect toxic CO and common O_2 molecules.

References

[1] Y. Fujimoto and S. Saito, Chem. Phys. **478**, 55 (2016).

[2] Y. Fujimoto and S. Saito, Jpn. J. Appl. Phys. **58**, 015005 (2019).

[3] Y. Fujimoto and S. Saito, Appl. Surf. Sci. Adv. **1**, 100028 (2020).

[4] Y. Fujimoto and S. Saito, J. Electrochem. Soc. **169**, 037512 (2022).

[5] Y. Fujimoto, J. Electrochem. Sci. Eng. **12**, 431 (2022).

Interactions between impurities and vacancy-helium complexes in metallic materials

Kazuhito Ohsawa

Institute for Applied Mechanics, Kyushu University,

Kasuga-koen 6-1, Kasuga, Fukuoka 816-8580

Introduction

Tungsten (W) and Iron (Fe) are important materials for plasma facing materials (PFMs) used in fusion reactors. Vacancy (V) nucleated under the irradiation circumstance in the metallic materials are considered to be trap sites of a large amount of helium (He) atoms. According to first-principle calculations, more than 30 He atoms can be accommodated in the vacancy. So, the effects of the vacancy-helium (V-He) complexes, vacancy trapping one or multiple He atoms, on the metallic materials were investigated in the present works. In particular, we focused on the interactions between the V-He complexes and typical impurities in the metallic materials. For example, rhenium (Re) is produced in W specimen by nuclear transmutation in the neutron irradiation circumstance. Besides, cupper (Cu) precipitation in Fe causes the embrittlement of steal. In the present work, we investigated interactions between impurities Re and Cu and V-He complexes in W and Fe specimen, respectively. The simulations will contribute to the study of radiation damage formation.

Simulation method

Binding energy E_b between impurity X and V-He complex was estimated in terms of first-principle calculations.

$$E_b = E[M_{m-1}VHe_n] + E[M_{m-1}X] - E[M_{m-2}VHe_nX(k)] - E[M_m], \quad (1)$$

where E is cohesive energy of supercell. For example, the supercell $M_{m-1}VHe_n$ is composed of m-1 metals (M), one vacancy (V), and n He trapped in the vacancy. Impurity located at k-th nearest neighbor site from the V-He complex is expressed by X(k), as shown in Fig. 1. Then, $E[M_m]$ indicates cohesive energy of perfect crystal. A large simulation cell composed of 5x5x5 bcc lattice was used. The cut-off energy of plane wave was 500eV.

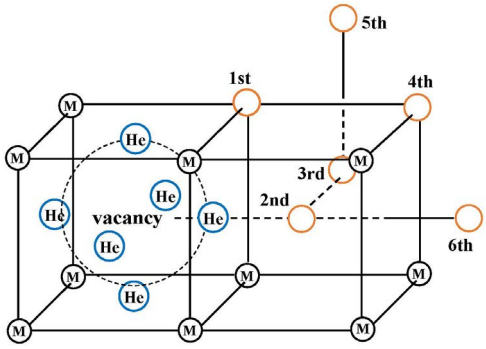

Fig. 1 Schematic view of k-th nearest neighbor site from V-He complex.

Results and discussion

We estimated binding energies of impurities Re and Cu to V-He complexes in W and Fe, respectively. The number of He atoms trapped in the vacancy is assumed to be 0, 1, and 6 in the present simulations.

According to Fig. 2, first and second nearest neighbor sites from the V-He complexes in W are energetically favorable for Re. Therefore, attractive interaction supposed to act between Re and W vacancy. Actually, Re precipitation has been reported to be observed on the inner surface of void in W specimen, which is good agreement with the present simulations. The binding energies of Re to V-He complex are almost independent of the number of He atoms trapped in the W vacancy, that is, Re does not appear to interact with He.

In the case of Cu in Fe, attractive interaction also acts between Cu and Fe vacancy, as shown in Fig. 3. The first nearest neighbor site from Fe vacancy is energetically most favorable for Cu, which consistents with the fact that Cu does not dissolve in Fe at all. However, the binding energies of Cu to V-He complex definitely depend on the number of He atoms trapped in the Fe vacancy. As the number of He atoms trapped in the Fe vacancy increases, the binding energy increases. So, there appears to be an interaction between Cu and He. However, He does not chemically bond with other elements because it is rare gas. So, we come up with a hypothesis to explain the present results. He atoms expand the Fe vacancy and create a strain filed around it. Cu only interact with the strain field and is not directly bound to the He atoms. It has been proposed that the presence of He atoms in metallic materials can be replaced by an appropriate strain field. The adequate examination for this hypothesis is an issue for the future. The difference between Re and Cu is supposed to be due to their solubility in the matrix. Re is partially soluble in W. On the contrary, Cu is completely insoluble in Fe.

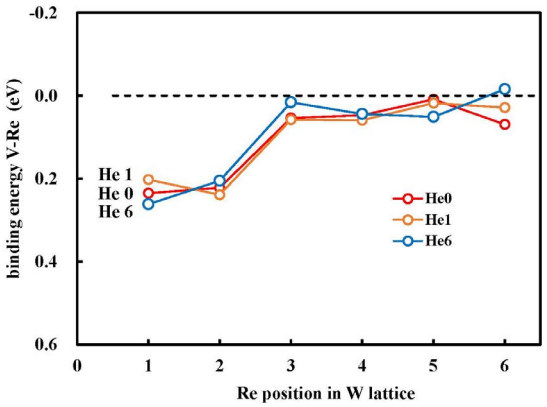

Fig. 2 Site dependence of binding energy of impurity Re to V-He complexes in W.

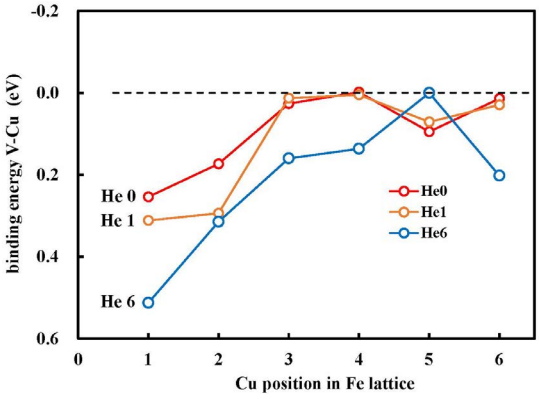

Fig. 3 Site dependence of binding energy of impurity Cu to V-He complexes in Fe.

Structure search for the T phase of silicene on the Ag(111) surface by Gaussian process regression

Yuji HAMAMOTO

Department of Precision Engineering, Graduate School of Engineering

Osaka University, Yamada-oka, Suita, Osaka 565-0871

Silicene [1], a silicon analog of graphene, has drawn growing attention from the viewpoint of a future application to ultrathin semiconductor devices. However, its charge carrier mobility is much smaller than graphene, possibly due to the nontrivial buckled structures of the honeycomb lattice, which are often observed simultaneously. Thus, identifying the buckled structures is crucial for the development of silicene-based devices. The density functional theory (DFT) is a powerful method to study the stabilities of materials, but its application to silicene has been limited to the systems whose structures can be inferred from experimental results. Consequently, there remain unidentified structures, one of which is the so-called T phase observed as less-ordered protrusions in silicene grown on Ag(111).

To investigate the stable structures of silicene on Ag(111) exhaustively and efficiently, we here adopt a structure search method based on an evolutionary algorithm and the Gaussian process regression [2]. Our results demonstrate that the method can reproduce not only the well-known stable structures but also metastable structures that have not received attention so far [3]. Especially, the $\sqrt{13} \times \sqrt{13}R19.1°$ type-I phase exhibits several metastable structures close in stability to the most stable ones as shown in Fig. 1. The metastable structures are characterized by monomer, dimer, and trimer protrusions. We have concluded that the coexistence of such metastable structures is the origin of the T phase observed experimentally.

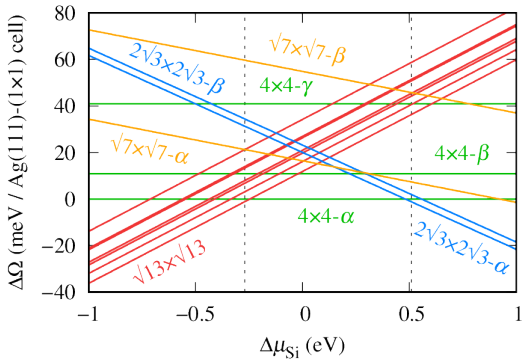

Fig. 1: Phase diagram of silicene on Ag(111).

References

[1] K. Takeda and K. Shiraishi, Phys. Rev. B **50**, 14916 (1994).

[2] M. K. Bisbo and B. Hammer, Phys. Rev. Lett. **124**, 086102 (2020).

[3] Y. Hamamoto, T. N. Pham, M. K. Bisbo, B. Hammer, and Y. Morikawa, Phys. Rev. Materials **7**, 124002 (2023).

Phase equilibrium of high entropy alloys and shape memory alloys

Yoko Yamabe-Mitarai

Frontier Science Graduate School,

The University of Tokyo, Kashiwa-no-ha, Kashiwa, Chiba 277-8561

High-entropy alloys (HEAs) comprise multiple elements with near-atomic composition and have high configurational entropy of constituent elements. HEAs have been attracted as new-generation structural and functional materials since this new paradigm was proposed in 2004 [1]. Most HEAs have a single face-center-cubic (fcc), body-center-cubic (bcc) structures, or their mixtures. Due to the limited slip system, the hexagonal-close-pack (hcp) structure is expected to be a high-temperature material. Significant solid-solution hardening is also expected for HEAs. Then, we are applying to find HEAs with hcp structure experimentally and by using DFT calculation. Phase stability of alloys was experimentally investigated, and a few alloys were found to be a hcp structure [2]. A supercell model with 128 atoms was used to indicate the solid solution phase. Special Quasirandom Structure was used to simulate random atomic position. The internal coordinates was optimized using Quantum Expresso (QE). The total energy, density of states, and electron charge density were calculated on the optimized coordinates. The results indicated that some specific bonding was very strong, and the strong bonding is expected to improve strength. This topic was presented in master's thesis and is now preparating a paper.

As the second topic, HEAs are applied for high-temperature shape memory alloys (SMAs). Several potential martensite phases are expected to be formed in HE-SMAs. The formation energy of each possible martensite phase was calculated. The results indicated that the most stable martensite phase changed depending on alloy composition.

The third topic is the adhesion behavior of the oxide layer on Ni to understand the stability of the protective oxide layer. We found that some alloying elements drastically decreased interfacial energy, improving the adhesion between Ni and the oxide layer. We submitted one paper related to this topic.

References

[1] B. Cantor et. al., A. J. B. Vincent, Mater. Sci. Eng. A, **375-377**, 213 (2004). [2] Y, Yamabe-Mitarai et. al., JALCOM, **911**, 164849 (2022)

Reaction Analysis in Solid Catalysts by DFT Calculations and Informatics

Tatsuya JOUTSUKA

Department of Materials Science and Engineering, Ehime University, 3 Bunkyo-cho, Matsuyama, Ehime 790-8577, Japan.

Center for Sustainable Energy and Environmental Engineering, Ehime University, 3 Bunkyo-cho, Matsuyama, Ehime 790-8577, Japan.

Focusing on the selectivity of zirconia-catalyzed methanol synthesis, we calculated adsorption and reaction energies to clarify the reaction mechanism. [1] In addition, polaron transfer rate constants in bulk titanium dioxide (TiO_2) and $SrTiO_3$ were calculated by the constrained density functional theory (CDFT) method. Then, the electronic structure calculation was used to elucidate the photocatalytic reaction mechanism and crystal plane selectivity in photocatalysts.

A zirconia-based solid solution catalyst $InZrO_x$ was prepared by substituting In with Zr, which has high catalytic activity. The correlation between the binding strength of the substituted elements and adsorbates (reactants, products, and intermediates) and methanol synthesis capacity was clarified. The DFT calculations employed Vienna Ab initio Simulation Package (VASP) program We conducted a Density Functional Theory (DFT) study on the formation of CH_4 on $InZrO_x$, analyzing the free energy surface and density of states (DOS). Our findings indicate a potential reaction pathway, emphasizing the transfer of the methyl group with a competitive activation barrier, aligning well with experimental data. Additionally, our study suggests that the decomposition of CH_3OH may also play a role in CH_4 production. The adsorption of a methyl group occurs exclusively on the $InZrO_x$ catalyst due to the superior overlap of DOS between the adsorbate and substrate compared to the $ZnZrO_x$ catalyst. We are now analyzing a series of solid solution catalysts in combination with machine learning. Furthermore, by integrating experimental and computational approaches, we elucidated the surface structure of CuO/t-ZrO_2. [2-3] Unlike other Cu^{2+}-containing catalysts, this catalyst is rich in highly reducible Cu^{2+} species. X-ray absorption spectroscopy and density functional theory calculations notably revealed that these Cu^{2+} species adopt a square-planar [CuO_4] configuration. Our findings suggest that these highly active [CuO_4] species are crucial in facilitating the coupling reaction.

Additionally, we calculated the polaron

transfer rate constants in bulk TiO_2 and $SrTiO_3$ (Fig. 1) using the Constrained Density Functional Theory (CDFT) method along several directions, such as the [101] direction in TiO2, with the CP2K program package. Our results show that the CDFT method provides a more accurate evaluation of the potential energy profile compared to the frequently used linear interpolation of structures for bulk TiO_2. Subsequently, we examined the $SrTiO_3$ (001) and (110) surfaces to understand polaron transfer at these surfaces. Currently, we are investigating the relationship between oxygen vacancies and electron polarons to further elucidate the photocatalytic mechanism, employing the CP2K program package.

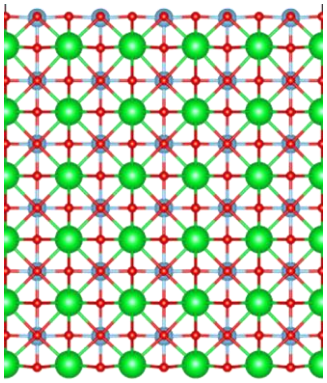

Fig. 1: Bulk $SrTiO_3$.

References

[1] Shohei Tada,* Yurika Ogura, Motohiro Sato, Akihiro Yoshida, Tetsuo Honma,e Masahiko Nishijima, Tatsuya Joutsuka,* Ryuji Kikuchi*, Phys. Chem. Chem. Phys., 26, 14037-14045 (2024).

[2] Shohei Tada,* Tatsuya Joutsuka* and Masaru Kondo,* ChemCatChem, in press.

[3] Masaru Kondo,* Tatsuya Joutsuka,* Kakeru Fujiwara, Tetsuo Honma, and Shohei Tada,* Catal. Sci. Technol., 13 (7), 2247-2254 (2023).

Materials exploration using materials informatics

Yosuke HARASHIMA
Graduate School of Science and Technology, Nara Institute of Science and Technology
Takayama-cho, Ikoma, Nara 630-0192

The 5th Strategic Energy Plan in Japan has been established, making the realization of a decarbonized society independent on fossil fuels the most crucial challenge for future development. The hydrogen energy generated from solar energy using photocatalysts (green hydrogen) is one of the promissing candidate. The purpose of this study is to establish a scheme controling impurity-induced property to improve the visible-light photocatalytic production of hydrogen, and then, to obtain novel photocatalytic compounds. We combined first-principles calculations and experiments by using informatics technique. Material searching space was determined on the basis of expert experiences. This study expands the searching space significantly by utilizing information science, thereby pioneering new research in photocatalytic material development. In particular, we construct a high-accuracy predictive by combining dynamic Monte Carlo simulation of the calcination processes with experimental data of hydrogen evolution rate (HER). This research not only addresses the energy issue with hydrogen-generating photocatalysts but also has spillover effects for carbon-neutral petrochemical synthesis from CO_2 and green hydrogen.

Performance of photocatalysts depend strongly on their calcination processes. In this study, the calcination process is explained by three features: temperature elevation speed, calcination temperature, and calcination time. Figure 1 illustrates the schematics. Products are obtained from reactants through a calcination process. This process also produces lattice defects. The HER, R, should be proportional to the amounts of products, ρ_{p}, and defects, ρ_{d}.

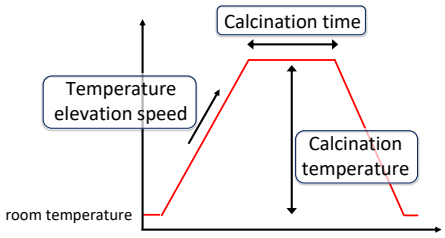

Figure 1: Schematic picture of a calcination process and its features: temperature elevation speed, calcination temperature, and calcination time.

$$R = a_{\mathrm{p}}\rho_{\mathrm{p}} + a_{\mathrm{d}}\rho_{\mathrm{d}}. \tag{1}$$

The coefficients $a_{\mathrm{p,d}}$ are determined such that the prediction reproduces experimental data of HER. $\rho_{\mathrm{p,d}}$ are calculated by dynamic Monte Carlo simulation for given calcination process.

Dynamic Monte Carlo simulation is a computational technique used to model the evolution of systems over time. The time taken for state transitions, τ, is calculated as follows.

$$\tau = -\frac{1}{W}\ln X, \tag{2}$$

where X is a random number with a range $0 < X \leq 1$, and W denotes a transition rate

$$W = \frac{1}{C}\min\left\{1, \exp\left(-\frac{\Delta E}{k_{\mathrm{B}}T}\right)\right\}. \tag{3}$$

C is a time constant, which is determined by regression. We demonstrated the scheme considering $SrTiO_3$ and optimized the calcination process to improve HER.

First principles study on the band structures of high entropy superconductors

Hidetomo USUI

Department of Applied Physics, Shimane University,

1060 Nishikawatsu-cho, Matsue, Shimane 690-8504

High-entropy (HE) compounds have attracted much attention not only from a mechanical point of view but also from the perspective of functional materials.[1,2] We have investigated the electronic structure of a HE compound MTe, which exhibits robustness of its superconductivity against external pressures[3, 4, 5]. This year, we calculated the electronic band structure of HE compounds constructed from the same or different groups in the periodic table. We used the VASP and WIEN2k packages within the PBE-exchange correlation functional with spin-orbit coupling included. We used a 2×2×2 supercell, and the site arrangement of *M* atoms is calculated using the special-quasi random structure implemented in Alloy Theoretic Automated Toolkit. The density of states of $Pb_{11}Ag_{11}Bi_{10}Se_{16}Te_{16}$ and $Ge_{10}Sn_{11}Pb_{11}Se_{16}Te_{16}$ in the rock salt structure is shown in Fig. 1. It is found that elements within the same group can strongly influence the band structure near the Fermi level ($Ge_{10}Sn_{11}Pb_{11}Se_{16}Te_{16}$). In contrast, elements from other groups tend to control the band structure near the Fermi level. The superconducting transition temperature exhibits the same behavior under pressure in (Pb,Ag,Bi)Te and (Ge,Sn,Pb)Te.[5] Therefore, our findings suggest that the electronic band structure is not a major factor in the pressure-dependent superconducting properties.

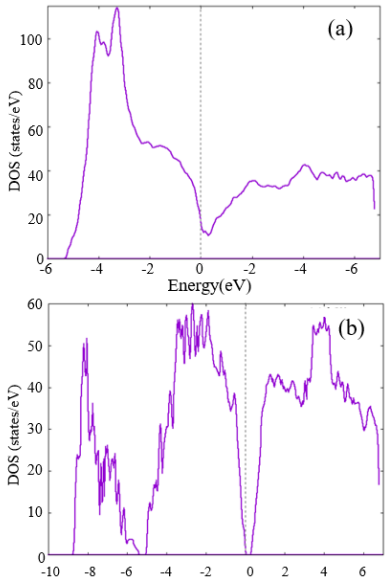

Fig. 1: The density of states of (a) $Pb_{11}Ag_{11}Bi_{10}Se_{16}Te_{16}$, (b)$Ge_{10}Sn_{11}Pb_{11}Se_{16}Te_{16}$.

References

[1] B. Jiang *et al.*, Science **371**, 830 (2021).

[2] P. Koželj *et al.*, Phys. Rev. Lett., **113,** 107001 (2014).

[3] Md R. Kasem *et al.*, Sci. Rep **12**, 7789 (2022).

[4] Y. Mizuguchi *et al.*, Mater. Today Pnys. **32**, 101019 (2023).

[5] R. Matsumoto *et al.*, J. Alloys Compd. **983**, 173906 (2024).

First-principles study of anomalous Nernst effect in topological materials

Susumu MINAMI, Takahiro SHIMADA
Department of Mechanical Engineering and Science,
Kyoto University, Nishikyo-ku, Kyoto 615-8540

The anomalous Nernst effect (ANE) is a thermoelectric (TE) effect stemming from the spontaneous magnetic order of materials, enabling the realization of flexible and efficient TE power generation modules due to the direction of the TE voltage compared to the conventional Seebeck effect [1]. Recent discoveries of topological materials that achieve a large ANE from exhibiting unique band structures (Weyl nodes, nodal lines) are promising candidate materials for TE devices based on the ANE [2]. In this research project, to elucidate the origin of the giant anomalous Nernst effect in topological magnetic materials and their characteristic electronic states, analysis of the anomalous Nernst effect and electronic states in topological magnetic materials will be conducted using first-principles calculations.

We evaluate the anomalous Nernst effect while considering in-plane lattice strain induced by epitaxial strain in the nodal-line semimetal $Co_3Sn_2S_2$. The first-principles calculations are employed the VASP package [3,4]. From the obtained Bloch states, we construct Wannier basis by using Wannier90 code [5] to evaluate transverse thermoelectric conductivity α_{xy}. The effects of the nucleus and electrons were expressed by the projector-augmented wave (PAW) method. A $24 \times 24 \times 24$ k-point mesh with the Monkhorst–Pack scheme was used for Brillouin zone sampling of the primitive cell. The generalized-gradient approximation was adopted for the exchange-correlation functional. The out-plane lattice constant and atomic configuration under each in-plane strain is optimized to satisfy the maximum force of below 0.01 eV/Å based on the conjugate gradient algorithm.

Figure 1 shows the temperature dependence of α_{xy} at several in-plane strain conditions. We find that the transverse thermoelectric conductivity α_{xy} is about 1.5 $AK^{-1}m^{-1}$ at 150 K, which is consistent with experimental results [6]. Moreover, α_{xy} reaches 2.2 $AK^{-1}m^{-1}$ with 3% in-plane compressive strain condition. We clarified that the in-plane compressive strain improves α_{xy} about 1.5 times more than no strain condition. As a future perspective, we investigate the enhancement mechanism of transverse TE conductivity α_{xy} by strain engineering for several topological magnets.

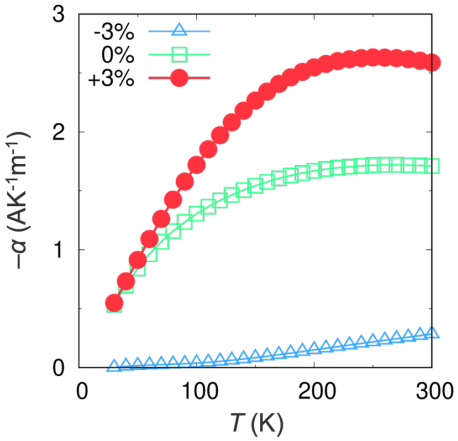

Fig. 1: Temperature dependence of transverse thermoelectric conductivity α_{xy}. Triangle, square, circle line points represent in-plane 3% tensile strain, no strain, 3% compressive strain condition, respectively.

References

[1] M. Mizuguchi and S. Nakatsuji, Sci. Tech. Adv. Mater **20**, 262 (2019).

[2] S. Nakatsuji, R. Arita, Annu. Rev. Condns. Matter Phys. **13**, 119 (2022).

[3] G. Kresse, and J. Hafner, Phys. Rev. B **47,** 558 (1993).

[4] G. Kresse, and J. Furthmüller, Phys. Rev. B **54**, 11169 (1996).

[5] G. Pizzi, et al., J. Phys.: Condens. Matter **32**, 165902 (2020).

[6] Guin, S. N. et al., Adv. Mater. **31**, 1806622 (2019).

Computational Carrier Mobility Estimation of Organic Semiconductors

Toshihiro SHIMADA

Division of Applied Chemistry, Faculty of Engineering,

Hokkaido University, Kita 13 Nishi 8, Kita-ku, Sapporo, Hokkaido 060-8628

Compared to simple p- and n-type organic field-effect transistors, it is very difficult to achieve high performance in ambipolar transistors because both HOMO–HOMO and LUMO–LUMO interactions in the crystal must be large and multidimensional. We synthesized some organic molecules with fused aromatic rings, determined the crystal structures experimentally, and calculated electronic structure including the interaction between p-electron systems between the molecules. We used VASP for the first principle band strucutre calculation using ISSP-B and -C systems for the computation. Theoretical calculations using the obtained molecular arrangement suggested that there are two-dimensional interactions for both HOMO–HOMO and LUMO–LUMO.[1]

From the calculation of TPCPA and TPDPP (shown in Fig. 1), it was found that TPCPA type 1 crystal had nearly one electronic structure for electrons, while TPCPA type 2 and TPDPP had two dimensional structures both for electrons and holes, that shows ambipolar characteristics. The experimental mesurement of FET was successfully performed for TPDPP, resulting in the confirmation of ambipolar characteristics.

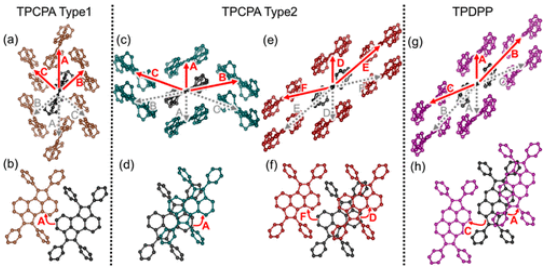

Fig. 1: Crystal structure and intermolecular interactions (arrows with A,B,C) of molecules TPCPA (two polymorphisms in crystal structure) and TPDPP. The molecular interactions were estimated from calculations using the experimentally determined crystal structures.

References

[1] H. Tanoguchi, T. Yuki, S. Yokokura, T. Yanase, J. Mingoo, H. Ito, T. Nagahama, T. Shimada, ACS Appl. Electron. Mater. 5, 6626 (2023).

[2] T. Yuki, S. Yokokura, M. Jin, H. Waizumi, S. Yokokura, T. Nagahama, T. Shimada, Cryst. Growth Des. 24, 1849 (2024).

Calculation of Formation Energies of $P_2Ir_2O_7$ and Related Compouds by DFT in relation to Thin Film Growth Experiments

Toshihiro SHIMADA

Division of Applied Chemistry, Faculty of Engineering,

Hokkaido University, Kita 13 Nishi 8, Kita-ku, Sapporo, Hokkaido 060-8628

Topological materials including Weyl semimetals (WSM) are gathering much attention recently from the expectation of possible spintronics applications. We are growing epitaxial thin films of WSM, such as pyrochlore $Pr_2Ir_2O_7$ (PIO) by molecular beam epitaxy. From the experimental structural evaluation and physical property measurement of the thin films, we consider impurity phases are sometimes included in the sample depending on the growth conditions. In order to understand the mechanism, we conducted DFT calculation of the related materials (IrO_2, PrO_2, Pr_2O_3, Pe_3IrO_7, PIO, PIO_WB(Weberite structure; *Ccmm*), PIO_DF(defect fluorite structure; $Fm\bar{3}m$) using ISSP supercomputer system. The crystal structures are shown in Fig. 1 adopted from Ref [1]. We used VASP with GGA-PBA with the cut-off Energy 650eV. The functional for Pr was Pr_3[2].

.

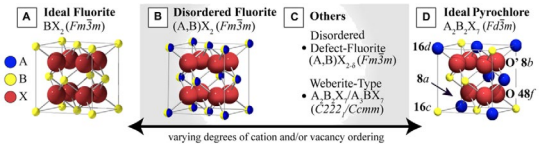

Fig. 1: Materials considered [1]

The result is shown in Fig. 2.

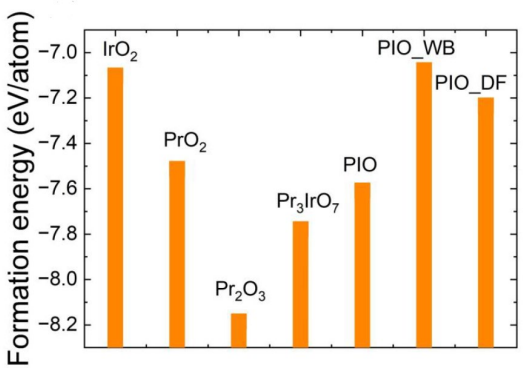

Fig.2: Formation energies from DFT.

The result is useful to optimize the thin film growth conditions for PIO.

References

[1] J.L. Wardini et al., Front. Chem. 9, 743025 (2021).

[2] G. Lan et al., Acta Mater. 91, 304 (2015).

Calculation of chemical shift of X-ray photoelectron binding energy of hydrogen-containing functional groups generated on fluoropolymer surface

Yuji OHKUBO, Misa NISHINO, and Kouji INAGAKI

Graduate School of Engineering, Osaka University, 2-1 Yamadaoka Suita, Osaka 565-0871

Polytetrafluoroethylene (PTFE) has both much low relative dielectric constant and dielectric loss tangent, so it is considered as a suitable dielectric substrate of high-frequency printed wiring boards. However, PTFE has low adhesion property, so adhering PTFE to Cu is difficult. We have achieved generation of oxygen-containing functional groups and adhesion strength of 0.98 N/mm between PTFE and Cu when PTFE was He-plasma-treated at over 200℃ under atmospheric pressure[1]. However, it is difficult to experimentally measure the exact value of the chemical shift in the X-ray photoelectron spectroscopy (XPS) spectra of the functional groups formed on the PTFE surface. Therefore, it is necessary to determine the exact values of chemical shifts of the functional groups formed on the plasma-treated PTFE surface using first-principles calculations to accurately identify the functional groups formed on the PTFE surface. In this study, we calculated the C1s core level binding energies of normal-chain-type molecules comprising C, F, O, and H. We deconvoluted the experimentally obtained C1s-XPS spectra using the calculated values to identify the chemical species generated on plasma-treated PTFE surfaces.

The C1s core level binding energy was calculated by the Δself-consistent field (ΔSCF) method. The energy difference between the ground state molecule and the molecule with a core hole was also calculated by this method using the Gaussian 09 software package. The geometry was optimized using the Hartree–Fock method, and ccpVDZ was used as the basis function. The SCF calculation of a molecule with a core hole was converged by direct minimization. Fluorine-based molecules were used as the computational models of polymers. These molecules were cut into small molecules from the –(CF_2–CF_2)*n*– chain, a component of PTFE. As the model of the as-received PTFE, CF_3–CF_2–CF_2–CF_2–CF_3 was used. CF_3–CF_2–CF_2–O–CF_3, CF_3–CF_2–O–C(=O)–CF_2–CF_3, CF_3–CF_2–CFOH–CF_2 –CF_3, CF_3–CF_2–C(=O)–CF_2–CF_3, and CF_3–CF_2–CF=CF–CF_3 were used as the models of oxygen-containing functional groups generated by plasma treatment. Furthermore, the molecules with F substituted by H were also calculated. It is difficult to accurately calculate the absolute experimental

C1s core level binding energies, but the relative C1s core level binding energies in various chemical environments can be well reproduced by ΔSCF calculations[2]. Therefore, we shift the calculated C1s core level determined by taking the energy difference between the experimentally observed C1s binding energy (Eexp) of 292.5 eV[3] in –(CF_2–CF_2)n– and the calculated value (EΔSCF) of 299.97 eV. To compare with experimental values, we subtracted Δ (7.47 eV) from the calculated C1s binding energies of all chemical species investigated in this study. The calculation error in this study originates from the incompleteness of the basis set, the neglect of the electron correlation energy in the Hartree–Fock approximation, the vacuum surrounding the model molecules, and the approximation of the model molecules as small molecules. The constant shift removes the error from the vacuum surrounding the model molecules.

Table 1 shows the calculated C1s core level binding energies of molecules with the oxygen-containing functional groups in the CF_2– and CH_2– chains. **Fig. 1** shows the deconvolution results of the C1s-XPS spectra of the plasma treated PTFE surfaces using the calculated values. The large peak near 286.4 eV was not reproduced using only these peaks because the smallest C1s core level binding energy ofmolecules with the oxygen-containing functional group in the CF_2– chain was 289.3 eV. Therefore, by adding the calculated values of the functional group in the CH_2– chain, we were able to reproduce the peak near 286.4 eV. This result indicated that the F atoms were substituted by the H atoms on the PTFE surface by plasma treatment.

Table. 1. Calculated C1s core level binding energies of molecules with oxygen-containing functional groups in the CF_2– and CH_2– chains.

No.	Molecule	E_{cal} [eV]
①	CF_3–CF_2–$\underline{C}F_2$–O–CF_3	294.1
②	CF_3–CF_2–$\underline{C}F_2$–CF_2–CF_3	292.5
③	CF_3–CF_2–O–$\underline{C}$(=O)–CF_2–CF_3	291.9
④	CF_3–CF_2–$\underline{C}$FOH–CF_2–CF_3	291.4
⑤	CF_3–$\underline{C}F$–(CF–(CF_3)$_2$)–CF_3 (Crosslinking)	290.7
⑥	CF_3–CF_2–$\underline{C}$(=O)–CF_2–CF_3	290.4
⑦	CF_3–CF_2–$\underline{C}F$=CF–CF_3	289.3
⑧	CH_3–CH_2–O–$\underline{C}$(=O)–CH_2–CH_3	289.3
⑨	CH_3–CH_2–$\underline{C}$(=O)–CH_2–CH_3	287.6
⑩	CH_3–CH_2–$\underline{C}H_2$–O–CH_3	286.2
⑪	CH_3–CH_2–$\underline{C}$HOH–CH_2–CH_3	286.1
⑫	CH_3–CH_2–$\underline{C}H_2$–CH_2–CH_3	284.6
⑬	CH_3–$\underline{C}H$–(CH–(CH_3)$_2$)–CH_3 (Crosslinking)	284.5
⑭	CH_3–CH_2–$\underline{C}H$=CH–CH_3	284.3

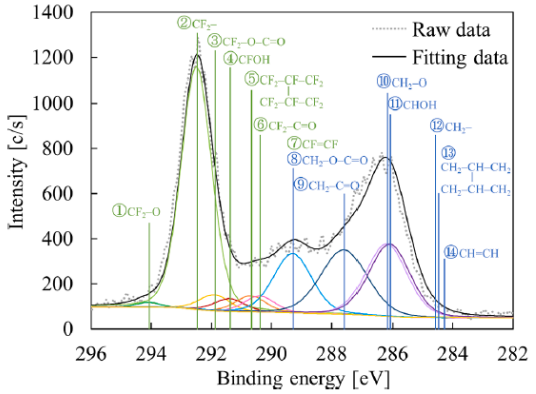

Fig. 1. Deconvolution results of C1s-XPS spectra of plasma treated PTFE surfaces using oxygen containing functional groups only in the CF_2– and CH_2– chains.

References

[1] M. Nishino et al., *RSC adv.*, **13** (2023) 25895–25903.

[2] E. A. Hoffmann et al., *J. Polym. Sci. Part A Polym. Chem.*, 42 (2004) 551–556.

[3] G. Beamson et al., *J. Chem. Educ.*, **70** (1993) A25.

Theoretical study of work function and band gap of double-perovskite

Kazume NISHIDATE
Graduate School of Science and Engineering, Iwate University
4-3-5 Ueda, Morioka, Iwate, 020-8551

Double perovskite Ba_2PrBiO_6 exhibits photo catalytic activity in the visible light range with the observed optical band gap of ∼1.0 eV. On the other hand, density functional theory (DFT) calculations predict a larger bulk band gap of 2.0 eV even with the standard Perdew-Burke-Ernzerhof (PBE) functional, which is known to underestimate the band gap of semiconductors. Much larger bulk band gap of 3.13 eV is predicted with a hybrid functional treatment for the exchange correlation, which generally gives better descriptions for them. This discrepancy between experiment and theory implies the presence of unknown mechanism which effectively reduces the band gap of Ba_2PrBiO_6 and thereby gains the sensitivity to the visible light. The first finding is that the surface band gaps of Ba_2PrBiO_6 calculated using an appropriate hybrid functional are smaller than the bulk band gaps and are 2.49 eV and 2.85 eV for the Pr-Bi and Ba-O polar surfaces, respectively. We also find that work function is quite sensitive to the surface structures and its accurate calculations are essential to show that the reduction and oxidation levels are fit to the gap region. When a substitutional defect Pr_{Bi}, in which Bi is substituted by Pr, is introduced into the Pr-Bi polar surface, surface band gap is further reduced to 0.93 eV, being very close to the experimental value. For the Ba-O polar surface, similar reduction to 1.59 eV is found but not substantial as compared to the Pr-Bi polar surface. These narrow surface band gaps may be the origin of the photo activity of Ba_2PrBiO_6 in the visible light region.

We also performed Born-Oppenheimer molecular dynamics simulations to clarify the reactivity of the polar surfaces to water. Adsorption of the second H_2O molecule generates two other hydroxyl groups with the help of the one oxygen atom at the subsurface. No more hydroxyl group is formed by the adsorption of the third H_2O molecule. On the other hand, H_2O molecule adsorbed on the Pr-Bi surface can be diffused on the surface. When two H_2O molecules were successively placed on the Pr-Bi surface, only the first H_2O molecule was adsorbed. This adsorption generates two hydroxyl groups as in the Ba-O case. However, the second H_2O molecule is not decomposed into the hydroxyl group but makes a weak bond with the surface (stage II). Then the H_2O molecule starts to diffuse on the surface (stage III). The different behaviors against the adsorptions may originate in the exposed oxygen atoms.

References

[1] K. Nishidate, M. Matsukawa, A. Matsushit, Y, Li, D. C. Roy, and M. Hasegawa,: Surf. and Int. **24**, 103914 (2024).

[2] Y. Li and K. Nishidate: Int. J. Hydro. Eng. **51**, 1471 (2024) .

Unique patterns in simulated scanning tunneling microscopy images of graphene nanoribbons

Junhuan LI, Kenta ARIMA

Graduate School of Engineering, Osaka University, Yamada-oka, Suita, Osaka 565-0871

Previously, we successfully validated the presence of a rectangular-like lattice in nanographene observed experimentally by simulating scanning tunneling microscopy (STM) images of armchair-edged graphene nanoribbons (AGNRs) [1]. However, the origin of this unique lattice remains to be explored.

Calculations were performed by STATE (Simulation Tool for Atom TEchnology) package. The band structures of 39-AGNR (where 39 is the width measured by the number of rows of carbon atoms across the AGNR) was shown in Figure 1.

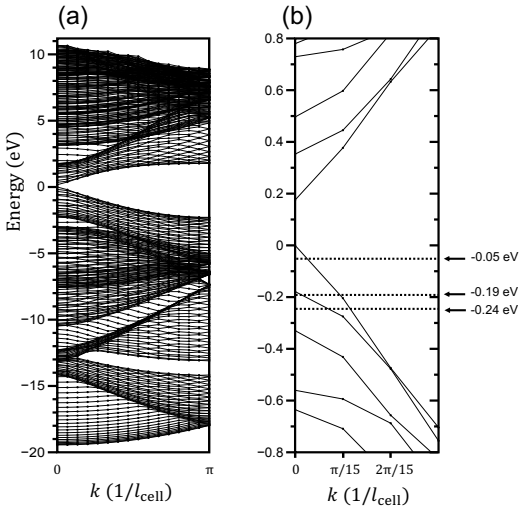

Fig. 1: Band structures of 39-AGNR.

Based on Figure 1b, we selected three different sample biases (represented by three dotted lines and arrows) for calculating the STM images. The larger the absolute value of the sample bias, the more eigenvalues in the band structure are included in the calculation. As shown in Figure 2, only the calculation results for the smallest sample voltage reveal the rectangular-like lattice [2].

This work has been performed on System B of the Supercomputer Center, the Institute for Solid State Physics, the University of Tokyo.

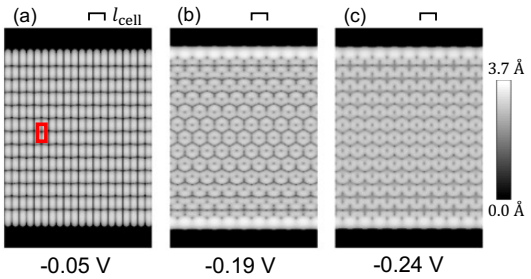

Fig. 2: Simulated STM images of 39-AGNR at different sample biases.

References

[1] J. Li et al., Phys. Rev. B **103**, 245433 (2021).

[2] J. Li et al., Phys. Rev. Res. **6**, 013252 (2024).

Acceleration of DFT calculation code by using GPU

Masao OBATA

Institute of Science and Engineering, Kanazawa University, Kanazawa, Ishikawa 920-1192

Electronic structure calculations based on density functional theory (DFT) and the Kohn-Sham (KS) approach, promising tools for analyzing and predicting the physical properties of materials, are widely used in various fields of material science. Accelerating the DFT code is crucial for promoting such investigation and will expand the application range of DFT calculations. For the speedup of DFT calculation, we considered utilizing GPUs and verified the efficiency of GPU in DFT calculation. Since the data transfer bottleneck between CPU and GPU is a well-known issue, we introduced a simple strategy to minimize data transfer called data GPUization [1]. In the data GPUization concept, we focused on large amounts of data in the DFT calculation, such as wave functions. We implemented GPU calculations in all the operations that handle such large data in the iterative procedure of DFT. As a result, large data transfers are no longer necessary in an iterative procedure. The concept of data GPUization focuses on the data size of variables as well as computational cost. Such a concept effectively reduces data transfers, especially in iterative calculations.

In our research, we implemented GPU calculation in our homemade DFT code, which employed a plane-wave basis with an ultrasoft pseudopotential scheme. The implementation was done using OpenACC and the GPU-accelerated math library provided by NVIDIA HPC SDK. We tested our implementation using ISSP System C (CPU: AMD EMPY 7763, GPU: NVIDIA A100) and compared the computational time with and without GPUs. The performance ratio between 1 CPU core and 1 GPU is around 247 (495 in the case of Tensor Core usage). We used a magnetic 224 atoms (5264 KS orbitals) system for the benchmark. The computational time in one DFT (Car-Parrinello) step was significantly reduced from 5206s in CPU to 49s in GPU without data GPUization. However, the transferred data size was 137GB in one DFT step, accounting for 60% of computational time. The computational time of the data GPUization version was 15s.

Although it was confirmed that using GPUs based on data GPUization drastically accelerates calculations, data GPUization requires large data to be constantly maintained in GPU memory; therefore, one of the future issues is overcoming GPU memory depletion.

References

[1] C. Pardede, M. Obata et al., proceedings of CCP 2023, accepted.

Leakage of surface/interfacial electrons of topological insulators

Ken-ichi Shudo

Fac. Sci/Eng, Yokohama Nat'l Univ.

Tokiwadai 79-5, Hodogaya-ku, Yokohama 240-8501

We have measured the electronic states of Bi_2Se_3, a typical topological insulator, by means of metastable atom electron spectroscopy (MAES), which exclusively detects the leak of electrons from a solid surface into the vacuum. An experimental result is shown in Fig.1. To interpret the spectra, we calculated a slab system of the material, using Vienna ab initio simulation package (VASP). The results of the calculated dispersion showed inconsistency due to the complicated band structure. The band shape depends on the approximation method or the LDA/GGE density functionals. We now measure MAES finely with varied conditions, and will compare them with the calculational results.

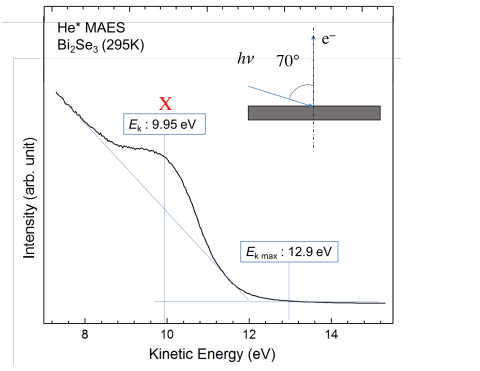

Fig. 1 MAES of Bi_2Se_3 with He* irradiation.

At the same time, we perform calculations of electronic states to elucidate the spin-dependent band structure of metal-organic framework (MOF) of metal-injected porphyrin-derivatives (the project continues from year 2022). At the pore of the porphyrin-core Fe atom is introduced, and the local spin moment remains. The spin state is correlated the linkage-legend (Cu) of MOF. The computational results account for our experimental photo-absorption spectra in magnetic circular dichroism (MCD). However, we noticed that there is intermixing of orbital angular moment and spin angular moment, and found inconsistency between the experimants and calculation in the work-function of the two-dimensional Fe-dosed porphyrin MOF layer. Currently the details are examined still.

Our group has started analysis of bend-symmetry of single crystal of pure Ti, on which optical higher harmonic generation occurs. We assume now that the asymmetry of the optical results originates from the bond strength of the fermi surface in terms of mechanical asymmetry.

Renormalized charge-spin fluctuations from first principles

Ryosuke AKASHI
National Institutes for Quantum Science and Technology

The first-principles calculation for superconductors have recently much advanced with efficient numerical implementations of the first-principles Eliashberg theory [1, 2, 3] and density functional theory for the superconductors (SCDFT [4, 5, 6]). For the phonon-mediated superconductors, those methods enabled non-empirical evaluation of the screened Coulomb interaction, which strongly suppresses the Cooper pairing, and accurate estimation of the resulting transition temperature $T_{\rm c}$. Further extensions of the framework have also been gradually conducted, toward materials regime with intermediately strong correlations.

A representative correlation effect that may become more appreciable in the regime is the spin-fluctuation effect. Recently, Essenberger and colleagues [7] have proposed a method to include the spin fluctuations in the first-principles superconducting calculation with the newly developed exchange-correlation kernel for the SCDFT. We have examined the accuracy in 3d and 4d elemental metals, V and Nb [8]. For those systems, we found that the calculations without the spin fluctuation yield values of $T_{\rm c}$ larger than the experimental values. The spin fluctuation included by the Essenberger formalism suppresses those too much: Although the deviation from the experimental observations is mitigated, the resulting values are too low. This oversuppressing phenomenon is thought to be due to the breakdown of the original formalism, which is based on the adiabatic local density approximation and presumably overestimate the strength of the fluctuation in the vicinity of the magnetic phase transition.

In this project, we have attempted to "renormalize" the strength of the spin fluctuation using the formally exact adiabatic connection formula [9]

$$E_{\rm xc} = E_{\rm x} - \frac{1}{2}\int_0^1 d\lambda \int \frac{d\omega}{2\pi} dr dr' \times \frac{\chi_\lambda[n](r,r';i\omega) - \chi_{\lambda=0}[n](r,r';i\omega)}{|\mathbf{r}-\mathbf{r}'|}. \quad (1)$$

Here, χ_λ denotes the response function for the ground state of the Hamiltonian with interaction scaled by λ: $H = H_0 + \lambda U$, where the external potential in H_0 is tuned so that the ground-state charge density n is constant against λ. The functional derivative with respect to the charge and spin densities gives us exact equations for the spin and charge susceptibilities [10].

We have tested a one-shot method, where we insert the ALDA susceptibilities in the right hand side of the derived equations and evaluated them once. At this point, however, the numerical calculations suffer from instability due to multiple Green's functions entering the equations. Efficient and reliable calculation of the formula is to be pursued in later projects.

We also explored electronic structure in nearly uniform electron model [11]. We analyzed interactions of three plane-wave branches in this model, which occur at linear regions formed by the intersections of the Bragg planes. We found that the band critical lines and Dirac nodal lines are generally formed in the close vicinity of those intersection lines.

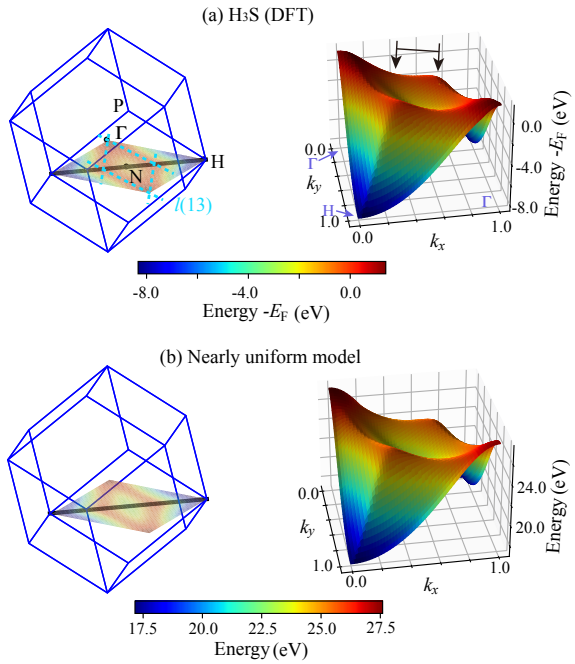

Figure 1: Structure of the valence band that is responsible for the divergence of DOS in H_3S. (a) Result with the first-principles calculation. Arrows on the right indicate the flat region that has dominant contribution to the total DOS. (b) Result with the nearly uniform electron model, with only three model parameters. See Ref. [11] for more details.

Further, we pointed out that the diverging van Hove singularity in a high-temperature superconductor H_3S is well explained by this mechanism. Figure 1(a) shows the energy eigenvalues of the band that is responsible for the DOS singularity, calculated from first principles. In the left panel, we depict the position of the intersection that is the origin of the linearly extended band critical point. By tuning the interaction matrix elements at this intersection, we successfully reproduced the band structure by the nearly uniform model as shown in panel (b). This result clarifies that the apparently anomalous electronic structure in H_3S is actually explained as an example of the general nearly uniform electron theory. The first-principles calculations were performed using Quantum Espresso [12] with norm conserving pseudopotentials from *Pseudo dojo* [13].

References

[1] G. M. Eliashberg, Zh. Eksp. Teor. Fiz. **38**, (1960) 966.

[2] A. B. Migdal, Zh. Eksp. Teor. Fiz. **34**, (1958) 1438.

[3] A. Sanna, J. A. Flores-Livas, A. Davydov, G. Profeta, K. Dewhurst, S. Sharma, and E. K. U. Gross, J. Phys. Soc. Jpn. **87**, (2018) 041012.

[4] M. Lüders, *et al.*, Phys. Rev. B **72** (2005) 024545.

[5] M. A. L. Marques, *et al.*, Phys. Rev. B **72** (2005) 024546.

[6] A. Sanna, C. Pellegrini, and E. K. U. Gross, Phys. Rev. Lett. **125**, (2020) 057001

[7] F. Essenberger *et al.*, Phys. Rev. B **90** (2014) 214504.

[8] K. Tsutsumi, Y. Hizume *et al.*, Phys. Rev. B **102**, (2020) 214515.

[9] D. C. Langreth and J. P. Perdew, Solid State Commun. 17, (1975) 1425.

[10] Y. Hizume, unpublished.

[11] R. Akashi, arXiv:2306.04238.

[12] P. Giannozzi *et al.*, J. Phys. Condens. Matter **29**, (2017) 465901.

[13] G. Pizzi *et al.*, J. Phys. Condens. Matter **32**, (2020) 165902.

Theoretical investigation for systemataising surface diradical

Kohei TADA[1, *]

Department of Materials Engineering Science, Graduate School of Engineering Science, Osaka University, Toyonaka, Osaka 560-8531, Japan

Diradical state is that with two open-shell electrons in pseudo-degenerate orbitals. The state is important for understanding the physical properties originating from strongly correlated intra-/intermolecular electrons [1]. Strongly correlated electrons are the origin of various material functions; hence, novel molecular function will be achieved by immobilising the diradical molecules on surfaces. However, the diradical state of surface-adsorbed molecules (= surface diradical) has not been well studied due to the lack of theoretical and experimental techniques.

In this project, a systematic investigation was performed on the interaction of s- and p-diradical molecules with alkaline-earth metal oxide surfaces. Diradical molecule models with s-orbitals were Au, Ag and Cu dimers with inter-atomic distance where the s-orbitals are pseudo-degenerating. This system was investigated using system B, ohtaka. For the p-orbital diradicals, a real diradical molecule, p-benzyne, was employed. This calculation was performed on system C, kugui. Used programme was VASP. Correction based on the approximated spin projection method to density functional theory calculation with plane-wave basis (AP-DFT/plane-wave) [2,3], which is a recently developed scheme, was used for the analysis of the diradical states.

Diradical character, *y*, is a feature value for diradical molecules, and can be utilised to *in silico* design [1]. The effect of surface-adsorption on diradical character (Δy) can be classified into three effects [4], as shown in Fig. 1: namely, the effect of molecular distortion caused by adsorption (Δy_{dis}), the effect of inter-molecular interactions (Δy_{coh}), and the effect of molecule-surface interaction (Δy_{surf}). Table 1 summarises Δy values of the p-benzyne adsorption models. Details of the calculated models can be found in the cited article [4]. The absolute values of Δy_{surf} are the largest among three effects. The reason why the *y* values of p-benzyne is reduced by the molecule-surface interaction is as following:

(1) Although the computational model is constructed as a physically adsorption of p-benzyne, a slight orbital correlation between the surface ions and the molecule occurs. This causes delocalisation of singly occupied C sp2 orbital to the aromatic ring.

(2) Intramolecular charge polarisation is induced by the charges of the surface ions, and

the spin density is reduced due to the enhanced contribution of the closed-shell resonance structure.

The present study explicitly shows that diradical character of real diradical molecule can be modulated even in weakly adsorbed states, such as physisorption. The results were published from *Physical Chemistry Chemical Physics*, and the paper was selected as the front cover and hot article [4].

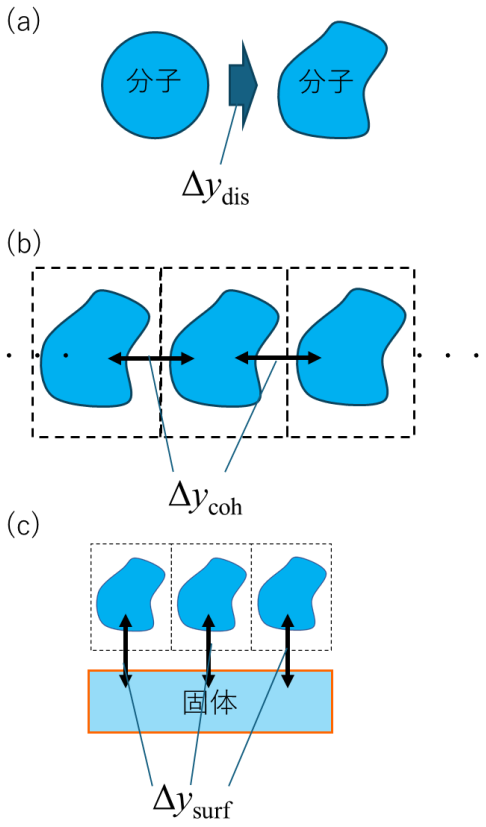

Fig. 1: Schematic views of Δy_{dis} (a), Δy_{coh} (b), and Δy_{surf} (c).

Table 1: Estimated (Δy), (Δy_{dis}), (Δy_{coh}), and (Δy_{surf}) of p-benzyne adsorption models [4]. Negative value indicates the y value of p-benzyne is reduced by the adsorption.

Model	Δy	Δy_{dis}	Δy_{coh}	Δy_{surf}
A	–0.8	+0.2	+0.8	–1.8
B	–5.7	–0.1	–0.6	–5.0
C	–6.0	–0.8	+0.6	–5.7
D	–11.1	–0.7	+0.6	–11.0
E	–5.5	–1.8	+0.6	–4.4

References

[1] T. Stuyver, B. Chen, T. Zeng, P. Geerlings, F. De Proft, R. Hoffinann, Chem. Rev. **119**, 11291 (2019).

[2] K. Tada, H. Ozaki, K. Fujimaru, Y. Kitagawa, T. Kawakami, M. Okumura, Phys. Chem. Chem. Phys. **23**, 25024 (2021).

[3] K. Tada, H. Koga, M. Okumura, S. Tanaka, Chem. Phys. Lett. **701**, 103 (2018).

[4] K. Tada, T. Kawakami, Y. Hinuma, Phys. Chem. Chem. Phys. **25**, 29424 (2023)

* Previous affiliation is National Institute of Advanced Industrial Science and Technology (AIST).

Photoexcited Carrier Dynamics in the CO_2 Photoreduction on Monoclinic-ZrO_2 Surface

Keisuke Hara and Yasuo Izumi

Graduate School of Science,

Chiba University, Yayoi-cho, Inage-ku, Chiba 263-8522

In this report, we evaluated the contribution of photoexcited electrons in the CO_2 photoreduction process occurred on the monoclinic-ZrO_2 photocatalytic surfaces. While exploring the reaction pathway through the ground state has already been done [1], the clarification of the role of excited electrons is indispensable because it directly describes the essence of photocatalytic process.

Although the final steps in the reaction mechanism normally differ among the catalysts, the onset steps often follow the mechanism in which CO_2 adsorbs on the surface, and photoexcited electrons are injected into CO_2 from the substrate. In these early stages of photocatalytic reaction pathway, the reaction can be classified into two types: Type I where excited electrons are injected into the adsorbed CO_2, forming a CO_2 anion radical and Type II where proton addition first takes place, forming an OC^+OH species. Therefore, in ZrO_2, which exhibits higher photocatalytic activity in the CO_2 reduction compared to transition metal oxides, this study elucidates whether Type I or Type II occurs predominantly over ZrO_2 photocatalyst.

Density Functional Theory (DFT) calculations were performed using the Vienna Ab initio Simulation Package (VASP) version 6.4.1.The projector-augmented wave method was employed at the DFT-D3 level to incorporate the van der Waals interaction. The generalized gradient approximation RPBE exchange-correlation functional was used for series of calculations including AIMD, with the cutoff set at 500 eV and adding Hubbard *U* parameter (4.0 eV for Zr). To further track the behavior of the photoexcited electrons, we conducted ab initio Non-Adiabatic Molecular Dynamics (NAMD) calculations. NAMD calculations are based on time-dependent Kohn-Sham theory combined with a fewest-switches surface hopping algorithm in the classical Path approximation [2, 3].

A series of calculations confirmed that adsorbed CO_2 on the pristine surface followed a Type II reaction pathway. In clear contrast, when CO_2 adsorbed at oxygen vacancies, the reaction step followed a Type I pathway. When CO_2 adsorbed at the oxygen vacancy, it bent upon adsorption, reducing the energy level of LUMO and LUMO+1 toward lower direction compared to straight configuration. The LUMO+1 level of bent CO_2 lay just below the Conduction Band Minimum of ZrO_2 and, hence, the excited

electrons were likely to relax to the LUMO+1 level. As the result, within 500 fs, 55% of the photoexcited electrons were injected into the LUMO+1 level of CO_2 after the photoexcitation (Figure 1, the line of CO_2 LUMO+1).

In contrast, there are the energy levels of CO_2 adsorbed on the pristine surface (not shown). The energy of these levels negligibly changed with the initial 500 fs. Even when photoexcited electrons were injected, these electrons quickly relaxed to the lower energy levels of ZrO_2 conduction band; the excited electrons could not be trapped for a long time. Thus, the ability of CO_2 to trap the excited electrons within its molecular orbital(s) was responsible for the formation of CO_2 anion radicals.

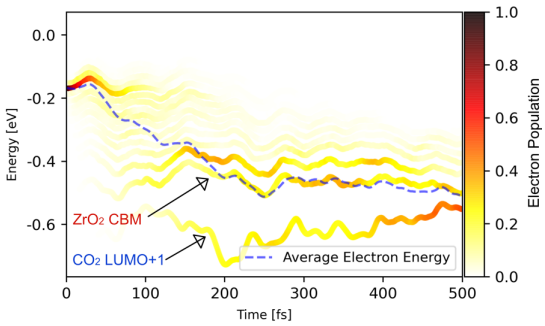

Figure 1. Time course of the relaxation of excited electrons in energy domain. The color strips indicate the normalized electron distribution at each energy state, and the blue dotted line represents the averaged electron energy.

As a future challenge, it is necessary to perform similar calculations on the other typical transition metal oxides, e.g. TiO_2 and In_2O_3, for photocatalyst to elucidate how the initial stages of the CO_2 photoreduction reaction impact on the overall photocatalytic reaction. Furthermore, it is important to clarify whether the rate of electron injection into the molecular orbitals of CO_2 dominates the reduction activity.

References

[1] Hara, K., Nozaki, M., Hirayama, R., Ishi, R., Niki, K., Izumi, Y., *J. Phys. Chem. C,* 2023, 127, 4, 1776–1788

[2] Akimov, A.V., Prezhdo, O.V., *J. Chem. Theory Comput.* 2013, 9(11), 4959–4972.

[3] Zheng, Q., Chu, W., Zhao C, *et al*., *WIREs Comput Mol Sci*. 2019, 9, e1411.

Ab initio path-integral molecular dynamics calculation of high pressure phases of ice

Jun TSUCHIYA
Geodynamics Research Center, Ehime University
Bunkyo-cho, Matsuyama, Ehime 790-8577

Determining the structures and physicochemical properties of water ice (H_2O) is fundamental across various scientific disciplines like physics, chemistry, earth and planetary sciences. Although numerous experimental and theoretical studies have been performed on the twenty known crystalline polymorphs of ice, their physical and chemical properties are not yet fully understood. A key challenge lies in the elusive nature of hydrogen, the lightest atom, with its extreme mobility and significant quantum effects posing difficulties for the experimental and theoretical investigations.

At high pressures, the behavior of ice becomes particularly complex. Previous studies indicate that in the ice VII to ice X transition, hydrogen shifts from a static to dynamically disordered state, eventually reaching symmetric hydrogen bonding states. In dynamically disordered hydrogen state, hydrogen atoms oscillate between two minima between oxygen atoms due to thermal and quantum vibrational effects. Recently, we have begun to study the structural, elastic, and vibrational properties of the high-pressure phases ice using ab initio path integral molecular dynamics (PIMD) calculations, in order to clarify the nuclear quantum effects (NQEs) on these properties (Figure 1) [1] .

The radial distribution function (RDF) of ice VII under pressure highlights the enhanced appearance of dynamically disordered hydrogen states at lower pressures in PIMD than in AIMD due to NQEs. Furthermore, a comparison of PIMD and AIMD calculations under similar conditions reveals the significant influence of NQEs on the elastic constants. At the transition from static to dynamically disordered hydrogen states, the elastic constants increase non-linearly at room temperature and high pressure around 40 GPa under the influence of NQEs. We found that the NQEs contribute significantly to the increase in the elastic constants of the dynamically disordered phases (about 20% at 300 K and 70 GPa). This study shows that NQEs have a significant influence on macroscopic properties such as elasticity even at room temperature.

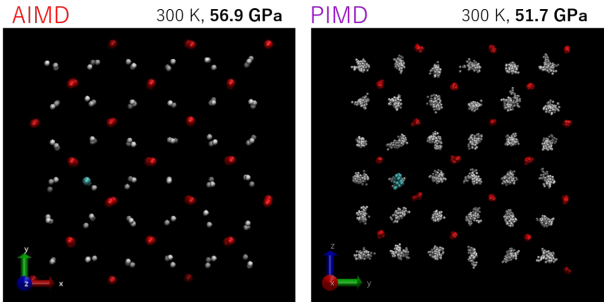

Figure 1: The snapshots of the AIMD (left) and PIMD (right) simulation of ice VII at high pressure condition.

References

[1] J. Tsuchiya, M. Shiga, S. Tsuneyuki, E.C. Thompson, preprint [arXiv:2307.14214].

First-principles study of electron interactions in transiton metal oxides

Hirofumi Sakakibara

Advanced Mechanical and Electronic System Research Center(AMES), Faculty of Engineering, Tottori University, 4-10 Koyama-cho, Tottori, Tottori 680-8552, Japan

In the history of condensed matter physics, one of the biggest topics is about cuprate high-T_c superconductors. Several theoretical studies have shown that the cuprates have ideal electronic structure for superconductivity triggered by spin-fluctuation and/or Mott physics. Theoretically, the cuprates may be described by a two-dimensional single-orbital Hubbard model on the half-filled square lattice, and this situation enhances *d*-wave superconductivity. Here, the term of the Hubbard model means a model that only onsite interaction U and the hopping integrals between the nearest neighbor sites are considered. The reason why the cuprates are recognized as ideal is that U/t value, a measure of electron correlation, is almost optimized for T_c. This implies that there are few rooms for improvement for materials described by single-orbital Hubbard models.

However, bilayer Hubbard models are theoretically investigated as candidates that go beyond the single orbital Hubbard model [1]. In bilayer models, the key value is the strong interlayer coupling $t_\perp$ and the Heisenberg exchange interaction $J{\sim}4t_\perp^2/U$. Namely, the Cooper pair is formed between different layers. Nakata et al. predicted a possibility that strong $t_\perp$ and paring is realized by the $d_{3z^2-r^2}$ orbitals spread along interlayer direction in a Ruddlesden-popper type bilayer nickelate $La_3Ni_2O_7$ [2]. In 2023, Sun et al. have reported that $La_3Ni_2O_7$ exhibit superconductivity with $T_c \sim 80$ K after structural transition under pressure of $P = 10{\sim}20$ GPa [3]. Inspired by these theory and experiment, we have started several theoretical works and collaborations between theoretical-experimental investigation.

We have modeled the electronic structure of $La_3Ni_2O_7$ using a combination between a first-principles calculation in local density approximation and the maximally localized Wannier method [4]. The figure 1 shows the electronic structure and the schematic picture of the constructed four-orbital Hubbard model, which contains the $d_{x^2-y^2}$ and $d_{3z^2-r^2}$ orbitals. By adopting the fluctuation exchange approximation (FLEX) to the model, we have obtained the green's function of dressed particles with self-energy triggered by spin- and charge-fluctuations. We have obtained an eigenvalue λ, which can be used as

a measure of T_c, plugging the green's function into the linearized Eliashberg equation. We have judged that λ~0.6 of $La_3Ni_2O_7$ is as high as that of cuprates ($\lambda \sim 0.5-0.8, T_c \sim 40-135$ K) and this explains the experimental observed T_c (~ 80 K) [5]. The superconducting gap function, which is obtained as an eigen function of linearized Eliashberg equation, can be regarded as a spin-fluctuation mediated *s*-wave superconductivity in which the sign is inverted between bonding and anti-bonding bands formed by the $d_{3z^2-r^2}$ orbitals [5].

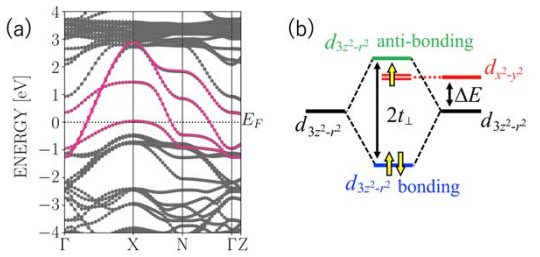

Fig. 1: (a) First-principles electronic structure (gray) and four-orbital model (magenta) of $La_3Ni_2O_7$. (b) shows a schematic picture of the model

Based on the analysis method, we have also investigated $La_4Ni_3O_{10}$, a trilayer member of Ruddlesden-popper type nickelates, in a collaboration with experimental group of Prof. Takano from NIMS. In this collaboration, we theoretical group predicted that $La_4Ni_3O_{10}$ can structurally transit to tetragonal symmetry as in $La_3Ni_2O_7$ by performing first-principles structural optimization and phonon calculation [6]. By performing FLEX calculation as the case of $La_3Ni_2O_7$, we have obtained λ of $La_4Ni_3O_{10}$ about 0.4, which means that a $La_4Ni_3O_{10}$ can exhibit a superconductivity with $T_c \sim 20$ K [6]. After the calculation, Takano's experimental group have found that the $La_4Ni_3O_{10}$ exhibit superconductivity with $T_c \sim 23$ K [6]. This means that our theoretical analysis predicted the superconductivity of $La_4Ni_3O_{10}$ before the experimental discovery.

To summarize, by using first-principles calculations, we have modeled the pressurized state of two Ruddlesden-popper type nickelates, $La_3Ni_2O_7$ and $La_4Ni_3O_{10}$, to investigate superconductivity. The superconducting nature may be the spin-fluctuation mediated *s*-wave superconductivity with pairs formed between different layers. The eigenvalue λ in FLEX explains the experimental T_c.

References

[1] R. T. Scalettar, J. W. Cannon, D. J. Scalapino, and R. L. Sugar, Phys. Rev. B **50**, 13410 (1994).

[2] M. Nakata, D. Ogura, H. Usui, and K. Kuroki, Phys. Rev. B **95**, 214509 (2017).

[3] H. Sun et al., Nature (London) **621**, 493 (2023).

[4] N. Marzari and D. Vanderbilt, Phys. Rev. B **56**, 12847 (1997).

[5] H. Sakakibara, N. Kitamine, M. Ochi, K. Kuroki, Phys Rev. Lett. **132**, 106002 (2024).

[6] H. Sakakibara et al., Phys. Rev. B **109**, 144511 (2024).

Electronic Structure and the Fermi surface of ReO_3

Takahiro Maehira
Faculty of Science, University of the Ryukyus, Nishihara, Okinawa 903-0213

Rhenium trioxide is an inorganic compound with the formula ReO_3. It is a red solid with a metallic luster that resembles copper in appearance. It is the only stable trioxide of the Group 7 elements. Rhenium trioxide exhibits extremely low electrical resistance not found in ordinary metal oxides. They are also similar to metals in that their resistance decreases as the temperature decreases. At around 78 K, it exhibits conductivity comparable to silver, which the highest electrical conductivity of any metal[1, 2]. ReO_3-type structures can be described as ABX_3 perovskites in which the A-cation site is unoccupied. They therefore have the general composition BX_3, where B is normally a cation and X is a bridging anion. The chemical diversity of such structures is very broad, ranging from simple oxides and fluorides, such as WO_3 and AlF_3, to more complex systems in which the bridging anion is polyatomic, as in the Prussian blue-related cyanides such as $Fe(CN)_3$ and $CoPt(CN)_6$. We studied cubic ReO_3 with a space group of Pm3m. The calculation for the energy band structures was carried out by using the OpenMX code(`http://www.openmx-square.org/`).

First, we discuss the calculated results for ReO_3 as shown in Figure 1, in which we depict the energy band structure along the symmetry axes in the Brillouin zone, which is shown in Figure 1, in the energy region from -25.0 to 25.0 eV. The Fermi level E_F is at 0.0 eV. for ReO_3 and indicated by dashed lines in Figure 1. With respect to the energy band structure near E_F, we emphasize that there is always hybridization between the Re 5d and O 2p states in ReO_3.

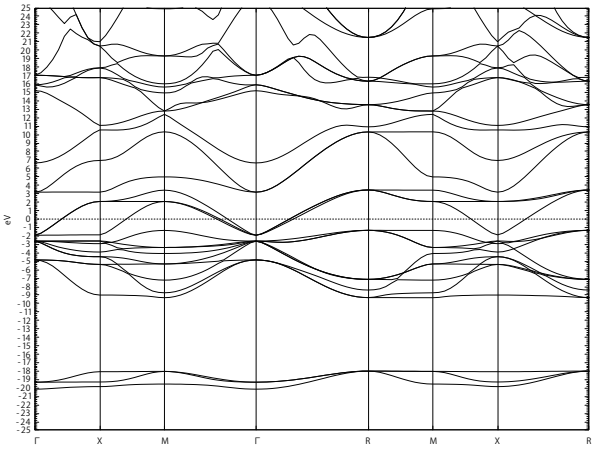

Figure 1: The energy band structure for ReO_3. E_F indicates the position of the Fermi level.

The total number of holes is equal to that of electrons, which represents that ReO_3 is a compensated metal. Since the lowest twelve bands are fully occupied, as shown in Figure 1, the next three bands are partially occupied, while higher bands are empty. This compound is compensated metal because of having two chemical units in the unit cell.

We move to discuss the Fermi surface of ReO_3. Three bands cross the E_F, therefore ReO_3 has three Fermi surfaces in Figure 2. The 13th, 14th and 15th bands construct the Fermi surface. The color on the Fermi surface illustrates the distribution of the Fermi velocity components. Fermi surfaces for ReO_3 centered at the Γ points, respectively. The 13th band construct large hole sheet centered at the Γ point and multiply connected with six arms along $\langle 100 \rangle$ direction, as shown Figure 2(a). The 14th band construct electron sheet cen-

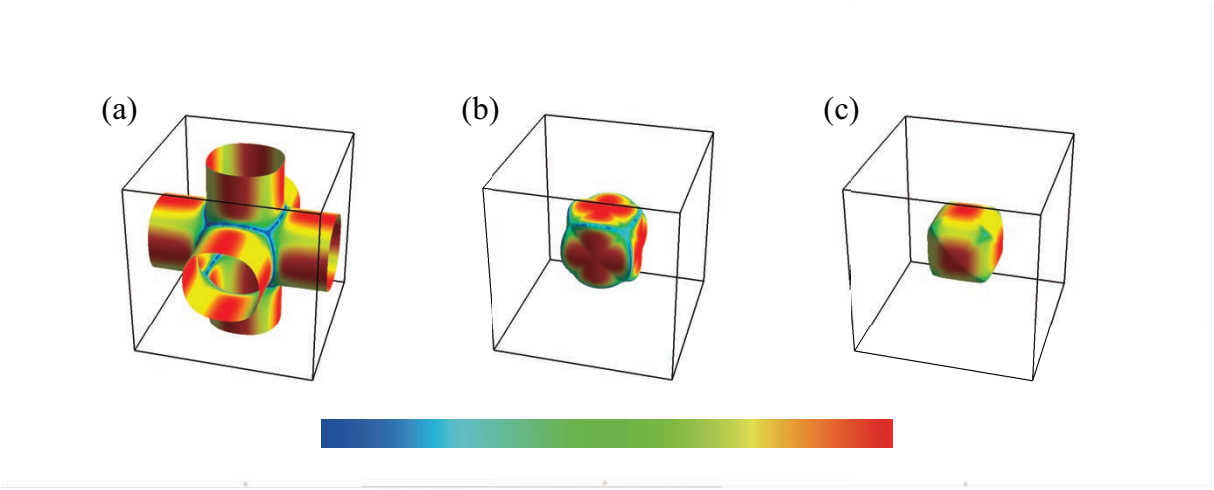

Figure 2: Calculated Fermi surfaces of ReO_3 for (a) 13th band hole sheet, (b) 14th band electron sheet, and (c) 15th band electron sheet. Colors indicate the Fermi velocity components on the Fermi surface. Red-shift indicate the increase of the Fermi velocity components. The center of the Brillouin zone is set at the Γ point.

tered at the Γ point and its shape is almost cubic, as shown Figure 2(b). The 15th band construct small electron sheet centered at the Γ point and its shape is almost cubic, as shown Figure 2(c).

The calculated total density of states (DOS) for ReO_3 is shown in Figure 3, in the energy region from -25.0 to 25.0 eV. The total density of states for ReO_3 is shown by the solid black line and the s, p, d and f states are shown by the solid color lines, respectively. This figure tells us that the DOS of the d states is higher than that of the f states at the Fermi level.

We have applied the band calculation of the electronic structure of ReO_3 based on the itinerant electrons by assuming a non-magnetic phase. We found that the hybridization between Re $5d$ and O $2p$ states occurs near E_F. The Fermi surfaces for ReO_3 are composed of one hole sheet and two electron sheets. The Fermi surface in the 13th band is multiply connected with the arms so some open orbits are expected to pass along the arms in some range of angles. We analyzed the existence of the open orbits in the ⟨100⟩ directions on the Fermi surface for ReO_3.

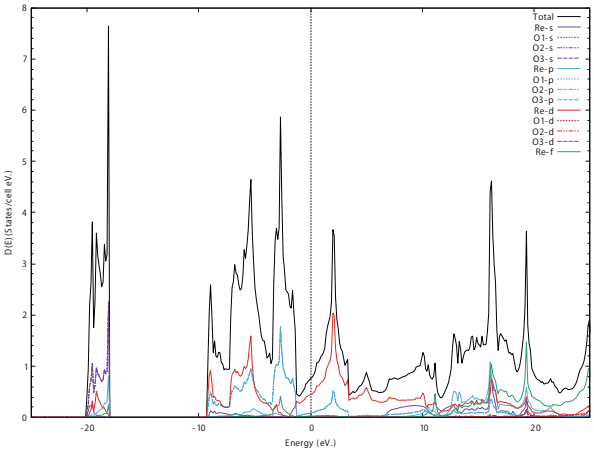

Figure 3: The density of states for ReO_3. E_F indicates the position of the Fermi level shown by the dashed line.

References

[1] A. Ferretti, D. B. Rogers, J. B. Goodenough: J. Phys. Chem. Solids **26** (1965) 2007.

[2] T. P. Pearsall, C. A. Lee: Phys. Rev. B. **10** (1947) 2190.

Theoretical Study on Electronic Properties in New Nanoscale Surfaces and Interfaces

Katsuyoshi KOBAYASHI
Department of Physics, Ochanomizu University
2-1-1 Otsuka, Bunkyo-ku, Tokyo 112-8610

We theoretically studied the magnetic structure of V_5Se_8 monolayers. V_5Se_8 is a layered material composed of VSe_2 layers and V intercalant layers. It is known that bulk V_5Se_8 has an antiferromagnetic structure at low temperatures. However, ferromagnetic behavior has been observed in a recent experiment of V_5Se_8 thin films [1]. We studied the magnetic sturtcure of V_5Se_8 monolayers by a density functional method in 2023. We used the program package VASP for density-functional calculations.

First we calculated the magnetic structure of bulk V_5Se_8. It is established that the V atoms of the intercalant layer have magnetic moments, and the magnetic moments in the VSe_2 layers are zero or negligible. The experimental value is 1.2 μ_B. The calculated values are 1.79 and 1.57 μ_B by GGA and LDA, respectively. Though the calculated values are larger than the experimental one, the LDA calculation better reproduces the experimental one. They are calculated at the experimental lattice constant. The lattice constant is better reproduced by GGA than LDA. The deviation from the experimental value is 0.9 % by GGA and -2.2 % by LDA. The minus sign means contraction.

Next we calculated the magnetic structure of a V_5Se_8 monolayer. Figure 1 shows the atomic structure of the V_5Se_8 monolayer studied in our calculation. First both the structural optimization and magnetic structure calculation were performed using GGA. It was found that a ferromagnetic structure has the lowest total energy among various magnetic structures considered in our calculation. In addition to the V atoms in the intercalant layers, those in the VSe_2 layers also have magnetic moments. This seems a surface effect.

The structural optimization and magnetic structure calculation also were performed using LDA. In this case the nonmagnetic structure has lower energy than magnetic ones. This result arises from the short interlayer distances optimized by LDA. Figure 2 shows the magnetic moment calculated as a function of the interlayer distance. When the interlayer distance is short, the energy gain due to exchange interaction is relatively reduced, which favors the nonmagnetic state. Since the bulk lattice constant is better reproduced by GGA, it seems better to use GGA for structural optimization and LDA to estimate magnetic moments.

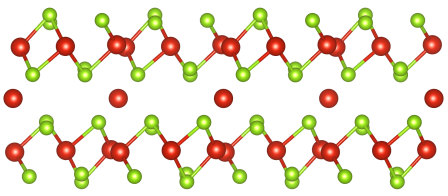

Figure 1: Atomic structure of a V_5Se_8 monolayer.

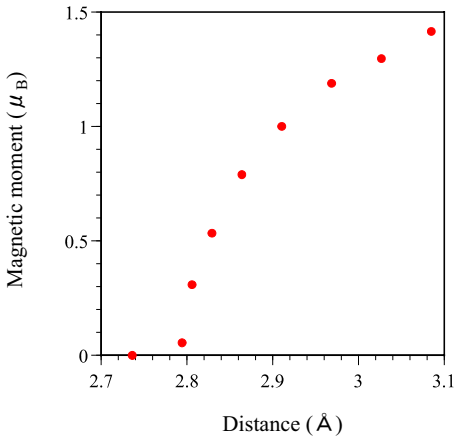

Figure 2: Magnetic moment of V atoms in the intercalant V layer of the V_5Se_8 monolayer calculated by LDA as a function of the distance between a V atom in the intercalant V layer and its nearest neighbor V atom in the VSe_2 layer. The distances optimized by LDA and GGA are 2.74 and 3.03 Å, respectively. The bulk distance is 2.95 Å.

References

[1] M. Nakano *et al.*: Nano Lett. **19** (2019) 8806.

Electronic stress tensor density analysis for material surfaces

Masahiro FUKUDA

Institute for Solid State Physics,

The University of Tokyo, Kashiwa-no-ha, Kashiwa, Chiba 277-8581

The electronic stress tensor density is a fundamental local physical quantity which is defined as the space-space components of the energy momentum tensor in the framework of quantum field theory. Since a half of the trace of the electronic stress tensor is related with the total energy of the system under the virial theorem, the analysis of the electronic stress tensor gives mechanical aspect of the chemical bond [1]. On the other hands, the material surface is important concept to discuss chemical reactivity, molecular absorptions, and force spectroscopy of atomic force microscopy. The surface defined by the zero kinetic energy density play a role as an electronic interface. The boundary surface of the positive-to-negative reversal of the kinetic energy density is consistent with the concept of the surface of materials in classical theory.

In this research, we revealed that the energy density constructed from the electronic stress tensor at the materials surface represents localization of the electronic charge density. We also found that the physical quantity expressed as the electron number density derivative of the energy density corresponds to the regional chemical potential, and its value at the material surface allows us to visualize areas prone to chemical bonding, such as dangling bonds and π -bonds. This should lead to a better understanding of the experimental observation of AFM images using atomic attractive force. This analysis of regional chemical potentials is also expected to lead to the development of a method for predicting crystal growth processes occurring on the surface of materials due to molecular adsorption, etc., from the electronic steady state before the reaction.

We are currently working on the evaluation of regional chemical potentials using post-process calculations for the electronic structure of 2D materials [2] and surface materials [3] obtained by DFT calculations using OpenMX [4].

References

[1] A. Tachibana, New Aspects of Quantum Electrodynamics, Springer, 2017.

[2] M. Fukuda and T. Ozaki, Phys. Chem. Chem. Phys., **26**, 3367 (2024)

[3] R. Zhang *et. al*., arXiv:2403.17427 [cond-mat.mtrl-sci]

[4] OpenMX, http://www.openmx-square.org

Search and realization of novel electronic properties of surfaces and interfaces and of nanostructures

Takeshi INAOKA
Department of Physics and Earth Sciences, Faculty of Science, University of the Ryukyus, 1 Senbaru, Nishihara, Okinawa 903-0213

Using the van-der-Waals density functional theory, we have been investigating the electronic structure of x-form phthalocyanine (Pc) crystals and the iodine (I) doping effect on this structure. We employ the program package 'Vienna Ab initio Simulation Package' (VASP) [1-4] on system B (ohtaka) in the present study.

The Pc is a planar π-conjugated macrocyclic molecule which can include an atom of various species at its center position. The x crystal is constituted of a square-lattice arrangement of molecular chains with double period and with molecular planes normal to the stacking direction. Doped iodine I atoms can enter one-dimensional open channels between these molecular chains.

(A) x-SiPc and x-SiPcI crystals

Although the synthesis of x-SiPc crystals is still in its infancy, we chose Si for center atoms, because we found that SiPc molecules (monomers) have Si p_z derived orbitals right above the LUMO, which may overlap each other in the x-form stacking.

Last academic year, we elucidated the following points:
(1) Because Si atomic chains dimerize, Si p_z orbitals cannot form metallic bands.
(2) The staggering angle becomes 40°, because H_2-like bonding orbitals are created between laterally neighboring molecular planes.
(3) I doping decreases the band occupancy from half-filling, as is observed experimentally as the Mott insulator-metal transition.
(4) If we assume equally spaced I atomic chains, they form metallic bands with an effective-mass ratio of 0.15.

This academic year, we examined the stability of equally spaced I atomic chains. We calculated the force working on an I atom when it is displaced in the chain-axis direction and the electronic structure is optimized with atom positions fixed. We found that the restoring force operates on each I atom displaced. The arrangement of x-SiPc chains act to create equally spaced I atomic chains.

According to X-ray analysis, the I atoms, whose average positions are equally spaced, have elongated temperature factors along the chain axis. This is interpreted as indicating that I atomic chains are trimerized without interchain correlations. Therefore, we analyzed the stability of trimerized I atomic chains in x-SiPcI crystals. We considered crystals with six-fold period in the stacking direction, and performed structure optimaization assuming formation of trimers. The result is exhibited in Fig. 1. This trimerization turned out to lower the total energy by 58.6 meV per unit cell. The I-I bond length in each trimer is 3.00Å, and the distance between neighboring trimers is 3.58Å. The

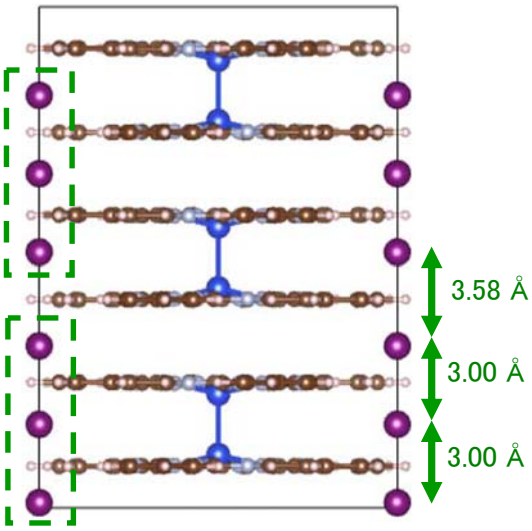

Fig. 1 Side view of the x-SiPcI crystal structure with trimerized I atomic chains.

trimerization induces a band gap at E_F, which prevent I atomic chains from making metallic bands. The SiPc chains operate to create equally space I atomic chains, while the I atoms try to form trimerized chains. These effects compete with each other, but the trmirization effect is larger.

(B) LiPc chian

In preparation for next year's study of x-LiPc and x-LiPcI crystals, we analyzed the electronic structure of a single x-LiPc chain. This molecular chain has a double period in the stacking direction, and two molecules in a primitive unit cell are stacked face-to-face with a staggering angle of 45°. Figure 2 exhibits the band dispersions on the Γ-Z line. A pair of the bands b185 and b186 are formed by band folding at E_F at the Z point. The bands b185～b190 with significant dispersions originate from π electrons. Figure 3 show the electron-density distributions (isosurfaces) of those two states at E_F which are formed by π electrons. The orbital of each state is localized to one of the two molecules in the unit cell, and each state is occupied by one electron, namely, an unpaired electron. Although our band theory cannot treat Mott insulators directly, presence of these unpaired electrons strongly suggests appearance of Mott insulators, as is observed experimentally [5]. By chemical I doping and dedoping, Teruya et al. successfully converted insulators of x-LiPc to metals of x-LiPcI and vice versa reversibly [5].

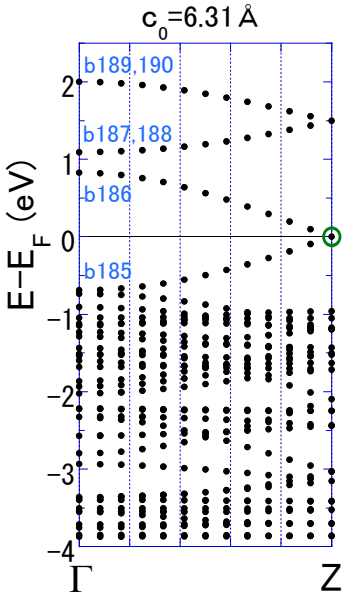

Fig. 2 Band dispersions on the Γ-Z line of a single x-LiPc chain. The green circle represents the two degenerate states at E_F.

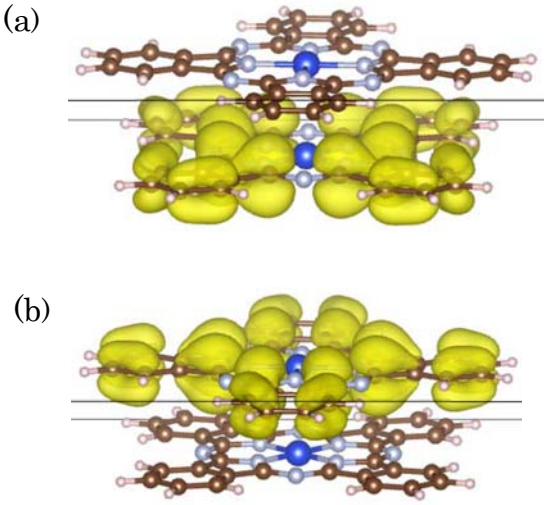

Fig. 3 Electron-density distributions (isosurfaces) of the two degenerated states at E_F at the Z point, as marked by the green circle in Fig. 2.

Next academic year, we examine the electronic structure of x-LiPc and x-LiPcI crystals and the I doping effect. We will be able to elucidate how I doping affects the band structure, and induce the insulator-metal transition, and what the electron states of I atomic chains are like.

References

[1] G. Kresse and J. Hafner: Phys. Rev. B **47**, 558-561 (1993).
[2] G. Kresse and J. Furthmüller: Comput. Mat. Sci. **6**, 15-50 (1996).
[3] P. E. Blöchl: Phys. Rev. B **50**, 17953 (1994).
[4] J. Klimeš, D. R. Bowler, and A. Michaelides: Phys. Rev. B **83**, 195131 (2011).
[5] R. Teruya et al.: Angew. Chem. Int. Ed. **61**, e202206428 (2022).

First-principles study on designing magnetic tunnel junctions from a viewpoint of Néel temperature

Katsuhiro Tanaka
Department of Physics, University of Tokyo, Hongo, Bunkyo-ku, Tokyo 113-0033

Mn_3Sn, an antiferromagnet with non-collinear spin texture, is a promising candidate for realizing the antiferromagnetic spintronics devices. Its magnetic structure, which is tightly connected to the topological electronic structure, has caused experimental observations of the tunnel magnetoresistance (TMR) effect [1] as well as the anomalous Hall and anomalous Nernst effects [2] in antiferromagnets. Studies on the ferromagnetic materials have suggested that thermal fluctuations at the interface between magnetic materials and insulators will depress the TMR effect also in the antiferromagnetic systems. Hence, from an application point of view, we believe that it is essential to enhance the Néel temperature of Mn_3Sn, which is typically 420 K. In this numerical study, we aim to search for suitable elemental substitutions that will increase the Néel temperature in Mn_3Sn.

First-principles calculations in random substitution systems were performed using the coherent potential approximation (CPA). We built a classical spin Hamiltonian for each doping system as follows:

$$\mathcal{H} = -2\sum_{i<j} J_{ij}(n_i, n_j)\boldsymbol{s}_i \cdot \boldsymbol{s}_j. \qquad (1)$$

Here, $J_{ij}(n_i, n_j)$ is the exchange coupling constants between i-th and j-th up to a cutoff length $2a$, where a is the lattice constant depending on the constituent elements. The normalized classical spin moment at the $i(,j)$-th site is denoted by $\boldsymbol{s}_{i(,j)}$. The dependence of the coupling constants on the kinds of the atoms n_i and n_j were calculated based on first principles calculation using the Korringa-Kohn-Rostoker (KKR) Green function method and the Liechtenstein formula [3] in the paramagnetic local moment disordered states, which has been implemented on the AkaiKKR code [4, 5].

Conducting the naive Monte Carlo (MC) simulations on the above Hamiltonian, we determined the Néel temperature from the peak of the magnetic heat capacity. Each MC simulation runs 100,000 MC steps for relaxation and 100,000 MC steps for the calculation of the magnetization for 5–10 atomic arrangements constructed with different random number sequences.

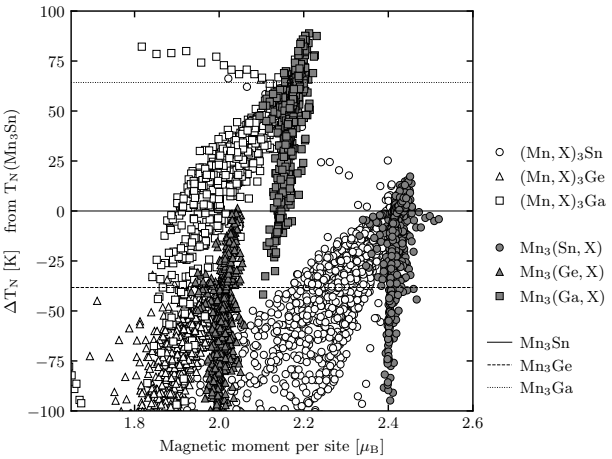

Figure 1: Variation of the Néel temperature of Mn_3Sn, Mn_3Ge, and Mn_3Ga with chemical substitution estimated by first-principles calculations.

By using the above methodology, we confirmed that the calculated Néel temperatures for Mn_3Sn, Mn_3Ga, and Mn_3Ge, which have

similar crystal and magnetic structures, semi-quantitatively reproduce the relative values of the experimental measurements. Furthermore, we carried out comprehensive calculations on systems with approximately 60 different elements substituted at levels ranging from 0–20% in the base materials. These calculations identified elements that contribute to an increase in the Néel temperature upon substitution (Fig. 1) [6].

References

[1] X. Chen, T. Higo, K. Tanaka *et al.*, Nature **613**, 490 (2023).

[2] S. Nakatsuji *et al.*, Nature **527**, 212 (2015); M. Ikhlas *et al.*, Nature Phys **13**, 1085 (2017); S. Nakatsuji and R. Arita, Annu. Rev. Condens. Matter Phys. **13** (2022).

[3] A. I. Liechtenstein *et al.*, J. Magn. Magn. Mater. **67**, 65 (1987).

[4] AkaiKKR (Machikaneyama, private version). http://kkr.issp.u-tokyo.ac.jp/

[5] T. Fukushima *et al.*, Phys. Rev. Materials **6**, 023802 (2022).

[6] Y. Toga, K. Tanaka *et al.*, in preparation.

Ab-initio MD simulation for molten $RbAg_4I_5$

Shuta TAHARA[1] and Yuki KANAE[2]

[1]*Department of Liberal Arts and Sciences,*

Chukyo University, 101-2 Yagoto Honmachi Showa-ku, Nagoya, Aichi 466-8666

[2]*Department of Physics and Earth Sciences, Graduate School of Engineering and Science,*

University of Ryukyus, 1 Senbaru Nishihara-cho, Nakagami-gun, Okinawa 903-0213

We have been carried out experimental and theoretical studies with an interest in the diffusion mechanism of Ag ions diffusing in solids, such as AgI and $RbAg_4I_5$ and its molten phases [1-3]. In our earlier studies using classical MD, we succeeded in roughly reproducing the characteristics of the structure factor $S(Q)$ obtained experimentally, but there was a problem that the accuracy was somewhat low for short range distribution. Therefore, we carried out first-principles MD simulations using Quantum Espresso software and the supercomputers ohtaka and kugui in an attempt to derive a more accurate structural model. Fig 1 shows comparisons of the $S(Q)$ of molten $RbAg_4I_5$. The present FPMD results well reproduce the experimental data, including the high wavenumber side of S(Q), indicating that the short-range order is well reproduced. In addition, a characteristic distribution of connected Ag ions was observed in the derived structural model.

We reported these results in the conference held by the molecular simulation society of Japan.

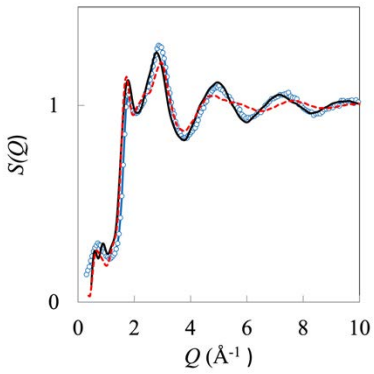

Fig. 1: Structure factors of molten $RbAg_4I_5$. Open circles [1], red dotted curve [1], and black curve indicate experimental data, classical MD, and FPMD of this study, respectively.

References

[1] S. Tahara and T. Fukami, J. Phys. Soc. Jpn. **84**, 024602 (2015).

[2] S. Tahara et al., J. Chem. Phys. **143**, 044509 (2015).

[3] S. Tahara, et al., EPJ Web conf. **151**, 03006 (2017).

A Moiré Model of Si(111)-√7×√3-In Surface

Kazuyuki UCHIDA

Kyoto Sangyo University, Kamigamo-Motoyama, Kyoto, 603-8555

Using ab-initio calculations based on the density functional theory, we have successfully constructed a new superstructure model for the Si(111)-√7×√3-In surface [1-4]. The model explains the long-range image observed in STM experiments [5] and the band structure obtained by ARPES experiments [6], being more effective than the previous model [7,8] which only replicated the ARPES experiment. We have also shown that the arrangement of bright spots in the STM image can be interpreted as a one-dimensional moiré. The calculations were conducted using the RSDFT program package [9,10] combined with a band-unfolding tool.

References

[1] J. Kraft, S. L. Surnev, and F. P. Netzer, Surface Science 340, 36 (1995).

[2] T. Zhang, P. Cheng, W. -J. Li, Y. -J. Sun, G. Wang, X. -G. Zhu, K. He, L. Wang, X. Ma, X. Chen, Y. Wang, Y. Liu, H. -Q. Lin, J. -F. Jia, and Q. -K. Xue, Nat. Phys. 6, 104 (2010).

[3] T. Uchihashi, P. Mishra, M. Aono, and T. Nakayama, Phys. Rev. Lett. 107, 207001 (2011).

[4] S. Yoshizawa, T. Kobayashi, Y. Nakata, K. Yaji, K. Yokota, F. Komori, S. Shin, K. Sakamoto, and T. Uchihashi, Nature Commun. 12, 1462 (2021).

[5] S. Yamazaki, Y. Hosomura, I. Matsuda, R. Hobara, T. Eguchi, Y. Hasegawa, and S. Hasegawa, Phys. Rev. Lett. 106, 116802 (2011).

[6] E. Rotenberg, H. Koh, K. Rossnagel, H. W. Yeom, J. Scha ̈fer, B. Krenzer, M. P. Rocha, and S. D. Kevan, Phys. Rev. Lett. 91, 246404 (2003).

[7] J. W. Park and M. H. Kang, Phys. Rev. Lett. 109, 166102 (2012).

[8] K. Uchida and A. Oshiyama, Phys. Rev. B 87, 165433 (2013).

[9] J. -I. Iwata, D. Takahashi, A. Oshiyama, B. Boku, K. Shiraishi, S. Okada, and K. Yabana, J. Comput. Phys. 229, 2339 (2010).

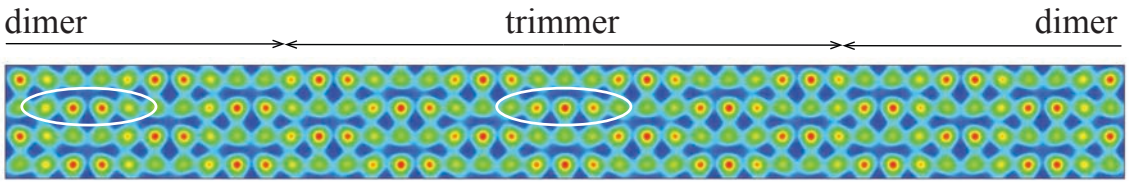

Fig.1： An STM image simulated for the new model proposed in this work.

Electronic band structures and Raman-spectra of intermediate states between $MoSe_2$ and Janus-MoSeS

Masaaki MISAWA
Department of Intelligent Mechanical Engineering, Fukuoka Institute of Technology
3-30-1 Wajiro-higashi, Higashi-ku, Fukuoka 811-0295

Janus-TMDC, which is obtained by substituting a chalcogen element on only one side of transition metal dichalcogenides (TMDCs), has attracted much attention as a functional material with the potential to lead to new electronics technologies. While various structures based on Janus-TMDC have been proposed for electronics applications, there are still many unknowns regarding how the physical properties change during the elemental substitution process. In this study, we performed first-principles simulations of the electronic band structure and evolution of Raman spectra during the synthesis of Janus-MoSeS by elemental substitution of $MoSe_2$[1]. The first-principles calculations based on density functional theory were conducted using the Vienna Ab initio Simulation Package (VASP)[2]. The Raman spectra were simulated using Phonopy[3] with Phonopy-Spectroscopy package[4].

To compute electronic band structure, the Janus $MoSe^bSe^t_{1-x}S^t_x$ (x = 0, 0.25, 0.50, 0.75 and 1.00) structures were prepared by replacing certain Se atoms with S atoms in a $2\times2\times1$ supercell of the crystalline unit cell. As a result of the calculation, we obtained the bandgap energies of 1.532, 1.520, 1.536, 1.595 and 1.652 eV for x = 0, 0.25, 0.50, 0.75 and 1.00, respectively. Note that the obtained bandgap energies for $x = 0$ and 1.00 are consistent with experimental bandgap energies very well. In an experimental result of photoluminescence (PL) spectra, it was observed that the PL peak shifts slightly to the lower energy side at the beginning of the elemental substitution, and then transfer to the higher energy side. Our calculations clearly explain this experimental PL transition.

In addition, we performed simulations of Raman spectra. In the experiment, it was observed that the A_1 mode, which characterizes $MoSe_2$, disappeared immediately with the progress of elemental substitution, and the $^1A_1$ mode, which characterizes Janus-MoSeS, is appeared. During this process, an unknown peak appeared around 260 cm^{-1}, which exists only in intermediate states and is not found in $MoSe_2$ or MoSeS. Our simulation results show that a peak appears at 258.1 cm^{-1} in the structure of $x = 0.5$, indicating a complex mode in which S and Se are intricately correlated.

This year, we also conducted first-principles calculations about the self-limiting growth mechanism of TMDC nanoribbons[5].

References

[1] H. Suzuki *et al.*: Nano Lett. **23**, 4533 (2023).

[2] G. Kresse and D. Joubert: Phys. Rev. **59**, 1758 (1999).

[3] A. Togo: JPSJ **92**, 012001 (2023).

[4] J. M. Skelton *et al.*: Phys. Chem. Chem. Phys. **19**, 12452 (2017).

[5] H. Suzuki *et al.*: ACS Nano **17**, 9455 (2023).

Lattice thermal conductivity calculation of iridium oxide $Ca_5Ir_3O_{12}$

Shoya Kawano

Department of Electrical and Electronic Engineering, Kyushu Institute of Technology, Kitakyushu, Fukuoka, 804-8550

We have studied the title compound, Ca5Ir3O12, which has attracted attention due to its strong spin-orbit interaction (SOI) [1]. This compound exhibits antiferromagnetic ordering below 7.8 K, undergoes a second order phase transition at 105 K, and displays non-linear conductivity along the c-axis. Further exploring its properties, we have conducted investigations into the thermal conductivity using synchrotron X-ray studies of lattice vibrations. To compare with these experiments, we have performed calculations using this supercomputing system.

We conducted calculations on the phonon lifetimes of $Ca_5Ir_3O_{12}$ using force constants determined through density functional theory (DFT) calculations performed with the Quantum ESPRESSO (QE) code [2] and the ALAMODE code [3] for phonon calculations. These calculations involved determining force constants that enabled us to compute phonon dispersion and phonon lifetimes.

We performed calculations using a 1×1×3 supercell. For the finite displacement and random displacement approaches, displacement distances of 0.02 Å and 0.04 Å were respectively employed. The random displacement approach was utilized to calculate the anharmonic terms of the force constants, for which 20 random structures were used. In QE code, we employed norm-conserving pseudopotentials generated by the ONCVPSP (Optimized Norm Conserving Vanderbilt Pseudopotential) code, sourced from PseudoDojo [4]. The Perdew-Burke-Ernzerhof type exchange-correlation function was used. We set a Γ-point-centered 4×4×3 k-point sampling for the supercell calculations. The energy cutoff for the wave function was 96 Ry, with a convergence criterion for the electronic self-consistency loop set at 10^{-10} Ry, and Gaussian smearing method with a smearing width of 0.002 Ry was used. We included the SOI effect.

Figure 1 displays the phonon dispersion relation for $Ca_5Ir_3O_{12}$, which is consistent with our studies conducted using synchrotron radiation experiments and calculations. The slope of the dispersion relation (dE/dk) corresponds to the phonon group velocity. The region from Γ to A shows a high slope, indicating a high group velocity.

We estimated the phonon lifetimes for $Ca_5Ir_3O_{12}$; most lifetimes are short, averaging around 0.5 ps. Long-lived phonons are

primarily found near ω = 0, contributing significantly to the thermal conductivity. When compared to phonon lifetimes obtained from our synchrotron radiation experiments, the results are consistent. The calculated thermal conductivities in the a-axis and c-axis directions are 0.09 W/mK and 0.69 W/mK, respectively, which align with experimentally observed values of approximately 1 W/mK. The very short phonon lifetimes contribute to the low thermal conductivity. Furthermore, the high group velocity in the Γ-A direction contributes to the anisotropy in thermal conductivity.

For the density functional calculations for each displacement, we used the F16CPU of system B with 2048 parallel computing cores using MPI. For the thermal conductivity calculation, a hybrid MPI/OpenMP parallelization approach was employed using the F16CPU of system B.

[1] K. Matsuhira *et al*. *J*. *Phys*. *Soc*. *Jpn*. **87**, (2018).

[2] https://www.quantum-espresso.org

[3] https://alamode.readthedocs.io

[4] http://www.pseudo-dojo.org

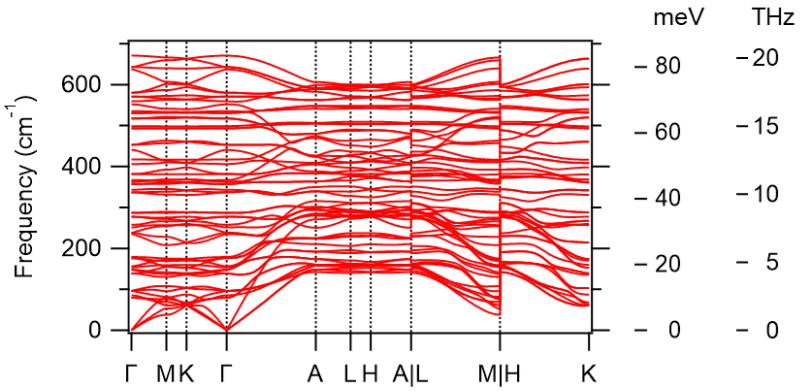

Fig. 1 Phonon dispersion of $Ca_5Ir_3O_{12}$ with SOI.

Activation barrier investigation for methane dissociation on Ni nanoparticle doped CeO_2

Takaya FUJISAKI

Faculty of Materials for Energy

Shimane University, 1060 Nishikawazu, Matsue, Shimane 690-0823

Introduction

In the world of renewable energy, biomass stands out as an important resource. It can produce methane through a process called anaerobic fermentation. This methane can then be used as a carrier for hydrogen, which is great for fuel cells because they're really good at making electricity. Recent research has shown that we can use biomass, like waste from shrimp farming, to make methane as seen in Fig. 1 [1][2]. This opens up the possibility of using money made from shrimp farming to help pay for fuel cells, which is good for both industries and helps make energy production more sustainable.

Getting hydrogen from methane efficiently is significantly important for making these fuel cell systems work well. That's why scientists are working hard to improve a process called dry reforming of methane (DRM). They've found that using a catalyst called CeO_2 loaded with tiny nickel particles could be a game-changer for how we use methane in fuel cells. This study dives deep into understanding how methane and carbon dioxide break apart during the DRM reaction to make the process more efficient.

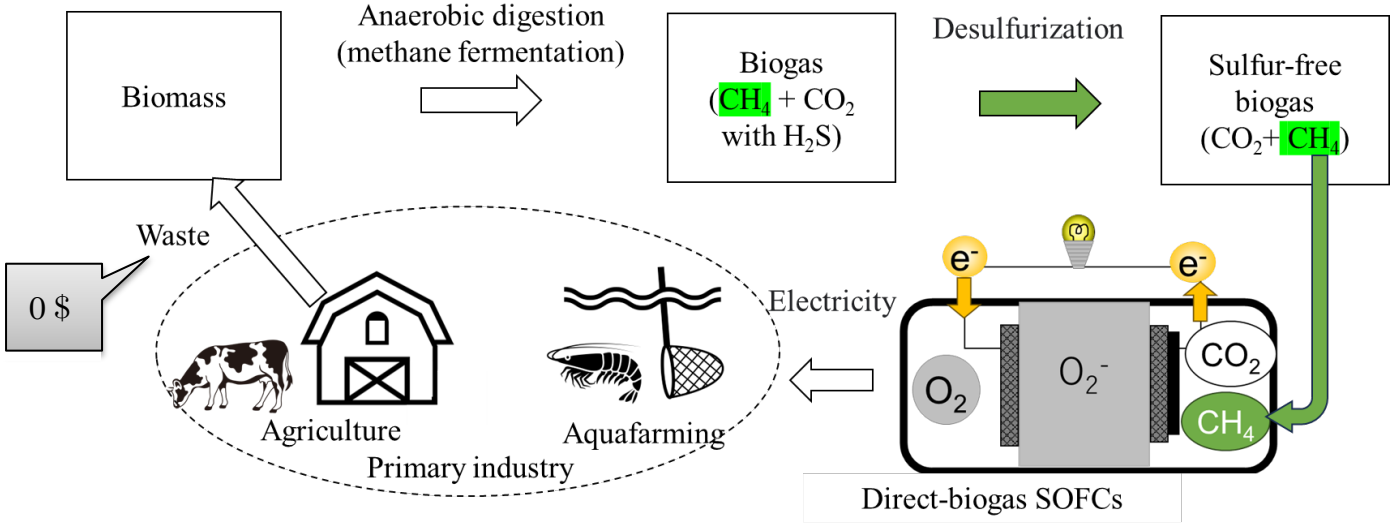

Fig.1 Schematic of combined biomass and fuel cell system

Analytical Methods

This study used a method called density functional theory (DFT) to figure out how hard it is for methane and carbon dioxide to break apart. They used a computer program called Vienna ab initio simulation package (VASP) to look at different setups of nickel nanoparticles on surfaces made of CeO_2. Then, they used a method called the nudged elastic band (NEB) to calculate how hard it is for methane and carbon dioxide to break apart for each setup. To make sure the computer results were accurate, they also did real experiments using a special catalyst made of nickel and CeO_2. By measuring how much hydrogen was made and how much methane was used up, they got a good idea of how fast the reactions were happening.

Results and Discussion

Fig. 2 shows the activation barrier of methine dissociation (left) and transition state (TS) of methane (right). The study found out some interesting things about how methane breaks apart. It turns out that it's easier for methane to break apart when the nickel particles have more positive charge. They also found that breaking apart carbon dioxide is harder than breaking apart methane during the DRM reaction. This means that how fast carbon dioxide breaks apart might control how fast the whole reaction happens. The study suggests that if we can find ways to make the nickel particles even more positively charged, we might be able to speed up the whole process even more, which would be great for making fuel cells more efficient.

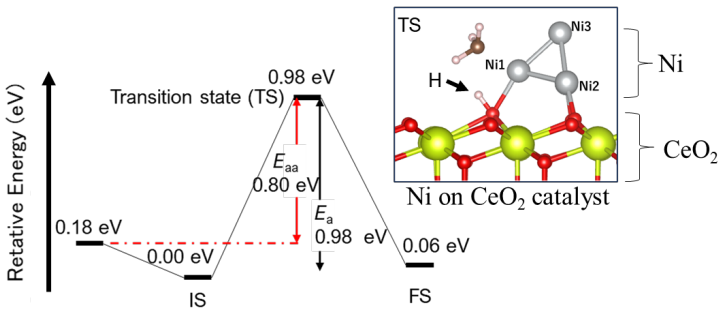

Fig.2 Ni on CeO_2 catalyst for making H_2

.

Acknowledgments

We extend our gratitude to The Institute for Solid State Physics, The University of Tokyo for providing access to their supercomputer facilities and for their invaluable support and guidance throughout this research endeavor.

References

[1] Y. Shiratori et al., Fuel Cells **19**, 346-353 (2019).

[2] P. H. Tu et al., Fuel Cells, 1-11 (2024).

Compression behavior of Xe in silica melt

Daisuke WAKABAYASHI

Photon Factory, Institute of Materials Structure Science,

High Energy Accelerator Research Organization (KEK), Tsukuba 305-0801

Noble gasses are believed to have the same abundance as the ancient Earth and planetary atmospheres because of their chemical inertness. However, it is known that the abundance of Xe in the current Earth's atmosphere is significantly lower compared to primitive meteorites. The lack of Xe in the Earth's atmosphere, known as "missing Xe," has long been studied as a major mystery in the field of geochemistry. Xe is heavier and relatively more chemically reactive among noble gases. It is hypothesized to form compounds under high temperature and pressure, remaining trapped in the deep Earth since its formation, but the detailed process remains unresolved. In this study, the behavior of Xe in magma under high temperature and pressure is simulated to elucidate its potential entrapment in the deep Earth.

Our previous experimental and theoretical studies have confirmed structural changes in the network of SiO_4 tetrahedra constituting silica glass under high pressure [1-2]. The structural change in the network is expected to affect the behavior of Xe significantly. In this project, ab-initio molecular dynamics simulations were conducted for Xe in silica glass under high pressure conditions up to 10 GPa, where the network structural changes occur.

Ab-initio calculations were carried out with a system of 145 atoms (48Si + 96O + 1Xe) under periodic boundary conditions using the QXMD code [3]. First, simulations were performed on the system without a Xe atom for more than 10 ps at 3,000 K. Then, a Xe atom was added to a void in the final atomic configuration, and subsequent calculations were performed for more than 10 ps. These calculations were conducted under the pressure conditions of 0, 3, 6, and 10 GPa.

The structure and behavior of the main component, SiO_2, remained unchanged regardless of the presence of Xe. The network structure composed of SiO_4 tetrahedra changed with pressure, leading to the collapse of voids.

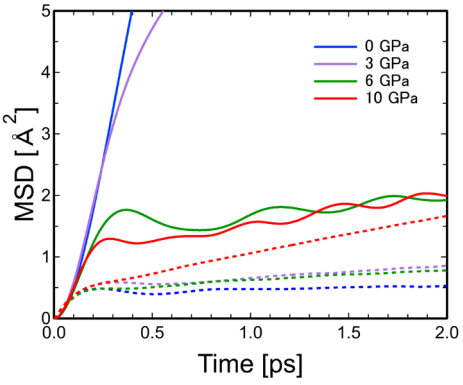

Fig. 1. Pressure dependence of mean square displacement of Xe in SiO_2 glass. Dotted lines represent the data of Si.

The mean square displacement of Xe is shown in Fig. 1, together with that of Si for reference. Figure 1 shows that the diffusion of Xe is significantly inhibited at pressures above 6 GPa, strongly suggesting that Xe is trapped within the network of SiO_2 glass and unable to move. The atomic configuration of Xe at 6 GPa and 3,000 K is shown in Fig. 2. Indeed, it is evident that Xe is confined within a narrow void. This observation is in agreement with previous experiments on silicate melt [4].

The bonding properties were estimated with a population-analysis method. The overlap population between Xe and other atoms suggests that Xe does not have a strong bonding with them. Xe becomes trapped within the network not due to chemical bonding, but simply because the network narrows as a result of the structural changes.

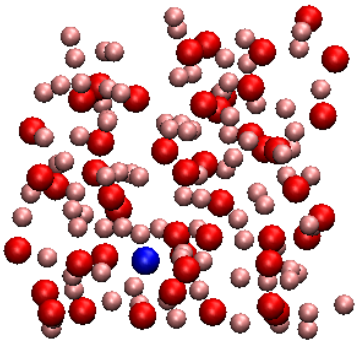

Fig. 2. Atomic arrangement of Xe in SiO2 glass at 6 GPa and 3,000 K (red: Si; pink: O; blue: Xe).

References

[1] D. Wakabayashi, N. Funamori, T. Sato, and T. Taniguchi, Phys. Rev. B **84**, 144103 (2011).

[2] E. Ryuo, D. Wakabayashi, A. Koura, and F. Shimojo, Phys. Rev. B **96**, 054206 (2017).

[3] F. Shimojo, S. Fukushima, H. Kumazoe, M. Misawa, S. Ohmura, P. Rajak, K. Shimamura, L. B. Oftelie, S. Tiwari, R. K. Kalia, A. Nakano, and P. Vashishta, Software X **10**, 100307 (2019).

[4] C. Leroy, C. Sanloup, H. Bureau, B. C. Schmidt, Z. Konôpková, and C. Raepsaet, Earth Planet. Sci. Lett. **484**, 103 (2018).

Analyses of diamond surface processes by machine-learning based potentials

Kouji INAGAKI

Graduate School of Engineering, Osaka University

Yamadaoka 2-1, Suita, Osaka 565-087

In this study, the wear process of diamond tools during the machining of ferrous materials has been analyzed using first-principles calculations. It was found that the reaction barrier for the Fe atoms to break into the C-C bonds is relatively low, and the fracture strength is lower than that of the C-C bonds. We attributed that this phenomenon is the cause of wear. In order to clarify the wear process directory by simulation, it takes much of computational cost. Machine learning techniques (MLP) is applied.

Since the reaction of Fe atom and C-C bond takes a five-folded structure in the path, we chose a graph-neural-network (GNN) based MLP. As a first step in our research, we generated a MLP to analyze the diffusion process of H on the Si surface, which we had previously identified. This is appropriate as a test calculation because Si adopts a five-folded structure in this reaction process. We employed Nequip application to form GNN-MLP, and succeeded in constructing the MLP using 1090 Si(001) 4x4 models as training data set with a Loss function of 0.008.

References

[1] K. Inagaki, K. Arima, The 84th JSAP Autumn Meeting 2023 20p-A202-5.

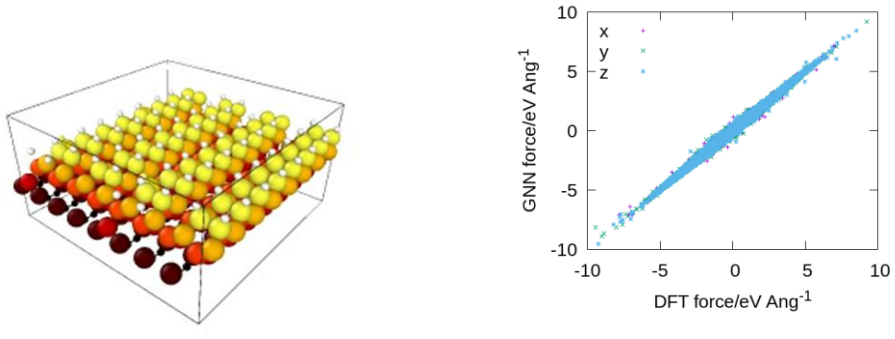

(a) (b)

Fig. 1: Training of machine learning potential. (a) Training data: One of the 1090 samples of Si (001) 4x4 6 layer model with surface 2x1 structure terminated by single H atoms with an excess H atom and bottom 16 dihydride. (b) Trained example. Loss function (defined in eqn. (9) in https://rdcu.be/dG4Zh) value is 0.008.

Reactivity analysis of high entropy alloys for catalyst informatics

Yoyo HINUMA

National Institute of Advanced Industrial Science and Technology (AIST)

1-8-31, Midorigaoka, Ikeda, Osaka 563-8577

High entropy alloys (HEAs) are a new class of metallic materials that contrast conventional alloy materials with few principal elements. HEAs consist of more than five near-equimolar components that are mixed to form single-phase solid solutions with high mixing entropy instead of (mostly) ordered intermetallic phases. Various unique synergistic effects result from such mixtures, such as high configuration entropy, lattice distortion, sluggish diffusion, and cocktail effects, resulting in peculiar characteristics including high mechanical strength, good thermal stability, and superior corrosion resistance.

Transition metal elements, especially late transition metal elements, are typically used in HEAs. The huge combination of elements makes brute-force searching impossible, and the question of which elements to use will always linger. This study considered five-component HEAs out of 12 late transition metal elements, which are Fe, Co, Ni, Cu, Zn, Ru, Rh, Pd, Ag, Ir, Pt, and Au. The activity of CO_2 adsorption, an important step in CO_2 hydrogenation, was investigated using first-principles density functional theory calculations. A CO_2 molecule was adsorbed on (111) surface sites of fcc-structure HEAs.

HEAs could be categorized into “binding”, “less binding”, or “inconclusive” HEAs. There were 27, 23, and 10 HEAs each, respectively, within 60 randomly chosen HEAs. “Binding” HEAs have low CO_2 adsorption energy positions of less than -0.08 eV, which is difficult to attain with elementary substances or binary alloys. These low adsorption energy, or more active, sites are found near top positions, whereas CO_2 does not adsorb near top “high symmetry” sites in “less binding” HEAs. HEAs containing Ru had a higher ratio of “binding” HEAs [1]. Calculating CO_2 adsorption energies could be a useful tool to check whether a specific HEA is “binding” or “less binding” prior to conducting extensive experiments.

References

[1] Y. Hinuma et al.: STAM Methods. 3 (2023) 2161807.

DFT calculations of HCOOH molecules in the pore of porous metal organic films on Cu(111)

Noriyuki Tsukahara

National Institute of Technology, Gunma College,

Toribamachi 580, Maebashi, Gunma, 371-0845, Japan

In this study, the adsorption structures of atoms and molecules that are trapped in a pore of porous organometallic thin films are investigated, and the interaction between the thin film and the adsorbed molecules is unveiled by DFT calculations.

A porous thin film obtained by adsorbing 1,3,5-tris(pyridyl)benzene (TPyB) molecules on Cu(111) is used as a host film. This film is formed when a Cu atom supplied from the substrate connect to two TPyB molecules, and hexagonal pores are periodically arranged. Formic acid is used as guest molecules.

Fig. 1 (a) shows an STM image of formic acid in the pores. A bright protrusion appears next to the two-coordinated Cu atom, and a zigzag chain is observed from the protrusion. Although the zigzag chain is observed in the adsorption structure of formic acid on Cu(111), the bright protrusion adjacent to the two-coordinated Cu originate from the unique adsorption structure in the pore.

Fig. 1(b) shows adsorption structures of an HCOOH molecule that is adjacent to two-coordinated Cu and the flat Cu(111) surface obtained by DFT calculation. The adsorption energy is larger for HCOOH adjacent to the two-coordinated Cu (-0.60 eV) compared to HCOOH on Cu(111) (-0.51 eV). For charge transfer between the substrate+film and the HCOOH molecule, charge transfer with the substrate decreases and that with the two-coordinated Cu increases when the HCOOH molecule is adjacent to the two-coordinated Cu. Therefore, the two-coordinated Cu provides new stable adsorption sites for HCOOH molecules.

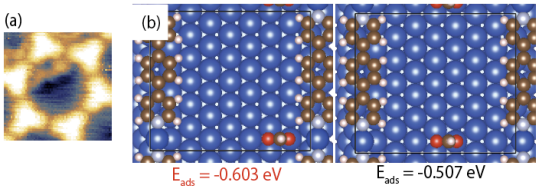

Fig. 1 (a) An STM image of HCOOH molecules in a pore of the metal-organic film on Cu(111). (b) Schematic drawings of a HCOOH molecule with two-coordinated Cu on Cu(111).

First-principles calculations of optical response to double-pulse lasers

Mizuho ONO[1], Hiroki GONOME[2]

[1]*Graduate School of Engineering,*

Tohoku University, Aoba-ku, Sendai, Miyagi 980-0845

[2]*Graduate School of Science and Engineering,*

Yamagata University, Jonan, Yonezawa, Yamagata 992-8510

Femtosecond laser pulses have very high peak intensities and can be used for nonlinear processing in wide-gap semiconductors and other applications. In recent years, material modification by multiple laser pulses has been proposed to avoid damage to optical elements [1]. Although a certain amount of energy must be applied for such material modification, it is generally difficult to predict the nonlinearity of the material. Therefore, in this study, the optical response of materials under double-pulse irradiation was verified using real-time time-dependent density functional theory. For silicon carbide, a typical wide-gap semiconductor, we examined the response to the second pulse for two systems: one in which the electrons remain in a non-equilibrium state after the first pulse and the other in which they form a thermal equilibrium state, i.e., a Fermi-Dirac distribution. Figure 1 shows the results of the induced current calculations. In the equilibrium system, a current with a threefold component was observed in addition to the laser's center frequency of 3.10 eV. In the non-equilibrium system, in addition to the 3.10 eV frequency, a current with a split threefold component was observed. Figure 2 shows the time evolution of the energy. The currents in the basic and threefold frequency components were higher in the equilibrium state, while the absorbed energy was higher in the nonequilibrium state.

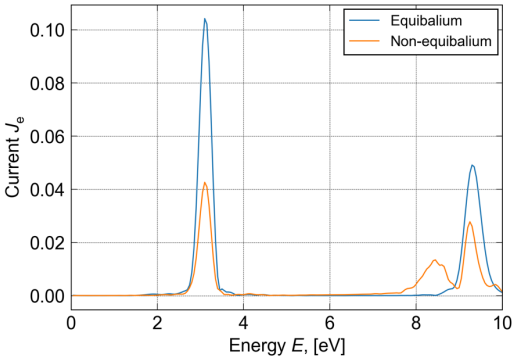

Figure 1 : Fourier components of electric current.

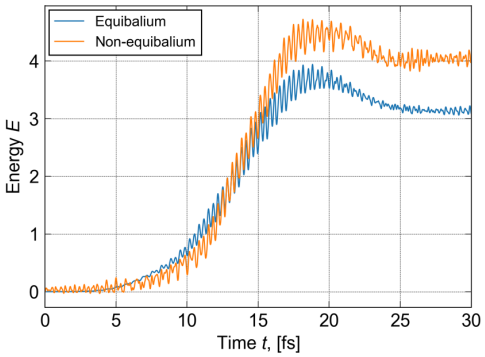

Figure 2 : Time series of internal energy.

References

[1] T. Otobe, T. Hayashi and M. Nishikino, Appl. Phys. Lett. **111**, 171107 (2017).

Structure-Performance Relationship Analysis for Catalysts

Hao LI

Advanced Institute for Materials Research (WPI-AIMR),

Tohoku University, Sendai 980-8577, Japan

The Hao Li Lab at WPI-AIMR aims to streamline catalyst search by focusing on developing precise catalysis theory for designing and understanding promising catalysts, thus bypassing the experimental trial-and-error process. In this ISSP project, we utilize *ab initio* calculations (e.g., density functional theory, DFT), multi-scale modeling, data science, and machine learning to facilitate catalyst design and comprehension. Numerous accomplishments from this project have been featured in top-tier journals like the Journal of the American Chemical Society, Nature Communications, and Angewandte Chemie International Edition.

An outstanding illustration from this project involves the investigation of pH-dependent oxygen reduction reaction (ORR) performance on single-atom catalysts (SACs) [1]. Initially, linear scaling relations were discerned among the binding energies of ORR adsorbates on different types of SACs (Fig. 1). Subsequently, we conducted pH-dependent microkinetic modeling and identified intriguing pH-dependent behaviors on SACs (Fig. 2), which align excellently with our subsequent experimental validations (Fig. 3).

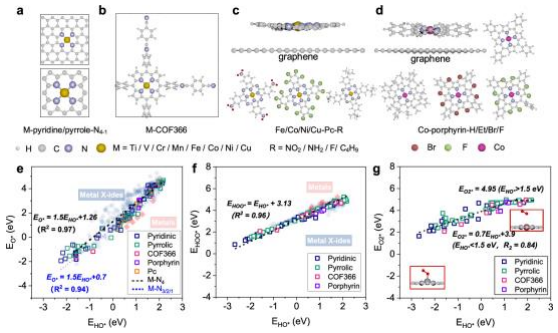

Fig. 1: Figure 1. Linear scaling relations are found in M–N–C catalysts with different atomistic environments.

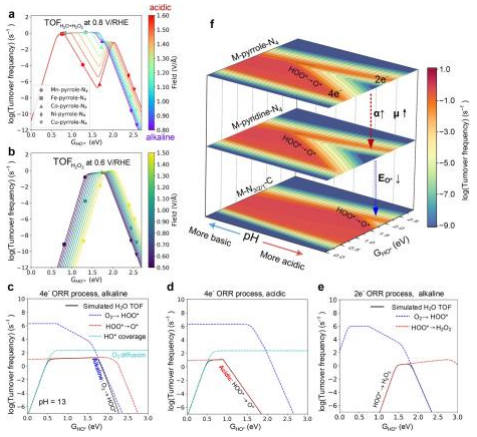

Fig. 2: Microkinetic ORR volcano models of M–N–C SACs and rate-determining analyses.

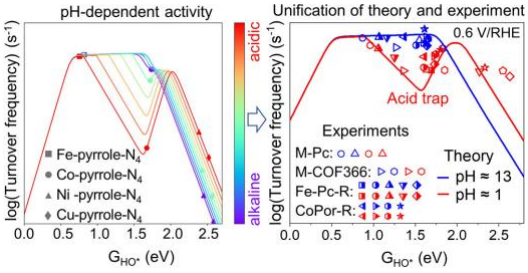

Fig. 3: Experimental validation on the derived pH-dependent volcano model for SAC ORR.

Another notable achievement is the development of an active machine-learning model for dynamic simulation and growth mechanisms of carbon on metal surfaces [2]. We designed an active learning framework to accurately fit a machine learning force field, replacing expensive DFT calculations (Fig. 4). This framework involves sampling data from various structures and utilizes on-the-fly validation and data acquisition to iteratively enhance the accuracy of the machine learning force field. The modeling results were compared with actual DFT results for validation.

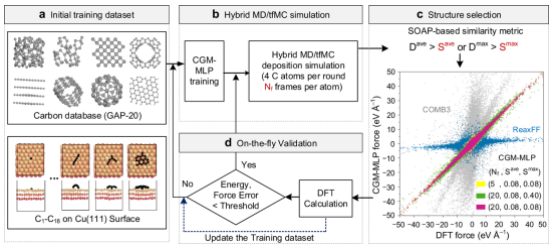

Fig. 4: The workflow of the development of on-the-fly fitting employed for this project.

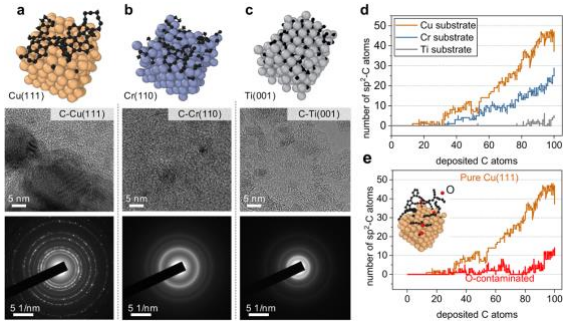

Fig. 5: Comparison between theory and experiments regarding the carbon forms on Cu, Cr, and Ti surfaces.

Utilizing the machine learning force field developed previously, we conducted extensive simulations on Cu(111), Cr(110), and Ti(001) surfaces, revealing distinct carbon behaviors on each surface. These findings demonstrate excellent agreement with subsequent experimental observations (Fig. 5). Another significant research outcome involves unraveling the structure-activity relationship for CO_2 electroreduction over SnO_2 using a standardized research paradigm [3]. We devised a workflow that integrates surface state analysis, surface reconstruction analysis, microkinetic modeling, and experimental validation (Fig. 6).

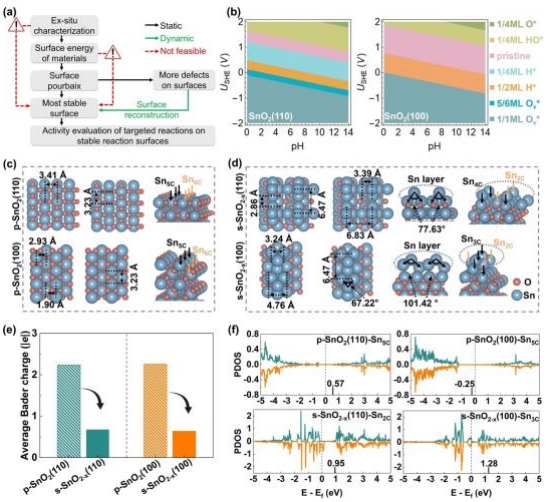

Fig. 6: Developed workflow for surface state analysis and structural dynamic evolution for CO_2 electroreduction using SnO_2.

In summary, we have successfully achieved the proposed objectives of this project, including the analysis of key reactions such as ORR and carbon behavior on catalysts. Moving forward, our future studies will focus on further developing this framework to enable more precise catalysis design, building upon our foundation in precise catalysis theory development.

❖ Besides, based on the generous

support of this ISSP project, we also have published other papers in 2023-2024, which are shown in Refs. [4-30].

References

1) D. Zhang, Z. Wang, F. Liu, P. Yi, L. Peng, Y. Chen, L. Wei*, and **H. Li***, J. Am. Chem. Soc., **2024**, 146, 3210–3219 (Cover Article).

2) D. Zhang*, P. Yi, X. Lai, L. Peng*, and **H. Li***, . Nat. Commun., **2024**, 15, 334.

3) Z. Guo, Y. Yu, C. Li, E. C. D. Santos, T. Wang, H. Li, J. Xu*, C. Liu*, and **H. Li***, Angew. Chem. Int. Ed., **2024**, 136, e202319913 .

4) D. Zhang, Y. Hirai, K. Nakamura, K. Ito, Y. Matsuo, K. Ishibashi1, Y. Hashimoto, H. Yabu*, and **H. Li***, Chem. Sci., **2024**, 15, 5123-5132 (Front Cover Article).

5) H. Liu, D. Zhang, Y. Wang, and **H. Li***, Langmuir, **2024**, 40, 7632–7638.

6) Y. Zhang, T. Wang, L. Mei, R. Yang, W. Guo, **H. Li***, and Z. Zeng*, Nanomicro Lett, **2024**, In Press (Invited Paper).

7) T. Wang, Z. Guo, H. Oka, A. Kumatani*, C. Liu*, and **H. Li***, J. Mater. Chem. A, **2024**, 12, 8438-8446.

8) F. Nekouei*, T. Wang*, F. Keshtpour, Y. Liu, **H. Li**, and S. Nekouei, Appl. Catal. B., **2024**, 351, 123974.

9) D. Zhu, J. Li, Z. Zheng, S. Ye, Y. Pan, J. Wu, F. She, L. Lai, Z. Zhou, J. Chen, **H. Li**, L. Wei*, and Y. Chen*, ACS Appl. Mater. Interfaces, **2024**, 16, 16175–16185.

10) C. Li, H. Liu, T. Zhang, Z. Liu, H. Shi, J. Cui, **H. Li***, H. Li*, and C. Li*, Adv. Mater., **2024**, 2312204.

11) X. Jiang, B. Zhou, W. Yang, J. Chen, C. Miao, **H. Li**, Y. Hou, X. Xu, L. Zhu D. Lin, and J. Xu*, Proc. Natl. Acad. Sci. U.S.A, **2024**, 121, e2309102121.

12) X. Jia, Z. Yu, F. Liu, H. Liu, D. Zhang., E. C. D. Santos, H. Zheng, Y. Hashimoto, Y. Chen, L. Wei*, and **H. Li***, Adv. Sci., **2024**, 11, 2305630.

13) Q. Li, D. Zhang, J. Wu*, Y. Luo, H. Liu, M. Lu, R. Cui, W. Liang, D. Wang, P. Xi*, M. Liu, **H. Li***, and L. Huang*, Adv. Mater., **2024**, 36, 2309266.

14) W. Yan, X. Wang, M. Liu, K. Ma, L. Wang, Q. Liu, C. Wang, X. Jiang, **H. Li**, Y. Tang*, G. Fu*, Adv. Funct. Mater., **2024**, 37, 2310487.

15) H. Liu, Y. Wang, P. Tan, E. C. D. Santos, S. M. Holmes, **H. Li***, J. Pan*, C. D'Agostino*, Small, **2023**, 2308948.

16) P. Wang, K. Zhang, **H. Li***, J. Hu*, and M. Zheng*, Small, **2023**, 2308791.

17) S. Ning, M. Li, X. Wang, D. Zhang, B. Zhang, C. Wang, D. Sun, Y. Tang, **H. Li**, K. Sun,* and G. Fu*, Angew. Chem. Int. Ed., **2023**, 62, e202314565.

18) Y. Zhang, T. Wang, F. Wang, H. Zheng, Z. Zeng*, and **H. Li***, J. Mater. Chem. A, **2023**, 11, 20528-20538.

19) J. Jing*, Z. Guo, Z. Li, Y. Chen, **H. Li***, and W-Y. Li*, Chem. Eng. Sci., **2023**, 282, 119251.

20) H. Liu, D. Zhang, S. M. Holmes, C.

D'Agostino*, and **H. Li***, Chem. Sci., **2023**, 14, 9000-9009 (Front Cover Article).

21) E. C. D. Santos, R. Sato, K. Kisu, K. Sau, X. Jia, F. Yang, S. Orimo*, and **H. Li***, Chem. Mater., **2023**, 35, 5996-6004.

22) W. Yang, Z. Jia, B. Zhou, L. Chen, X. Ding, L. Jiao, H. Zheng, Z. Gao*, Q. Wang*, and **H. Li***, ACS Catal., **2023**, 13, 9695-9705.

23) W. Yang*, Z. Jia, L. Chen, B. Zhou, D. Zhang, Y. Han, Z. Gao, and **H. Li***, Chem. Commun., **2023**, 59, 10761-10764 (Invited Paper).

24) C. Li, Z. Guo, Z. Liu, T. Zhang, H. Shi, J. Cui, M. Zhu, **H. Li***, H. Li*, and C. Li*, ACS Catal., **2023**, 13, 16114-16125 (Front Cover Article).

25) J. Li, Z. Guo, J. Wu, Z. Zheng, Z. Yu, F. She, L. Lai, **H. Li***, Y. Chen*, and L. Wei*, Adv. Energy Mater., **2023**, 13, 2301743.

26) Y. Hao*, Z. Guo, H. Cheng, C. Yao, S. Cheng, L. Yi, and **H. Li***, J. Colloid Interface Sci. **2023**, 650, 1949-1957.

27) M. Li, X. Wang, K. Liu, H. Guo, M. Li, D. Sun, **H. Li**, K. Huang*, Y. Tang*, and G. Fu*, Adv. Energy Mater., **2023**, 13, 2301162.

28) Z. Guo, C. Liu, C. Sun, J. Xu*, **H. Li***, and T. Wang*, ChemCatChem, **2023**, 15, e202300669.

29) W. Yang*, L. Chen, B. Zhou, Z. Jia, Y. Liu, **H. Li***, and Z. Gao*, J. Phys. Chem. C, **2023**, 127, 13011-13020.

30) M. Li, X, Wang, K. Liu, H. Sun, K. Huang, D. Sun, Y. Tang, W. Xing, **H. Li***, and G. Fu*, Adv. Mater., **2023**, 35, 2302462 (ESI Hot & Highly Cited Paper).